Image Analysis of Micrograph and Fractograph for Material Characterization

Thesis submitted by

Siddhartha Banerjee

Doctor of Philosophy (Engineering)

Department of Computer Science and Engineering
Faculty Council of Engineering & Technology
Jadavpur University
Kolkata, India

2019

JADAVPUR UNIVERSITY

KOLKATA – 700032, INDIA

INDEX NO. **40/12/E**

1. Title of the thesis : **Image Analysis of Micrograph and Fractograph for Material Characterization.**
2. Name, Designation & Institution of the Supervisors :
   (a) **Prof. Sanjoy Kumar Saha, Professor, Department of Computer Science and Engineering, Jadavpur University.**
   (b) **Prof. Pravash Chandra Chakraborti, Professor, Department of Metallurgical and Material Engineering, Jadavpur University.**
3. List of Publication :
   (a) Siddhartha Banerjee, Pravash Chandra Chakraborti and Sanjoy Kumar Saha. *An automated methodology for grain segmentation and grain size measurement from optical micrographs.* Measurement, volume 140, pages 142–150, 2019.
   (b) Siddhartha Banerjee, Subhas Bhunia, Pravash Chandra Chakraborti and Sanjoy Kumar Saha. *An Automated Approach for Volume Fraction Measurement of Titanium Alloy using Digital Image Processing.* Proceedings of the 7-th International Conference on Computer and Communication Technology, Pages 95-99, November 24 - 26, 2017.
   (c) Siddhartha Banerjee, Tanuka Dasgupta, Subhajit Mukherjee, Mahadev Shome, Pravash Candra Chakraborti and Sanjoy Kumar Saha. *Digital image correlation for grain scale strain measurement in interstitial free high strength steel.* Materials Science and Technology, volume 32(4), pages 328-337, 2016.
   (d) Siddhartha Banerjee, Swarup Kumar Ghosh, Subhabrata Dutta and Sanjoy Kumar Saha. *Segmentation of dual phase steel micrograph: An automated Approach.* Measurement, volume 46, pages 2435–2440, 2013.
   (e) Siddhartha Banerjee, Koustav Basu, Pravash Chandra Chakraborti and Sanjoy Kumar Saha. *Segmentation of SEM Fractograph into Void and Surface Region.* In Proceedings of the International Conference on Advances in Materials and Materials Processing (ICAMMP), 2011.

   (f) Siddhartha Banerjee, Koustav Basu, Pravash Chandra Chakraborti and Sanjoy Kumar Saha. *Extraction of Region Contour in SEM Fractographs.* In Proceedings of the Second International Conference on Emerging Applications of Information Technology (EAIT), pages 98-101, 2011.

4. List of Patents : None.

5. List of Presentations in National/International/Conferences/Workshops :

   (a) Siddhartha Banerjee, Subhas Bhunia, Pravash Chandra Chakraborti and Sanjoy Kumar Saha. *An Automated Approach for Volume Fraction Measurement of Titanium Alloy using Digital Image Processing.* Proceedings of the 7-th International Conference on Computer and Communication Technology, Pages 95-99, November 24 - 26, 2017.

   (b) Siddhartha Banerjee, Koustav Basu, Pravash Chandra Chakraborti and Sanjoy Kumar Saha. *Extraction of Region Contour in SEM Fractographs.* In Proceedings of the Second International Conference on Emerging Applications of Information Technology (EAIT), pages 98-101, 2011.

CERTIFICATE FROM THE SUPERVISORS

This is to certify that the thesis entitled **"Image Analysis of Micrograph and Fractograph for Material Characterization"** submitted by Shri **Siddhartha Banerjee** who got his name registered on **13/08/2012** for the award of Ph.D. (Engg.) degree of Jadavpur University is absolutely based upon his own work under the supervision of **Prof. Sanjoy Kumar Saha** and **Prof. Pravash Chandra Chakraborti** and that neither his thesis nor any part of the thesis has been submitted for any degree/diploma or any other academic award anywhere before.

1. ————————————

Signature of the Supervisor
and date with Office Seal

2. ————————————

Signature of the Supervisor
and date with Office Seal

Acknowledgements

At the outset I would acknowledge the patient efforts of my supervisors **Prof. Sanjoy Kumar Saha** and **Prof. Pravash Chandra Chakraborti** in deciding upon the problem which finally has led to this thesis. Without their iterative feedback and suggestions it would not have been possible to come up with this direction of research. I am grateful to them for their painstaking review of my work and meaningful suggestions which ultimately has given shape to this thesis.

Signature

Abstract

Metals and alloys are extensively used for engineering applications. Strength, ductility, toughness, creep, wear or abrasion, fatigue etc. are generally considered to be some very important mechanical properties of materials in different applications. Properties of metals and alloys are governed by their micro-structures which are evolved through different thermal and mechanical processing. Hence, the study of micro-structure of metals and alloys is very important. The objective of present work is to develop image processing based automated methodologies for analysing the micro-structures of material and fracture surface. In this respect four tasks, namely (i) studying grain size distribution in the micro-structure of single phase material, (ii) measuring the volume fraction of different phases present in a material, (iii) studying micro level deformation in a single phase material and finally, (iv) studying distribution of void in a ductile fracture surface have been considered. To fulfil the objectives developing the segmentation methodologies to extract the regions of interest (grain, phase and void) is considered as the most significant task.

Properties like yield strength, tensile strength, toughness, ductility, fatigue strength, creep strength and susceptibility to brittle fracture are governed by grain size. Knowledge of grain size is, therefore, very important. Commercially available software are intensity based threshold oriented and suffers if the grain boundaries are not well demarcated. Proposed edge oriented methodology can detect the closed contour of the grains despite of intensity variation within the grain and similarity between the intensities of grain boundary and grain interior. Experiment shows that the computed grain size is found to be very close to ASTM reference value.

In case of materials with micro-structures consisting of multiple phases, relative volume fraction of phases concerned, governs the average properties of the material. For such analysis identification and extraction of the phases present is important task. We have worked with two different material namely dual phase steel and titanium alloy. Normally different phases correspond to different intensity level. But simple intensity based thresholding as adopted by commercial software cannot work well due to non uniform intensity values within a phase and also due to overlap in intensity between one of the phases and phase boundary. More so in case of titanium alloy as primary α and transformed $\beta(\alpha)$ phases are of similar intensity. Methodologies for both the materials consider post processing

that follows thresholding to overcome the specific challenges. For dual phase steel removal of grain boundary, linking and refining of phases constitute post processing. In case of titanium alloy, geometric property is considered to distinguish two types of α.

Grain size and phase volume fraction help in correlating the average or macro level strength property of the material. It is known that deformation response of all the grains under the influence of external load cannot remain same and depends upon the crystallographic orientation of the grains with respect to the loading axis and also on the orientation of the surrounding grains. As a result, investigation towards understanding the nature of micro-level deformation is essential. The simplest case is to study the grain level behaviour for a single phase material. In this work we have investigated the tensile deformation of IFHS steel. The specimen is put under varying load and a sequence of micrographs at different loads are studied. Proposed methodology extracts the grains and tracks them over the sequence of micrographs. It uses artificial grids over the images and does not require any other sophisticated experimental technique to lay the grids on the specimen surface itself. Finally, grain level strain is measured. It has been observed that deformation is heterogeneous.

As micro-structure controls the deformation behaviour of any material, it is also connected with the fracture or failure of a component during service. It becomes necessary to understand the role of micro-structure on the fracture processes. Ductile fracture involving different stages, *e.g.* void nucleation, void growth and void coalescence, forming micro-crack results into dimple fracture surface. Void size and their distribution are well connected to the deformation process leading to failures. An automated methodology has been proposed to extract the voids and to find their size and distribution. The study reveals that void features, like void size and void density at different strain rates bear good correlations with tensile properties of ductile materials.

The salient feature of the proposed image processing based methodologies is that, unlike commercial software no intervention from the end user is required. Moreover, the usage and outcome are not prejudiced by the prior acquaintance of image processing operations.

Table of contents

List of figures

List of tables

Chapter 1

Introduction

1.1 Background

Metals and alloys find extensive uses for engineering applications despite the current trend towards developing newer materials with fascinating properties to meet specific requirements. Among various property requirements depending upon the application areas, mechanical properties of any metallic system are of great importance. Strength, ductility, toughness, creep, wear or abrasion, fatigue etc. are generally considered to be some very important mechanical properties in different applications.

Properties of metals and alloys are governed by their chemistry and micro-structures which are evolved through different thermal and mechanical processing. For fixed chemistry, modulation of micro-structure through changes in processing schedule (thermal, mechanical or both) leads to different combinations of mechanical properties. Hence, the study of micro-structure of any metal or alloy which is the assemblage of different phases is extremely important. The complete study of any micro-structure requires observation of metallographically polished and etched surface of small specimen in a microscope, capturing the images of micro-structure and finally performing quantitative analysis. In strict sense, stereological analysis of the micro-structural features is most important. It goes without saying that the importance of quantitative analysis of micro-structural parameters, like, size, shape, distribution and the overall morphology of different phase constituents including the grains, control the mechanical properties of metals and alloys.

Metallic elements found in Mendeleev's Periodic Table are completely in pure form and so are single phase systems. Single phase alloy systems are not pure system, *i.e.*, not a single component system, and these are called solid solution. Micro-structure of polycrystalline single phase systems are primarily composed of grains only. In such cases, micro-structure is characterized by grain size, grain shape and their distribution. In reality, grains do not always have same size and their two-dimensional shapes can also vary in a field of view. The size, shape and distribution of the grains depend upon the processing route of the materials. Generally, though in case of single phase systems the mechanical properties are correlated with an average grain size, their shape and distribution also have significant influence on mechanical properties [1–3].

The properties which are largely governed by grain size are: yield strength, tensile strength, toughness, ductility, fatigue strength, creep strength and susceptibility to brittle fracture. Knowledge of grain size is, therefore, very important in understanding the above properties and correlating the material's chemistry and processing route with the final grain structure. Grain size determination is thus a very important aspect in microstructure-property relationship of a material. It is generally done on images obtained by optical microscopy which requires polishing and etching of specimens. The major issue is perfect polishing and etching of the specimen to reveal grain boundaries. These steps are largely manual in nature and require individual skill. Grain size determination using optical microscopy is commonly done with the help of commercially available image analysis package. It may be noted that using these software packages may lead to misleading results in cases when all the grain boundaries are not properly etched and broken boundaries are present. Therefore, the major challenge remains how to measure the grain size when the optical microscopic images do not reveal the grain boundaries to a very good extent.

While grain size of single phase materials control the strength and toughness of a material in such a manner that with lowering of grain size both strength and toughness are increased, there are limitations of increasing the strength just by lowering the grain size only [4, 5]. As a result, materials with micro-structure consisting of multiple phases are considered for optimum combination of different mechanical properties. In such cases, the average properties of the material are influenced by the phases present. Generally, the Law of Mechanical Mixture is used to predict the strength of materials consisting of multiple phases. To apply this law it is required to know the relative volume fraction of the phases concerned. The commercially available image analysis packages which are used for estimating the phase volume fractions, identifies the phases based on gray level intensity of different phases. But, many a time it becomes difficult to have micro-structures of high and uniform contrast all through the field of view. Small variation in gray level in region to region poses trouble for accurate estimation of different phases.

It appears from above that proper determination of micro-structural parameters, be it grain size or relative amounts of different phases, would help in correlating and predicting strength of a material with high accuracy. It is worthwhile to mention here that the strength property that is correlated with micro-structural parameters is the average property or macro property. At this point it is very much intriguing whether the macroscopic property is really representative when the scale of measurement is reduced down to grain level. To have a knowledge of micro-level or grain level deformation behaviour it is simpler if a single phase material consisting only of grains (grain body and grain boundary) is considered. The choice of considering single phase materials is to avoid the interaction effect between different phase present in the micro-structure. However, though by considering a single-phase material such interaction effect between the phases can be avoided, it is also interesting to know whether all the grains in single phase materials do behave similarly under the influence of external load. A survey of literature shows that deformation response of all the grains under the influence of external load cannot remain same and depend upon the crystallographic orientation of the grains with respect to the loading axis [6–8]. In reality, the grains in a single phase materials are randomly oriented with respect to the loading axis. The grains which are favorably oriented with respect to the loading axis are highly responsive towards deformation; and unfavorably oriented grains deform at higher load.

Nowadays, electron back scatter diffraction (EBSD) technique in conjunction with scanning electron microscope is used to understand the deformation heterogeneity in polycrystalline materials. Deformation experiments directly within scanning electron microscope also provide scope for studying the deformation response of individual grain under load. In this technique the grain structure and other constituting phases of the material are directly observed during deformation. It is known that the deformation characteristic of individual grain depends on its crystallographic orientation and also on the orientation of the surrounding grains with respect to loading axis. Collectively, the deformation of individual grain controls the average deformation behaviour of a material. As a result, investigation towards understanding the nature of micro-level deformation has gained impetus over the last decade [9–15]. It is worth mentioning that strain measurement at any point in an area of interest, is required for better understanding of the deformation behaviour of materials. Use of digital image processing and correlation techniques has enabled such measurements. In this direction, deformation of grid pattern introduced on the specimen surface by lithography [16–19], and from correlating the speckle pattern placed on specimen surface is commonly used taking help of digital image correlating software [20, 21]. These techniques require additional steps in preparing the specimens, and also depends on the adhesiveness of the speckles with the specimen surface as deformation is progressed.

The ultimate goal to develop materials is to sustain a component under service conditions. Load bearing components may undergo complete failure following deformation. While micro-structure controls the deformation behavior of any material, it is also connected with the fracture or failure of a component during service. As such it is always desired to use materials with high fracture resistance behavior. Fracture is broadly classified as brittle or ductile. It becomes necessary to understand the role of micro-structure on the fracture processes. In this regard, post-mortem analysis of fracture surfaces which carry the signatures for the type of failure is done, in order to find a link with the material's micro-structure and the loading conditions including the environment.

Ductile fracture occurs through the stages, like void nucleation, void growth and void coalescence leading to the formation of micro-cracks, which by spreading under load, leads to final fracture. In general, fracture occurring following these steps results in dimple fracture surfaces. Careful examination of such dimple fracture surfaces in scanning electron microscope and subsequent analysis provides information about void size and their distribution. It has been reported in literature that the void size and distribution are well connected with the deformation process culminating to fracture [22–24]. However, determination of the size of very large number of voids requires painstaking manual/semi-manual processes on the images of fracture surfaces. Therefore, developing an automated procedure which would be robust on one side and user friendly on the other side would be very much beneficial to analyse the ductile fracture surfaces of any material. The scope of the present work is limited to ductile fracture.

1.2 Past Work

In the context of developing materials, characterization of micro-structure through determination of grain size distribution and volume fraction of constituting phases, looking into the homogeneity/heterogeneity of deformation under load and finally the analysis of fracture surfaces play important role. In this regard, use of digital image processing (DIP) techniques have been popular with the advent of image acquisition technology and instruments. In all such analyses, extracting the regions of interest is an important issue. In case of volume fraction measurement the region of interest is different phases present in the micrograph where as in grain size distribution detection of grains is important. Establishment of correlation between the region of interest in same fields of fractograph of varying load played central role. Researchers use both non DIP and DIP methods for such measurement. An outline of these past work are described in the following sections.

1.2.1 Identification of Grain and Grain Size Analysis

Common measurement procedures, like linear intercept method [25] or Planimetric method [26] is used to determine the average grain size. As a routine purpose these images are analyzed using commercially available image analysis software. In an image processing based system, it is important to extract the grains. As the grains are normally separated by boundary, detection of boundaries can also help in extraction.

Watershed-based scheme [27–29] can be used for segmentation and it provides closed contour of the extracted regions. As there is intensity variation within the grains, it is likely that the grains will be over-segmented and this will affect the size measurement significantly. Various segmentation methods are commonly used in the field of geology [30–32]. But these methods are not applicable in the current context as the micrographs under consideration are of different characteristics.

Gauthier et al. [33] has presented an automated scheme for segmenting WC (Tungsten Carbide) grains in the Cobalt matrix. The segmentation was done from two types of image namely the back scattered electron composition (BSEC) and back scattered electron topography (BSET) images. They have adopted a two stage algorithm for segmentation of grain. Heilbronner [34] developed a methodology that considers a number of images of a particular field of view. Significant boundaries are detected from each image using gradient filter. All such boundaries are finally combined to obtain a single grain boundary map. Dengiz et al. [35] presented a Fuzzy logic based algorithm and a Artificial Neural Network (ANN) based algorithm to detect the grain boundary in the images of alloy steel. Both the methods provide better performance in comparison to commonly used image processing tools. However, sufficient data is required for training the neural network. Zhuravel et al. [36] proposed a method based on fractal dimension. An automated system is presented by Barreto et al. [37], that works depending on thresholding. An image is pre-processed to merge the neighboring pixels with intensity values within a tolerance range. Depending on the tolerance range, the method may give rise to over or under segmentation. ImageJ is a software tool that offers collection of basic image processing functionality and also used for measuring grain size [38, 39].

1.2.2 Phase Identification and Phase Volume Fraction Measurement

It is quite common to study the volume fraction of different phases present in the microstructure. In the image processing based approach it is essential to differentiate the phases based on certain features. Intensity is quite commonly used feature. Komenda [40] proposed a scheme where an image classifier has been integrated with *context vision* [41]. It facilitates contextual analysis (i.e. spatial dependencies among the regions) for extracting the areas of interest. But, such analysis incurs computational cost. Moreover, the classification accuracy heavily depends on proper training. Neural network also have been tried to classify the phases of an alloy [42]. Accuracy depends on training and that requires sufficient data. Chatterjee et al. [43] presented an image processing based automated system that considered intensity based thresholding to differentiate the phases present in High Strength Low Alloy (HSLA) steel. To refine the measurement, phase boundaries which might have intensity values similar to one of the phases present were identified as thin region and ignored in measurement. Gruttadauria et al. [44] utilized Image Pro Plus software to identify the phases based on intensity variation.

1.2.3 Local Strain Analysis

Strain analysis is done to examine the deformation that a specimen undergoes on being subjected to incremental load. By studying the images at different loads analysis is done.

An algorithm is presented by Ulstad [45] to generate an estimation of the difference of two distorted digital image. In the first step nonlinear transformation is carried out to obtain spatial registration of the two images under comparison. Local area intensity statistics are compared in order to find the difference of the two images to estimate small scale differences between the two images. An improved algorithm using Electronic speckle photography is presented and analyzed by Sjodahl [46]. It offers a simple and fast technique for measuring in-plane displacement in solid and fluid mechanics. The algorithm is analyzed using both computer-simulated speckle patterns and real experiments. The digital image correlation technique is used by Cintron et al. [47] to present an innovative system Vic-2D for strain measurements in a two-dimensional contour map for planar surface. A commercially available optical strain measurement system (ARAMIS) that utilizes the Digital Image Correlation (DIC) methodology is used by Kang [20] for microscopic strain mapping. The paper shows that the accuracy of the strain mapping depends on the preparation of the samples for SEM observation. Cao et al. [48] developed a simple and efficient non-contact method to measure the Poisson's ratio using DIC method. A comparative study has been carried out by Ghadbeigi et al. [49] to assess the accuracy of DIC technique in measurement of large strains of an Interstitial Free (IF) steel. A micro-grid technique has been used to compare the strain measured by DIC. It is also reported that the DIC technique can also be used to determine the heterogeneity and severity of deformation in polycrystals [50]. Besides, in situations where it is difficult to measure the strain directly, this technique finds application in knowing macroscopic strain as in case of creep deformation [51].

1.2.4 Fracture Surface Analysis

Investigating a fracture surface is associated with failure analysis. It is well known that ductile fracture occurs due to the formation of voids, their growth and coalescence forming a micro-crack. Quantitative estimation like average circular diameter of voids, void density on the fracture surface etc. are very significant in understanding the mechanical properties of materials undergoing ductile fracture. For such quantitative analysis, detection of void regions is the most important task.

Bandstra et al. [52] employed micro-mechanical modelling with finite element analysis to examine local deformation behaviour within void arrays of HY-100 steel. In this work different factors, like size, spacing, clustering of the void have been studied using image based multi-hole model. Chae et al. [53] have studied density and volume fraction of strain-induced voids for HSLA-

100 steel. The objective was to determine the damage accumulation pattern for tensile failure over a range of stress-states. The study was done using Image Pro Plus, an image processing software. Ductile fracture behaviour of 304LN stainless steel at various strain rates has been studied by Das et al. [22]. The fracture behavior is characterized using void morphology *i.e.* void size, void density and void size distribution on the tensile fracture surface. The deformation behavior of copper-strengthened high-strength low-alloy steel also has been investigated by Das at al. [54]. In both the cases, they have also relied on image processing tool and manually applied different options from the tool for the purpose. Taslicukur et al. [55] examined the microstructural characterization and the fracture behavior of GG20 and GG25 gray cast iron materials. In this work Leica QWin software was used for image analysis. Cu-strengthened high strength low alloy (HSLA) steel has been analyzed by Dutta et al. [56] to automatically characterize micrographs and fractographs. They introduce texture analysis method for this purpose. The texture analysis method consists of several steps like fractal analysis using box-counting, grey level co-occurrence matrix (GLCM) technique and run length statistical (RLS) analysis technique.

1.3 Present Work

Objective:

- Objective of the present work is to develop image processing based automated methodologies for analysing the micro-structures of material and fracture surface. As a result, prior understanding of image processing will not be a prerequisite for the user. The analysis includes the following
  - Studying grain size distribution in the micro-structure of single phase material.
  - Measuring the volume fraction of different phases present in a material.
  - Studying micro level deformation in a single phase material.
  - Studying distribution of void in a fracture surface.
- To enable the analysis, developing segmentation methodologies to extract the regions of interest (grain, phase and void) becomes the significant task.
- To develop a non-invasive approach based on image processing for studying deformation.

1.3.1 Contribution of the Work

Major contribution of the present work are as follows:

- An automated system has been developed for studying grain size distribution from optical micrograph [57]. Proposed methodology extracts the grains following edge oriented approach and can cope up with grains of varying intensity. Subsequently grain size measurement is carried out.
- A novel scheme for automatic extraction of the phases present in the micro-structure of dual phase steel and subsequent measurement of volume fraction of the phases [58] has been proposed. Proposed methodology works well despite the variation of intensity present in a phase, overlap of intensity between a phase and grain boundary. It can also handle fragmented phase components.
- A methodology has been developed for measuring the volume fraction of phases present in Titanium alloy [59]. The methodology identifies primary α and transformed β (α) phase. Within the transformed phase α/β lamellar matrix are also identified.
- To study the deformation homogeneity/heterogeneity in single phase material, digital image correlation (DIC) based methodology has been developed [60]. It enables the study of deformation at micro level.
- An automated system has been developed to analyse the dimple fracture surface forming due to ductile fracture [61, 62]. It extracts the voids and studies their distribution.

1.3.2 Overview of the Dissertation

In this work image processing based automated methodologies have been developed for analysing the micro-structures of material and fracture surfaces. The major parts of the work is shown in Figure 1.1. Methodologies have been developed for grain size analysis, phase volume fraction measurement, local strain analysis and fracture surface analysis. The dissertation elaborates the details of the methodologies in subsequent chapters.

Grain size of a material and its distribution has tremendous impact on strength and toughness of a material. Commercially available image analysis software which works with gray level thresholding are routinely used for this purpose. The results obtained by using such software are dependent on how clearly the grain boundaries are revealed in the micro-structure. Difficulty in demarcating the

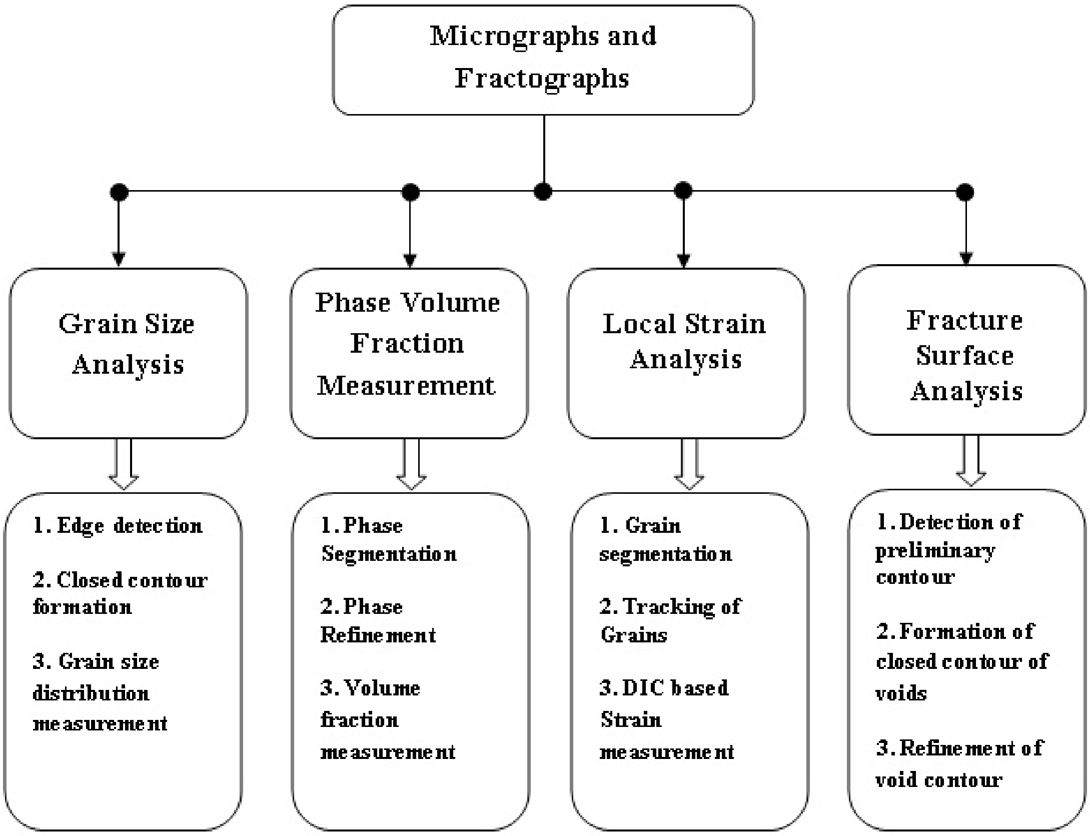

Fig. 1.1 Overall Organization of the Dissertation.

grain body and grain boundaries arises due to non uniform etching or over etching of the polished specimen surface. In such cases proper extraction of the grains is very crucial. A robust automated methodology has been proposed in Chapter 2 to extract the close contours of grains. It enables subsequent measurement of size and analysis.

In a material with micro-structure consisting of multiple phases, volume fraction of the phases present have bearing on the mechanical properties. Hence it is important to know the volume fraction of the phases present in the material. In the current scope of this work, we have worked with two different material namely dual phase steel and titanium alloy. In the dual phase steel two phases correspond to two different intensity levels. But non uniform intensity values in a phase and overlap between the phases pose the challenge. In titanium alloy there is primary α phase and transformed phase consisting of α/β lamellar matrix. The primary challenge is to extract two types of α and β. Chapter 3 details the automated methodologies to extract the phases and to measure their volume fraction for the two cases.

Grain size distribution or phase volume fraction can be correlated with average (macro level) deformation / strength of a material. However, the average response does not hold good at small length (grain) scale. Hence, it is important to study the local deformation pattern. As discussed earlier, the simplest case is to study the grain level behaviour of single phase material. In this effort miniature sized specimen is loaded in steps and a series of high resolution micrographs corresponding to different loads are examined. In Chapter 4, a digital image correlation based methodology has been presented for this purpose.

Deformation may lead to complete failure of a load bearing components. In fact micro-strcutures do really control the deformation and fracture behaviour of any material. Present scope of the work includes the characterization of ductile fracture surfaces which carries the signature of fracture processes or types. Ductile fracture occurring through stages, like void nucleation, void growth and void coalescence results into dimple fracture surface. Void size and their distribution are well connected to the deformation process leading to failures. An automated methodology has been proposed to extract the voids and to find their size and distribution. It has been described in Chapter 5.

Finally, the work is summarized and scope for further research is outlined in Chapter 6.

Chapter 2

Identification of Grain and Grain Size Analysis

2.1 Introduction

Mechanical behaviour of metals and alloys are structure sensitive properties. Modulation of micro-structure of a material without changing the chemistry gives rise to a wide range of property combinations. Thermal and mechanical processing of metals and alloys in a controlled manner modulates the overall micro-structure through characteristic changes of the phases, and by allowing new phases to form. It is not only the mere presence of the phases, but their volume fraction, size, shape and distribution – all together constitute the micro-structure of any material. Change of any of these measurable parameters results into a new material with new properties. Quantification of the characterizing parameters of the phases present in a material is essential in at least three ways: (1) to understand the response of a material against different types of mechanical and thermal loads, (2) for quantitative prediction of mechanical properties, and (3) for designing of alloy - its composition and processing schedule. The importance of quantitative analysis of micro-structure is thus well understood. In single phase materials the task of analyzing the micro-structure is apparently simple as in such cases micro-structure consists of only grains. The properties of such materials are governed by the grain size, grain shape and the distribution of grains. It is worth mentioning here that by reducing the grain size two very fundamental mechanical properties of any material, namely strength and toughness, are improved [4, 5]. Hence, it is worth to study the grain size and its distribution.

2.2 Past Work

Classical methods of studying micro-structure of metal involve microscopic observation of different phases on sectioned surface. The area of interest on the surface is mechanically polished (or finally electropolished) to make the surface completely scratch free and then the polished surface is properly etched with chemical reagents. Finally, the etched surface is viewed either in optical or in scanning electron microscope (SEM). To get an overall picture about the micro-structure it is required to observe a large number of fields and capture the images. These images are subsequently analyzed for characterizing the micro-structure of any material.

Common measurement procedures, like linear intercept method [25] or Planimetric method [26] is used to determine the average grain size. As a routine purpose these images are analyzed using commercially available image analysis software. In such procedures primarily grey level thresholding is done to identify the grain and grain boundaries. It should, however, be noted here that the etching process which is essential to reveal grain boundaries is a manual skill based process. Uniform etching all through the field of view is extremely difficult, if not impossible. Nonuniform etching and also overetching of grain boundaries poses problem in identifying the actual grain boundaries. To obviate this difficulty a robust automated methodology is presented in this work. In an automated grain measuring software the first and major step is to segment the individual grains present in the micrographs. The proposed work is primarily focused on this aspect. Thereafter grain size is measured. In this work major emphasis has been put to extract the closed boundary encompassing a grain to minimize the error in measurement.

Mostly used segmentation technique is based on intensity thresholding. Ideally, the interior of the grains and the boundary separating the grains are of different intensity value. Thus, intensity based thresholding may be thought of as a way to categorize the pixels as boundary or grain interior pixels. However, the intensity values of the grain interior pixels and boundary pixels may overlap. Moreover, within each category also intensity variation may exist. Thus, threshold selection is a challenge. Different methods for optimal threshold selection exist in literature [63–65]. But, the intensity variations of intra and inter grains affects the segmentation outcome.

Another common approach for segmentation is based on edge detection [66, 67]. Ideally, grain interiors are uniform in terms of intensity and there exists an intensity variation between the grain interiors and boundary regions. Thus, edge detection based techniques are expected to detect the boundary as the edge. It assumes that objects in an image have clear borders, where a significant difference of intensity is present. But intra grain variation gives rise to unwanted edge pixels. It may fail to detect weak boundary where the intensity variation is low. Thus, simple edge detection based approach cannot provide desired closed contour of the grains.

Watershed-based scheme [27–29] can also be used for segmentation and it provides closed contour of the extracted regions. As there is intensity variation within the grains, it is likely that the grains will be over-segmented and this will affect the size measurement significantly. Various segmentation methods are commonly used in the field of geology [30–32]. But these methods are not applicable in the current context as the micrographs under consideration are of different characteristics.

A neural network and fuzzy logic based algorithm was developed by Dengiz et al. [35] to detect the grain boundary of steel alloys. But the applicability of the method is constrained by the availability of sufficient data. Heilbronner [34] developed a methodology for automatic detection of grain boundary in reduced time. In this method a number of images of a particular field of view are captured and significant boundaries are detected from each using gradient filter. All such boundaries are finally combined. But, it may fail to provide closed contour. Another complexity of the method is related with registration of different images. In [37], a system is presented that works around thresholding. An image is pre-processed to merge the neighboring pixels with intensity values within a tolerance range. Depending on the tolerance range, the method may give rise to over (under) segmentation. ImageJ is a software tool that offers collection of basic image processing functionality and also used for measuring grain size using the software [38, 39]. Das et al. [68] analysed the grain size for Al-Si-Mg alloy using canny edge detection, fractal and run-length statistical parameters. Campbell et al. [69] deployed watershed algorithm for the purpose. To avoid over segmentation, they followed a merging technique.

The above brief discussion about different image processing methods for grain segmentation vis-à-vis grain size determination reveals that there does not exist any generic solution to extract regions of interest. Segmentation is, in general, an ill posed problem. Depending on the application methodology is devised to meet the specific requirements. In this work we propose a robust methodology which is edge oriented. It extracts close contours of the grains in a set of micrographs with the final objective to measure the grain size.

2.3 Proposed Methodology

The determination of grain size and its distribution require very good quality images captured using light microscopy. Generally, light microscopic images are used for this purpose. A large sheet of Interstitial-free steel has been used as the material. In the present work optical micrographs of the surface of the specimen has been used to develop a robust methodology. As shown in Figure 2.1, it is observed that the sample micro-structure consists of equiaxed grains [70] which are mostly separated by boundaries with intensity values considerably different from the neighbouring grain interiors.

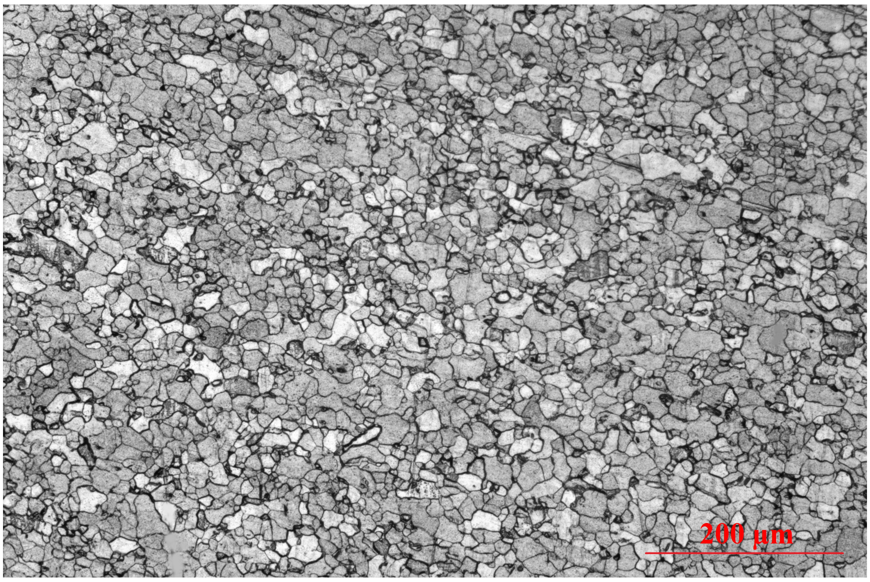

Fig. 2.1 A sample micrograph showing the grain structure of a metal surface.

Proposed methodology consists of two major steps, like extraction of closed contour of the grains and measurement of grain-size and these are elaborated in this section.

2.3.1 Extraction of Closed Contour of the Grains

In a micrograph, ideally a grain is a smooth region with distinct boundary separating it from the neighbouring grains. Careful observation of the micrographs (as in Figure 2.1) indicates that different grains may have different intensities. Although the intensity of the grain boundaries are of different from the neighbouring grains, globally it can have overlap with the intensity value of other grain interiors. As a result common approach of intensity based thresholding may fail to separate the grain interior and boundary. On the other hand, edge based approach seems promising as the boundaries are of intensity value that is locally different. But, non uniformity present in the grain interiors may give rise to additional and unwanted edges. In case, boundary is not dominant then it results into discontinuity in the grain contours. Moreover a thick boundary results into a pair of edges. Thus, edge detection alone also cannot serve the purpose. Edge detection acts as the foundation for the proposed methodology and subsequently a set of processing is performed to overcome the shortfalls. It ensures that closed contour of the grains are finally determined and the methodology works for a wide variety of micrographs. The major steps are as follows.

- Edge Detection.
- Closed Contour Formation.

Edge Detection

To extract the grain boundaries, the canny edge detection algorithm [71] is applied. The algorithm is quite robust and consists of number of steps runs as follows:

1. **Smoothing of the image**: Since the detection of edges are heavily affected by noise present in the image, it is essential to remove noise to prevent detection of false edges. The Gaussian filter is used to smooth the image to reduce the effect of noise on the edge detector.

   A Gaussian filter [66, 67] kernel of size 5 × 5 with σ = 1.4 given below is used in this algorithm.

$$\frac{1}{115}\begin{pmatrix} 2 & 4 & 5 & 4 & 2 \\ 4 & 9 & 12 & 9 & 4 \\ 5 & 12 & 15 & 12 & 5 \\ 4 & 9 & 12 & 9 & 4 \\ 2 & 4 & 5 & 4 & 2 \end{pmatrix}$$

2. **Finding gradients**: After smoothing the image, the edge strength is calculated by finding the gradient of the image. Sobel operator [66, 67] is used to measured the gradient of the image. The Sobel operator uses two 3 × 3 convolution mask given below to estimating gradient in horizontal direction (G_x) and in vertical direction (G_y) respectively for each pixel.

$$G_x = \begin{pmatrix} -1 & 0 & +1 \\ -2 & 0 & +2 \\ -1 & 0 & +1 \end{pmatrix} G_y = \begin{pmatrix} +1 & +2 & +1 \\ 0 & 0 & 0 \\ -1 & -2 & -1 \end{pmatrix}$$

   From these G_x and G_y edge gradient and edge direction are calculated using equations 2.1 and 2.2.

$$|G| = |G_x| + |G_y| \tag{2.1}$$

$$\theta = \arctan\frac{|G_y|}{|G_x|} \tag{2.2}$$

   After finding the edge direction, a relation is established for the edge direction with actual direction that can be traced in an image. With respect to the centre pixel **a** in the 5 × 5 matrix given below, there are four possible direction namely horizontal direction (0^o), vertical direction

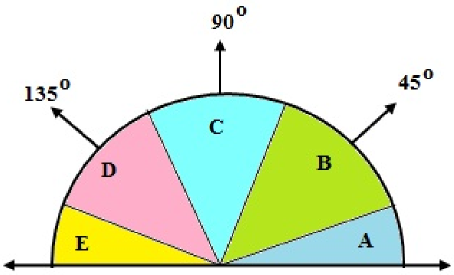

Fig. 2.2 Edge direction approximation.

(90^o), and two diagonals (45^o and 135^o).

$$\begin{pmatrix} \times & \times & \times & \times & \times \\ \times & \times & \times & \times & \times \\ \times & \times & \mathbf{a} & \times & \times \\ \times & \times & \times & \times & \times \\ \times & \times & \times & \times & \times \end{pmatrix}$$

Thus any edge direction calculated by equation 2.2 is approximate to the closest angle as shown in Figure 2.2.

Any edge falling within the region **A** and **E** (i.e. edge direction falling in the range 0^o to 22.5^o and 157.5^o to 180^o) is set to 0^o. Any edge direction falling in the region **B** (between 22.5^o and 67.5^o) is set to 45^o. Similarly, any edge direction falling in the region **C** and **D** is set to 90^o and 135^o respectively.

3. **Non-maximum suppression**: After calculating the edge directions non-maximal suppression is carried out to trace along the gradient in the edge direction and compare the value perpendicular to the gradient. Two perpendicular pixel values are compared with the value in the edge direction. If these values are lower than the pixel value on the edge they are suppressed by changing their values to 0. Otherwise the higher pixel value is set as the edge and other two pixels are suppressed with a pixel value 0.

4. **Double thresholding**: After application of non-maximal suppression remaining edge pixels are quite accurate to present the real edge. However, there still remains some edge pixels which are caused by noise and intensity variation. In order to remove these unwanted edges, it is essential to preserve the edge with high gradient value and filter out edge pixels with low gradient. Two threshold values called high and low threshold values are selected for this purpose. Pixels stronger than the high threshold are marked as strong; edge pixels weaker than

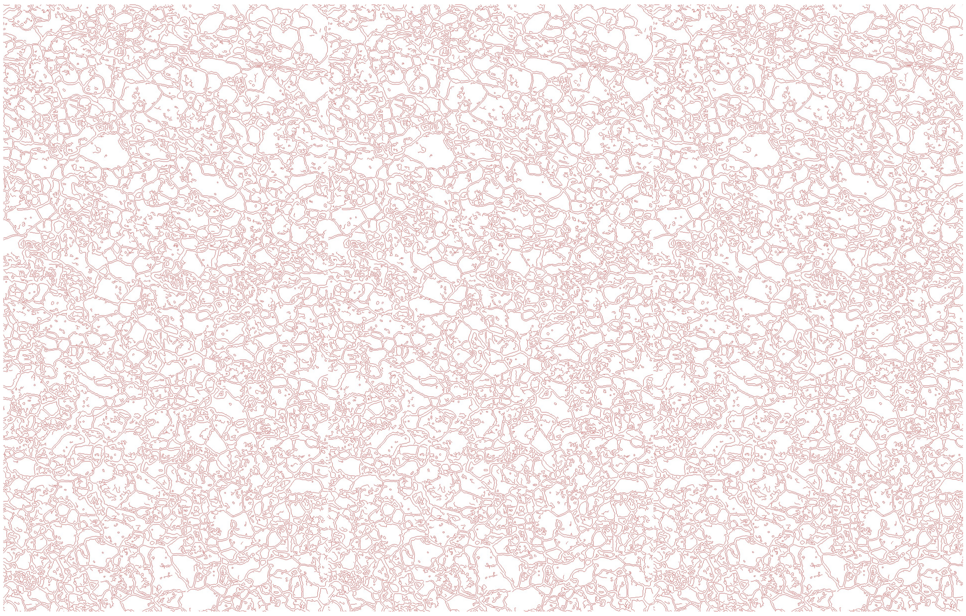

Fig. 2.3 Image after applying edge detection algorithm on the image in Figure 2.1(edges are shown in red).

the low threshold are suppressed and edge pixels between the two thresholds are marked as weak. Two threshold values are chosen empirically depending on the application image.

5. **Hysteresis**: Strong edges are immediately included in the final edge image since they are resulted from true edge of the images. But weak edges can either be extracted from true edges or due to the noise or intensity variation. Thus to achieve accurate result the weak edges resulting from noise or intensity variation should be removed. Usually, a weak edge pixel generated from true edges are connected with a strong edge pixel whereas noise response are disconnected. Thus a weak edge pixel is included in the final image if and only if they are connected to strong edges.

Figure 2.3 shows (edges are shown in red) the output after applying canny edge detection algorithm on the image in Figure 2.1.

Closed Contour Formation

It is quite likely that the detected edges do not form closed contours. It is attributed to the presence of weak boundaries with intensities close to that of the surroundings. A part of Figure 2.1 is magnified and shown in Figure 2.4(a) and its corresponding edge image is shown in Figure 2.4(b). It is observed that the edges are broken, double edges are generated for thick boundaries and lots of unwanted (spurious) edges are there. Measures are taken to address these issues and the steps are as follows.

- *Joining of Broken Edges:* As the first step, morphological closing operation [66] is applied on the edge pixels. The purpose is to connect the broken edges lying within a neighborhood. The structuring element of size 3×3 is considered. It is chosen small enough to restrict the possibility of spurious edges getting merged. Otherwise, such edges may qualify to form the boundary. The effect of this step is shown in Figure 2.4(c).
- *Handling Double Edges of Thick Boundary:* In the magnified image shown in Figure 2.4(b), it is clear that two edges on either side of the thick boundary are generated. If care is not taken then trapped region between such edges will erroneously be treated as grains. To surmount the problem number of steps are followed.
    - First of all, morphological dilation [66] with 5×5 structural element is applied on the detected edge pixels. As a result, such double edges are likely to get merged as shown in Figure 2.4(d).
    - The dilation operation results into thick boundary. Even after that there may exist small black patches trapped inside the boundary regions (white) as shown in Figure 2.4(d). It is essential to remove those to avoid misjudging those as grains. To remove these black patches, the mean area (μ_s) of the black regions (candidate grains) is calculated and tiny black regions are removed. Black patches with size smaller than a threshold are taken as tiny. The value of the threshold is experimentally determined as $0.10 \times \mu_s$. Such regions are marked as white to designate them as the boundary. The effect is shown in Figure 2.4(e).
    - Since the grain boundaries at this stage are thick enough, standard thinning algorithm [66] is used to make them single pixel width. Figure 2.4(f) shows the image obtained after thinning.
- *Removal of spurious Edges:* The edge detection algorithm detects some false edge as boundary due to intensity variation within grain. Such curves in most of the cases are unlikely to form a closed contour. At this stage the aim is to prune out such open curves and to retain only the closed contour. For this purpose a grain pixel (black) is selected as a seed and region growing [67] algorithm is followed. It recursively marks the pixels in the grain till the boundary pixels are encountered. The outer contour of the marked region provides the desired closed contour of the grain and also excludes the open and false edges present within the grain. The process continues for other grains by selecting another unmarked grain pixel as seed, if available. Thus the closed contour obtained is shown in Figure 2.4(g).

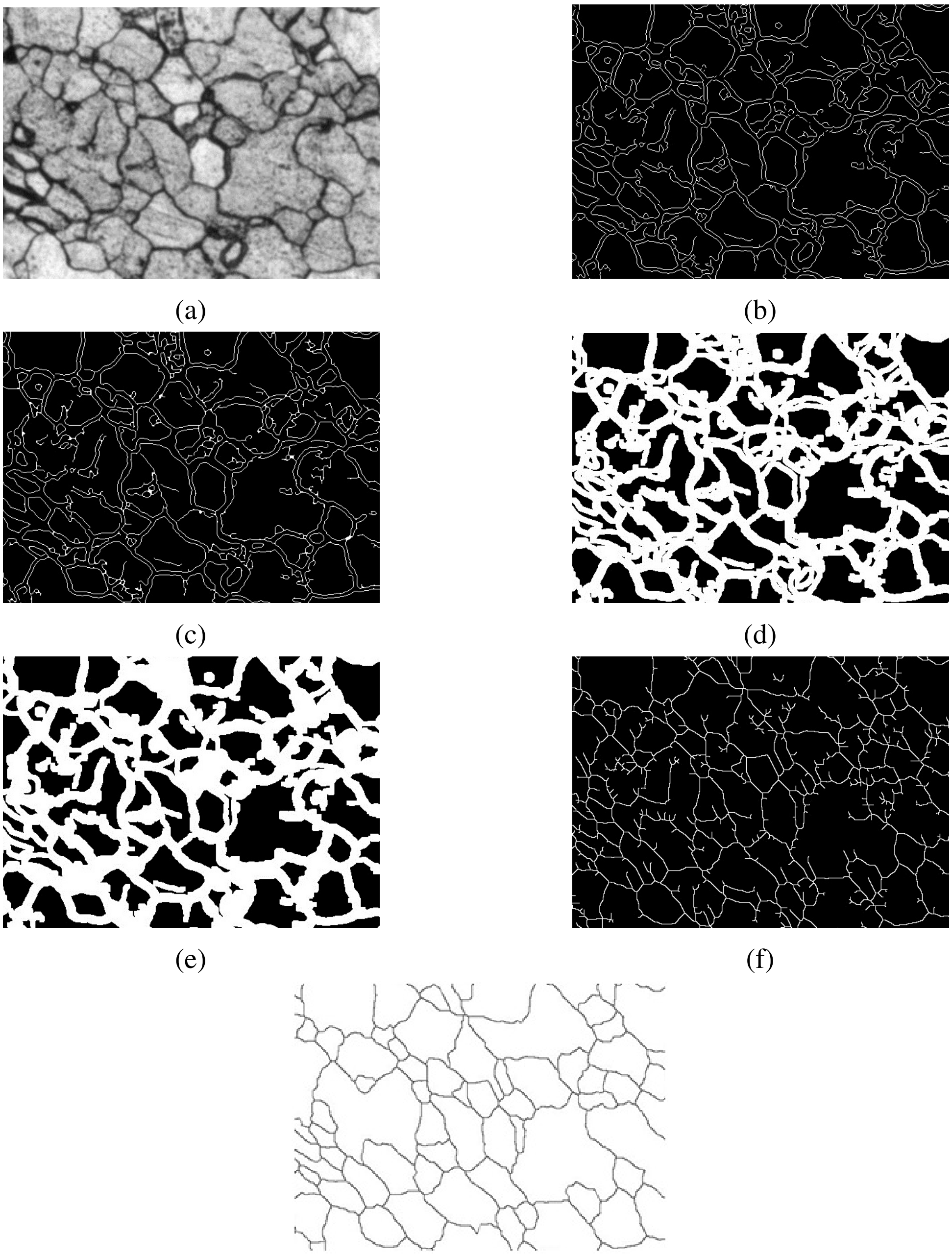

(a) (b)

(c) (d)

(e) (f)

(g)

Fig. 2.4 Step wise output of contour extraction process: (a) Magnified version of a part of the image in Figure 2.1, (b) Corresponding edge image, (c) Image after morphological closing (d) Image after morphological dilation, (e) Image after removal of small black patches, (f) Image after thinning and (g) Extracted contour image.

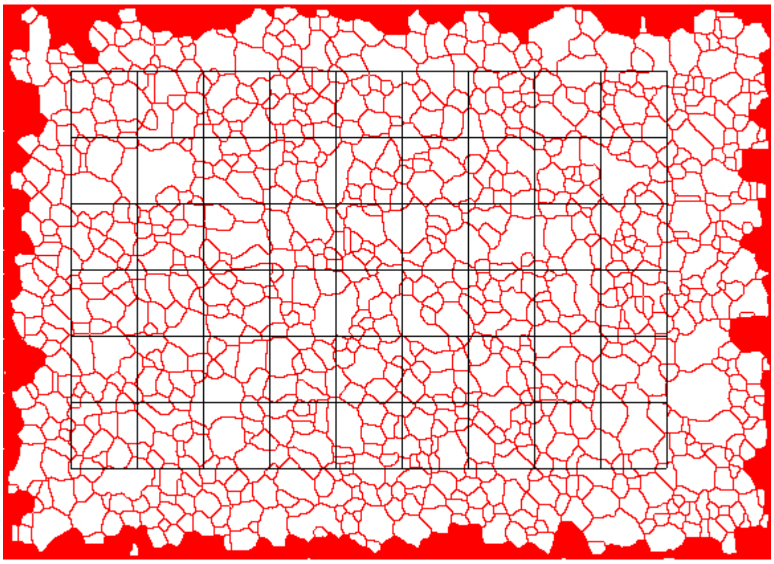

Fig. 2.5 Set of horizontal and vertical lines drawn on the micrograph.

2.3.2 Measurement of Grain Size Distribution

One of the methods for measuring the grain size distribution is Intercept Method [25, 26]. In this method, a line is considered along the micrograph. It is observed how many times the line intersects with the grain boundaries. P_L, the number of intercepts per unit length is then computed. The intercept length (l_i) is obtained as $1/P_L$. It is taken as the average grain size along the line. The process is repeated by considering n number of parallel lines. Finally, average of l_i provides the mean intercept length (l). The equation 2.3 relates the ASTM grain size number G and mean intercept length l.

$$G = -6.6457 log(l) - 3.298 \tag{2.3}$$

In our experiment, we have considered set of uniformly spaced parallel lines in horizontal and vertical direction as shown in Figure 2.5. Intercept length along each of the vertical and horizontal lines are computed for set of images. Average of all is taken as the mean intercept length (l) for the surface and G is calculated using equation 2.3. Incomplete grains in the field of view demarcated as red patch in Figure 2.5 have been ignored for grain size analysis.

Another popular method for calculating grain size is Planimetric method [25, 26]. As per ASTM standard, Planimetric method considers only the number of complete grains (N_i) within a known test area (A_i). It ignores the grains that intersect the test area border as those are likely to be part of grain. Once the count has been obtained, the number of grains per unit area (NA_i) can be estimated by equation 2.4. It is recommended to repeat the process with at least five images of the surface. The average of NA_i obtained from each image of the surface is taken as the grains per unit of area (NA). The average grain size (G) is computed following equation 2.5.

$$NA_i = N_i/A_i \tag{2.4}$$

$$G = 3.321928log(NA) - 2.954 \tag{2.5}$$

2.4 Experimental Result

The proposed algorithm has been applied on the optical micrographs of three different types of ineterstitial-free steels received from TATA Steel, Jamshedpur, India. The steels were in the form cold-rolled sheets. One large surface of these specimen coupons extracted from these steel were metallographically polished to completely scratch free condition and thoroughly cleaned with water and then in acetone and dried. Subsequently, the polished surface was chemically etched with Marshall's reagent. The polished and etched surface of the specimens was observed in a Leica make upright optical microscope (Model: Leica DM 2500M). A large number of images were captured from each these specimens using a Leica make digital camera (Model: Leica DFC550). The methodology developed in this work and discussed in Section 2.3 has been applied over these images to find the grain size of the steel and their distributions.

The result obtained has been compared with manually measured reference values, and also with that obtained by using Image J software and by following the method proposed in the work of Peregrina-Barreto et al. [37].

One representative micrograph of specimen 1 used in our experiment is shown in Figure 2.6(a). In this micrograph the grain boundaries are clearly observed and so also the grains. In general, micro-structure of this specimen consists of equiaxed grains of ferrite [70]. It is observed that the gain boundaries are of lower intensity than that of grain interior. As visually observed the grain intensity is almost homogeneous, *i.e.*, of low intensity variation, the classification of the image in two classes (grain interior and boundary) is relatively easier. The intensity histogram in Figure 2.6(b) shows a sharp and dominant peak which represents the grain intensity. The other peak at lower intensity range corresponds to the boundary. Thus intensity based threshold selection for segmenting the image into two classes (as used in Peregrina-Barreto et al. [37] and Image J software) is not difficult. The grains

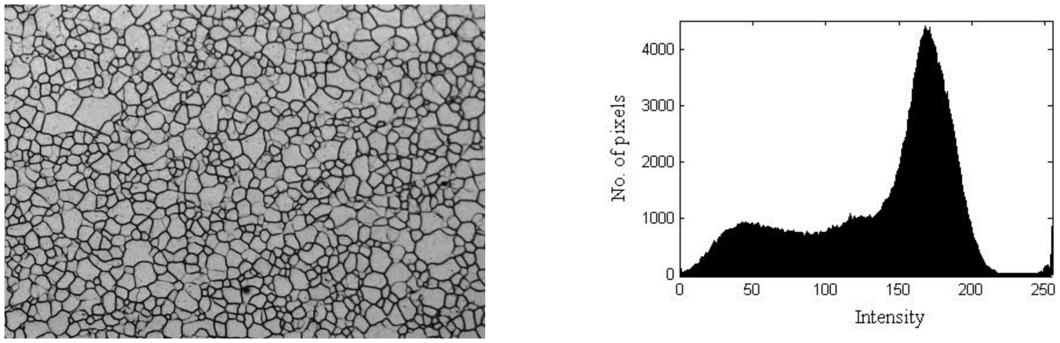

(a) (b)

Fig. 2.6 A representative micrograph of specimen 1, and (b) Intensity histogram of the micrograph.

Table 2.1 ASTM Grain size G measured by different methods for onefield of view of specimen 1 and 2.

			Proposed Methodology		
Figure	Method of Peregrina-Barreto et al. [37]	Image-J	Planimetric	Linear intercept	Reference Value
Specimen 1: Figure 2.6(a)	11	11	11	11	11
Specimen 2: Figure 2.8(a)	11	10	10	10	9

extracted by the proposed method, method of Peregrina-Barreto et al. [37] and Image J software are shown in Figure 2.7.

Figure 2.8(a) shows a micrograph of specimen 2. It is visually observed that unlike the image shown in Figure 2.6(a) the intensity of the grain interiors are not uniform enough. Moreover, there is intensity variation in different grains. The same is also clearly observed in the intensity histogram with multiple peaks in Figure 2.8(b). Thus the selection of threshold to separate the grain interior and boundaries is difficult. The grain boundaries extracted by three methods is shown in Figure 2.2. It is quite clear that the proposed methodology successfully extracts the boundaries whereas the performance of other two intensity threshold based methods is poor.

The measured ASTM grain size G for the proposed methodology and other two methods is listed in Table 2.1. Though for uniform image *e.g.* Figure 2.6(a), all the methods yield same result, images with non-uniformity (Figure 2.8(a)) might give rise to different results with different methods. It is worthwhile to mention that though proposed methodology and ImageJ have yielded same results, the use of ImageJ requires the manual selection of processing steps and parameters. But the use of proposed methodology does not require any kind of intervention. To come out with a real comparison among different methods, it is required to study a number of fields of any specimen. In this direction, we have considered twenty fields of specimen 2 and ten fields of specimen 3.

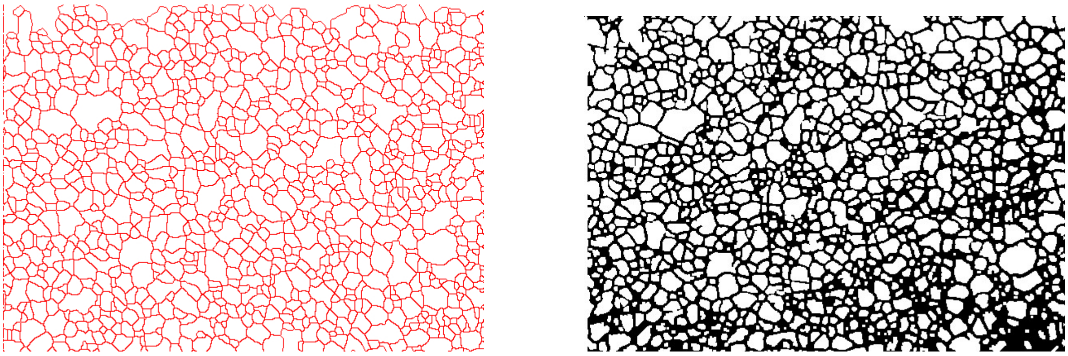

(a) Proposed method (b) Method of Peregrina-Barreto et al. [37]

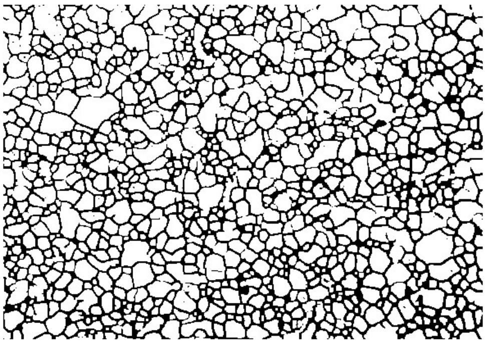

(c) Image J software

Fig. 2.7 Grain boundaries extracted by different methods from image in Figure 2.6(a).

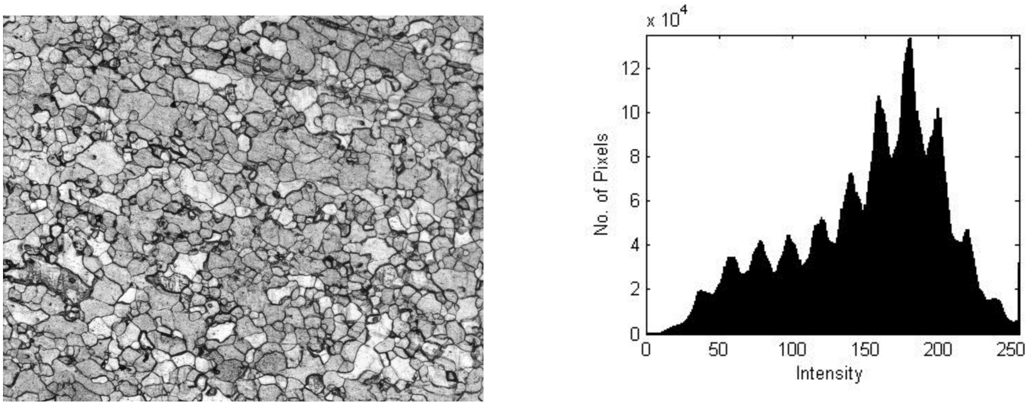

(a) (b)

Fig. 2.8 (a) A representative micrograph of specimen 2, and (b) Histogram of the micrograph.

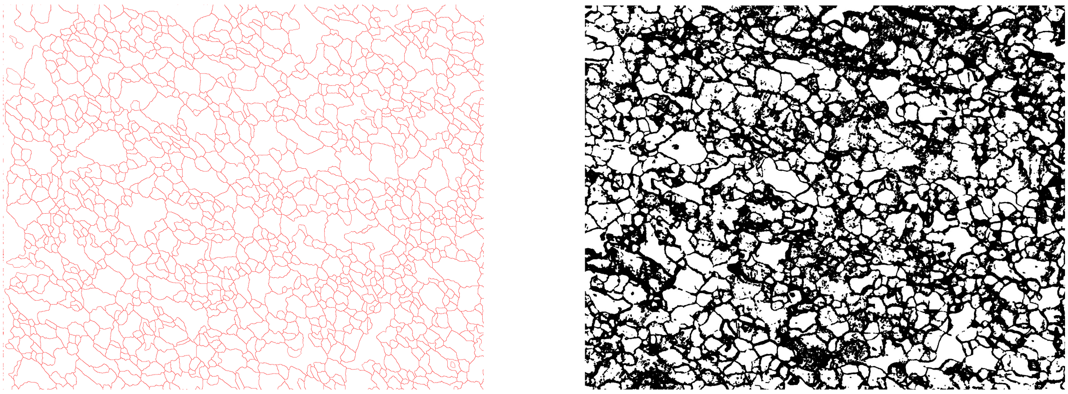

(a) Proposed method (b) Method of Peregrina-Barreto et al. [37]

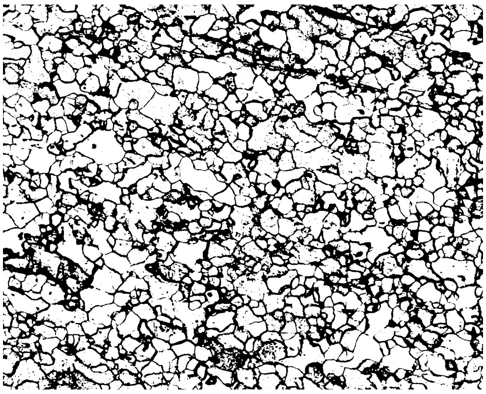

(c) Image J software

Fig. 2.9 Grain boundaries extracted by different methods from image in Figure 2.8(a).

Table 2.2 ASTM Grain size G measured by different methods for different fields of view of specimen 2.

			Proposed Methodology		
Fields	Method of Peregrina-Barreto et al. [37]	Image-J	Planimetric	Linear intercept	Reference Value
Field 1	11	11	10	10	9
Field 2	12	12	10	10	10
Field 3	11	10	9	9	9
Field 4	12	11	10	10	9
Field 5	10	10	10	10	9
Field 6	11	10	10	10	9
Field 7	12	11	10	10	10
Field 8	10	9	9	9	9
Field 9	11	10	10	10	9
Field 10	12	11	10	10	9
Field 11	12	11	10	10	9
Field 12	10	10	10	9	9
Field 13	11	11	10	10	9
Field 14	10	10	10	10	9
Field 15	11	11	10	10	9
Field 16	12	12	10	10	9
Field 17	10	11	10	10	9
Field 18	11	11	10	10	9
Field 19	12	12	10	10	9
Field 20	10	10	10	9	9

Table 2.3 ASTM Grain size G measured by different methods for different fields of view of specimen 3.

		Proposed Methodology			
Fields	Method of Peregrina-Barreto et al. [37]	Image-J	Planimetric	Linear intercept	Reference Value
Field 1	12	12	12	12	11
Field 2	13	12	12	12	12
Field 3	10	11	10	10	10
Field 4	11	10	10	10	10
Field 5	12	12	11	11	11
Field 6	13	13	12	12	12
Field 7	11	12	11	12	11
Field 8	12	12	11	11	11
Field 9	13	13	12	12	12
Field 10	12	12	11	11	11

Table 2.4 Measured ASTM Grain size G on a set of micrographs of specimen 2 and 3.

		Proposed Methodology			
Specimen	Method of Peregrina-Barreto et al. [37]	Image-J	Planimetric	Linear intercept	Reference Value
Specimen 2	11	11	10	10	9
Specimen 3	12	12	11	11	11

As shown in Table 2.2, the ASTM grain size G measured by the method of Peregrina-Barreto et al. [37] varies from 10 to 12 for these 20 micrographs, whereas the estimation of G using Image J software varies from 9 to 12 over these twenty fields. In the proposed method it varies from 9 to 10. Similarly, ten fields of view of specimen 3 have been considered by all the three methods. A representative micrograph of specimen 3 has been shown in Figure 2.10. Over these ten fields the average grain size (G) varies from 10 to 13 for the methods of Peregrina-Barreto et al. [37] and ImageJ software. For the proposed method the result varies between 10 and 12. The result is shown in Table 2.3. The average grain size measured on the fields of specimen 2 and specimen 3 are listed in Table 2.4. The mean (μ) and standard deviation (σ) of ASTM grain size error with respect to reference values are calculated for specimen 2 and specimen 3 and are given in Table 2.5. For each specimen average and standard deviation of error are computed considering all the fields of the corresponding specimen. It is found that the measurement done by the proposed methodology is closer to the reference value.

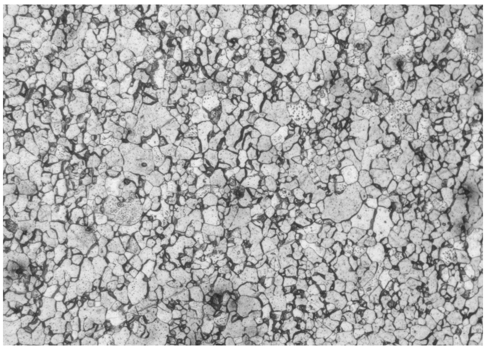

Fig. 2.10 A representative micrograph of specimen 3.

Table 2.5 Error estimation in measured ASTM Grain size G for specimen 2 and 3 with respect to reference value.

					Proposed Methodology			
	Method of Peregrina-Barreto et al. [37]		Image-J		Planimetric		Linear intercept	
Specimen	μ	σ	μ	σ	μ	σ	μ	σ
Specimen 2	1.95	0.74	1.60	0.74	0.80	0.40	0.70	0.46
Specimen 3	0.80	0.40	0.80	0.40	0.10	0.30	0.20	0.40

Further it is observed that as expected the grains are of varying size in the investigated microstructures. The present methodology offers to find the grain size distribution in terms of grain area without any additional effort. The range of grain area present in a specimen has been divided into number of bins with bin size 5 μm^2. To obtain the distribution, grains of very small area and those of very large area have been ignored. In the present study top and bottom most 5% of the grains in terms of area have not been considered. The representatives of five fields of specimen 2 and their distribution are shown in Figure 2.11(a)-(e) and Figure 2.11(f)-(j). The average distribution of grains over 20 micrographs of the specimen2 is shown in Figure 2.11(k).

Figure 2.11 reveals that even in a particular specimen there is variation of grain size in different fields of view and it is not unnatural also. It is thus always required to measure the grain size over a large area and represent the size with no fixed value. In the specimen 2, it is found that the average grain area over twenty fields actually varies between 70 to 105 μm^2. The same investigation is also applied over ten fields of specimen 3 and the average grain area varies between 45 μm^2 and 53 μm^2.

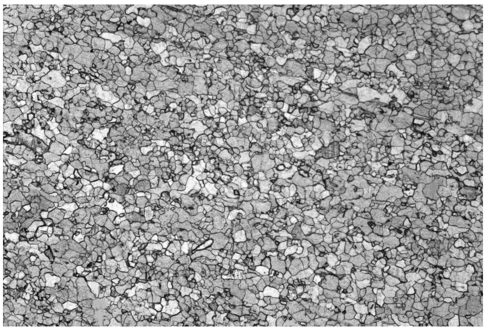

(a)

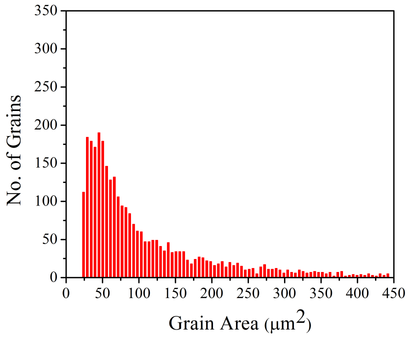
No. of Grains
0
50
100
150
200
250
300
350
0 50 100 150 200 250 300 350 400 450
Grain Area (μm^2)

(f)

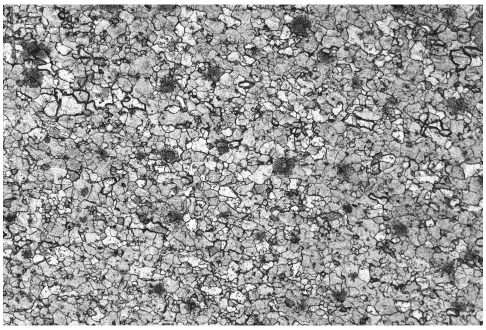

(b)

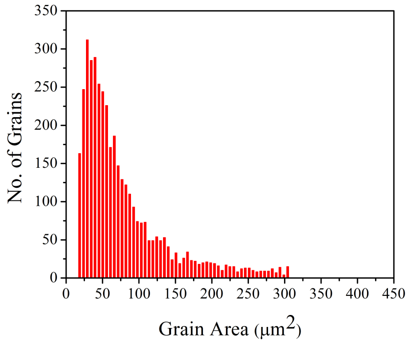
No. of Grains
0
50
100
150
200
250
300
350
0 50 100 150 200 250 300 350 400 450
Grain Area (μm^2)

(g)

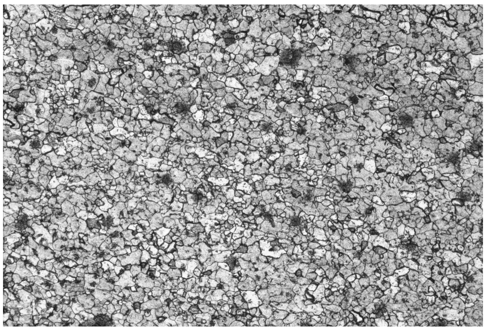

(c)

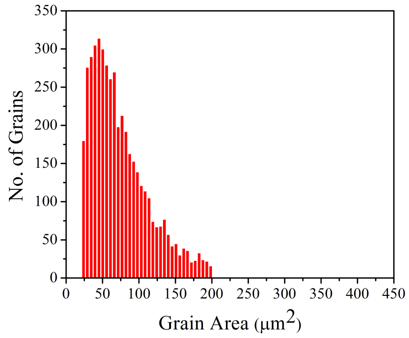
No. of Grains
0
50
100
150
200
250
300
350
0 50 100 150 200 250 300 350 400 450
Grain Area (μm^2)

(h)

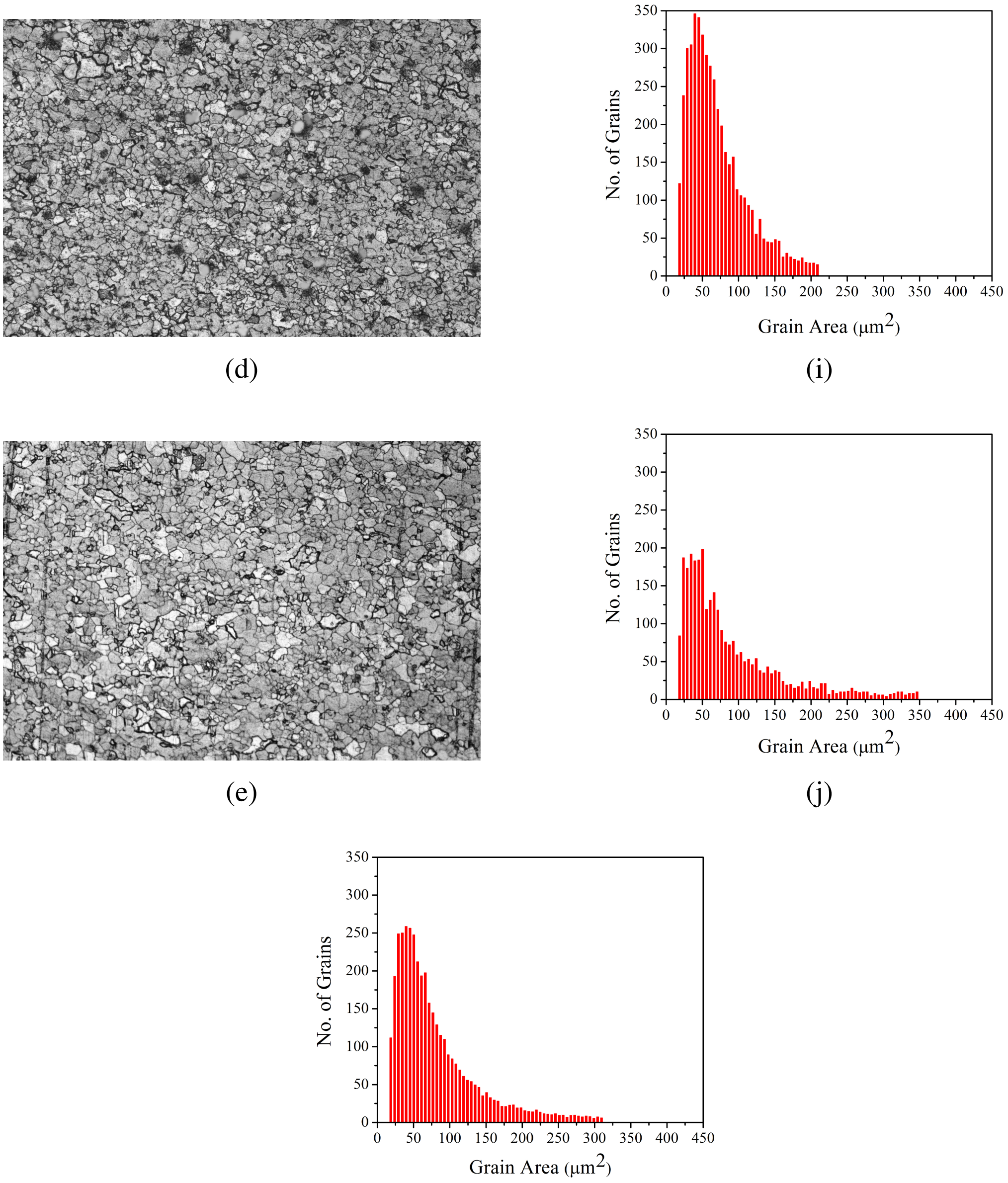

(d) (i)

(e) (j)

(k)

Fig. 2.11 (a) - (e) Five Micrographsof Specimen 2, (f) – (j) Distribution of grains of those five micrographs and (k) Average grain distribution of 20 micrographs of Specimen 2.

2.5 Summary

The proposed automated methodology extracts the closed contours of the grains present in the micrograph. Despite the intensity variation within the grain and similarity between the intensities of grain boundary and grain interior, closed contours obtained by present methodology can well approximate the actual grain. The proposed methodology performs well in extracting the grains in a wide variety of steel micro-structures. The computed grain size is found to be very close to ASTM reference value. The performance has also been compared with other methods which consider the commonly used threshold based segmentation. It is observed that the present methodology has the capability for proper segmentation of the grains. The proposed segmentation methodology can also be used as a convenient tool for other microstructural analysis such as grain shape and phase morphology.

Chapter 3

Phase Identification and Phase Volume Fraction Measurement

3.1 Introduction

Mechanical properties of a material are known to be structure sensitive. Besides mechanical properties, other properties, corrosion, as an example, are also known to be structure sensitive. It is worth mentioning here that by the term "structure sensitive" we focus on micro-structure of materials, which is an aggregate of different phase(s). Depending upon thermal and/or mechanical processing the micro-structural evolution of any material of fixed chemistry can widely vary. Concomitant with the variation of micro-structure different combination of material properties can be designed. The modulation of micro-structure vis-à-vis the changes of properties is one of the prime concerns to material scientists/engineers. However, such modulation of micro-structure in multi-phase materials depends solely on the phase changes associated with thermal/thermo-mechanical processing.

The phase change/transformation vis-à-vis the development of micro-structure needs to be studied deeply to correlate different properties with processing parameters. To define the micro-structure of any multi-phase materials it is necessary to know the relative volume fraction of the different phases, their size, shape and distribution. Any change of any of these parameters can alter the properties of a material, and sometimes the changes could be dramatic. This lays the thrust on characterizing the micro-structure of any material; a detailed knowledge of which can also lead to tinker the processing parameters to achieve the best combination of properties. The complete domain right from processing to characterizing micro-structures to evaluation of properties is at present known as "micro-structural engineering" or "designing of materials through micro-structural engineering". In this direction quantification of micro-structural parameters is of extreme importance and hence demands attentions.

3.2 Past Work

The quantification of phase volume fractions is commonly and almost routinely done by using the light microscopic images or scanning electron microscopic images of the micro-structure. Before phase quantification it is necessary to develop micro-structure of the material using small specimens which are metallographically polished and etched to develop the micro-structural details following standard metallographic procedure. It should be noted that the entire procedure in preparing the specimen is manual in nature.

The microscopes are nowadays integrated with digital camera and the images captured by this camera are stored in a personal computer. The digital images of micro-structures are used for characterizing the micro-structure including the relative volume fraction of the phases. Common image analyzing software is generally used for this purpose. The analysis of micro-structure for relative volume fraction of the phases is based on the grey level of different phases/constituents that develops depending upon the etching reagent and phase characteristics. But, only grey level based analysis poses difficulties many a time in determining the phase volume fractions. This difficulty primarily arises out of very small variation in the grey level characteristics within/between the phases, and also in complex structure where different phases, but with almost similar grey level (or with no variation in grey level) remain finely intermixed. Hence, there remains a challenge in such critical conditions to delineate different phases and determine the relative phase volume fraction. Keeping all these challenges in mind, the methodology for automated measurement mostly comes down to the task of image segmentation.

It is observed that very few efforts have been made to automate the segmentation of micro-structures and measuring the volume fraction of the phases present. Furthermore, the methodologies adopted are material specific. It has already been discussed the micro-structures varies from material to material and also it varies with different processing parameters. Hence devising an automated system applicable for all cases is very difficult. It has motivated the researchers to customize the systems for specific scenarios.

Komenda [40] proposed a scheme where an image classifier has been integrated with *context vision* [41]. It facilitates contextual analysis (*i.e.* spatial dependencies among the regions) for extracting the areas of interest. But, such analysis incurs computational cost. Moreover, the classification accuracy heavily depends on proper training. Neural network also have been tried to classify the phases of an alloy [42]. A comparative study has been done between multi-layer perceptron and self-organizing map topologies for segmenting micro-structures in metallographic images. In this work, multi-layer perceptron neural network was trained using supervised back propagation algorithm and training of self-organizing map neural network was based on the unsupervised Kohonen algorithm. The network is trained using sixty samples of cast irons and the results obtained by multilayer perceptron neural network were very similar to the ones obtained by visual human inspection. It is worth mentioning that for such supervised techniques, sufficient samples are required for proper training. Chatterjee et al. [43] presented an image processing based automated system that considered intensity based thresholding to differentiate the phases present in high strength low alloy (HSLA) steel. To refine the measurement, phase boundaries which might have intensity values similar to one of the phases present, were identified as thin region and ignored in measurement. Gruttadauria et al. [44] utilized Image Pro Plus software to identify the phases which also differentiated the phases based on intensity. Paulic et al. [72] measrured volume fraction of graphite, ferrite and ausferrite are calculated using threshold based technique. Salem et al. [73] analyzed Ti6AlV4 microstructure data by learning the phase patterns. Campbell et al. [74] also worked with Ti6AlV4 specimens. Watershed transform followed by a merging technique had been used for region segmentation. In each region, phases were identified by using thresholding. Deep learning has been tried by Azimi et al. [75]. But it requires large data repository for proper learning. Graylevel co-occurrence based textural properties were considered by Naik et al. [76] for phase identification. Yang et al. [77] quantify alpha and beta phase in dual-phase Ti-6Al-4V titanium using Image-Pro Plus software.

Commercially available software mostly rely on intensity based thresholding and option is provided to the user to select the threshold. But the brief discussion reveals that the problem is not that trivial. Threshold based scheme fails to consider within phase intensity variation and any other structural criteria. As a consequence, more rigorous segmentation scheme becomes essential.

The objective of the present chapter is to present automated methodologies to quantify phase volume fractions in different micro-structures of two different materials, namely, *dual-phase steel* and *titanium alloy*. For each material a number of micro-structures developed by varying the processing parameters have been investigated. The methodologies for the two cases are elaborated in Section 3.3 and 3.4 respectively.

3.3 Case I: Dual-Phase Steel

In this work, we have dealt with SEM images of dual phase steels consisting of two distinct phases, soft polygonal ferrite matrix along with the distribution of hard martensite second phase in

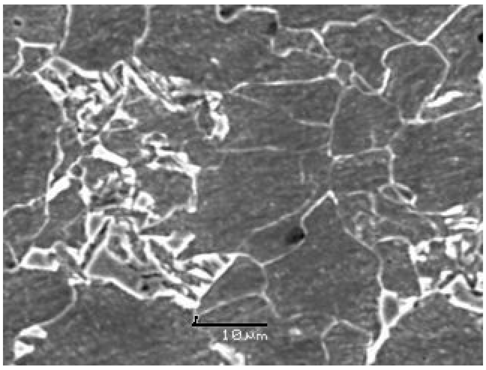

Fig. 3.1 A Sample dual phase steel micrograph.

the form of island. Images of the samples, polished and etched with 2% Nital, were carried out by Scanning Electron Microscope (Model: Hitachi S3400N), in secondary electron mode, at various magnifications. The ferrite grains with black appearance cover the major part whereas the sparsely distributed second phase appears as white blobs (see Figure 3.1). Thus, the task can be mapped onto the classical problem of segmenting the background and foreground.

3.3.1 Proposed Methodology

Apparently it seems that conventional approach of intensity based thresholding can identify the two phases. But, numbers of challenges are there making the problem non-trivial. The issues are as follows.

- The grain boundary also possesses the similar intensity (white in our case) as one of the phases (martensite).
- Martensite components may not possess uniform intensity. Even it may have ferrite like intensity values trapped inside.
- A single martensite component may appear as a collection of splitted sub-components.

The boundaries are to be identified and excluded. A closed contour of the white phases encompassing the nearby sub-components has to be formed. Otherwise the white grain boundaries and the black segment within the martensite laths will disturb the phase identification and phase quantification process. The broad steps to accomplish the tasks are as follows.

- Initial segmentation.

- Phase formation.
- Phase refinement.

The steps are detailed in the following sub-sections.

Initial segmentation

It has been observed that intensity values of the pixels in two phases can be broadly categorized as black and white. Thus, the primary target is to binarize the given image. As the boundary pixels are also white, the removal of the same is taken up with the binarized image. The steps for initial segmentation are as follows.

- smoothing.
- Thresholding.
- Boundary removal.

The micrograph may not reflect strong contrast between the two phases. The ferrite grains are not uniformly black. It contains variation. Same is also true for the martensite phase. Due to the limitation imposed by image acquisition environment and surface undulation, such variations and/or noise may creep in. To minimize such effects we perform pre-processing prior to thresholding. 5×5 mean filter is applied to smoothen the image.

Thresholding is applied on the smoothened version of the original image. Based on the intensity histogram, a threshold, th is chosen. Pixels with intensity higher than th are considered as white and black otherwise. Selection of th is important, as the phases show considerable variation and contrast is also not very high always. We have relied on thresholding scheme proposed by Otsu [64]. As the histogram for the micrographs are bimodal in nature, Otsu algorithm is well suited. The optimal threshold is chosen in a way to minimize the intra-class variance. The Otsu method is non parametric and unsupervised method that select threshold automatically. An optimal threshold is chosen such a way that the separability of the resultant classes in gray level is maximized. The procedure utilizes upto second order cumulative moments of the gray level histogram to select the threshold value. The procedure is given below.

Assume that the pixels of the given image are represented by L gray levels $\{1, 2, ..., L\}$. The number of pixels at level i is denoted by n_i and total number of pixels in the image is designated by $N = n_1 + n_2 + ... + n_L$. To find the threshold the following steps are followed

1. Normalize the Gray level histogram using following equation and considered it as a probability distribution function.

$$P_i = n_i/N \quad where \quad p_i \geq 0 \quad and \quad \sum_{i=1}^{L} P_i = 1 \tag{3.1}$$

2. Separate the image into two classes C_0 and C_1 (back ground and foreground) by a threshold at level k; where C_0 denotes pixels with level $\{1,2,...,k\}$ and C_1 denotes pixels with level $\{k+1,k+2,...,L\}$. Calculate the class occurrence and class mean level using following equation.

$$\begin{aligned} w_0(k) = Occurence \quad of \quad class \quad C_0 &= \sum_{i=1}^{k} P_i \\ w_1(k) = Occurence \quad of \quad class \quad C_1 &= \sum_{i=k+1}^{L} P_i \end{aligned} \tag{3.2}$$

and

$$\begin{aligned} \mu_0(k) = Mean \quad of \quad class \quad C_0 &= \sum_{i=1}^{k} \{i.P_i\}/w_0(k) \\ \mu_1(k) = Mean \quad of \quad class \quad C_1 &= \sum_{i=k+1}^{L} \{i.P_i\}/w_1(k) \end{aligned} \tag{3.3}$$

3. Calculate the class variance of both classes using following equations

$$\begin{aligned} \sigma_0^2(k) = \sum_{i=1}^{k}(i-\mu_0(k))^2.P_i/w_0(k) \\ \sigma_1^2(k) = \sum_{i=1}^{k}(i-\mu_1(k))^2.P_i/w_1(k) \end{aligned} \tag{3.4}$$

4. In next step within-class variance is calculated which is sum of the two variance multiplied by their associated occurrence, i.e.

$$\sigma_w^2(k) = w_0(k).\sigma_0^2(k) + w_1(k).\sigma_1^2(k) \tag{3.5}$$

5. Repeat Step 2 to Step 4 to find k for $k = 1,2,...,L$ that maximizes $\sigma_w^2(k)$.

The thresholded image corresponding to the image in Figure 3.1 has been shown in Figure 3.2.

It may be noted that in the thresholded image the pixels forming the inter ferrite grain boundaries also take part in the process of binarization and appear as white. But, the grain boundaries are thinner with respect to the actual martensite phase regions. Based on these observations, we have applied morphological opening operation [67] to get rid of thin boundary segments. Opening operation consists of morphological erosion followed by dilation. Let size of the structuring element (SE) for morphological operation be S×S. In order to erode the binary image, the centre of SE is placed on

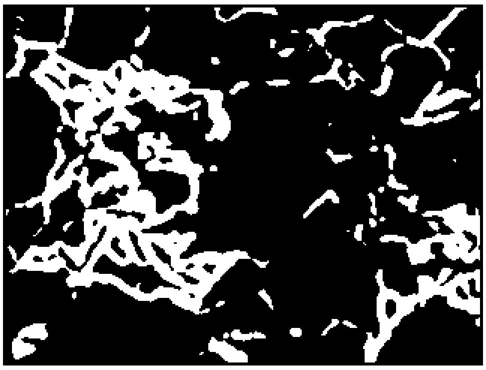

Fig. 3.2 Image after Thresholding.

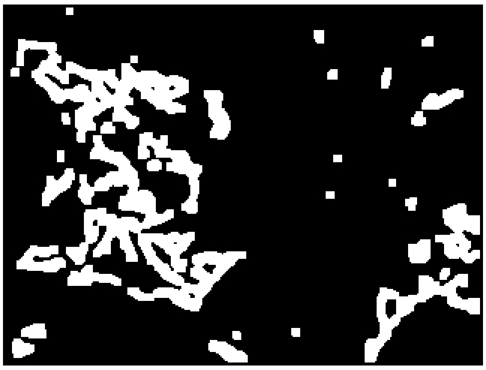

Fig. 3.3 Image after boundary removal.

a pixel and in the eroded image; the corresponding pixel is converted to a black one if any of the pixels covered by SE in the binary image is black, otherwise white. Thus the grain boundaries being thinner get removed. White regions retained after erosion also get shrinked and in order to retain their original size, dilation is carried out with the eroded image. Centre of the SE is placed on a pixel of eroded image. The corresponding pixel in the dilated image is white if any of the pixels covered by SE in the eroded image is white, otherwise black. In our experiment, 5×5 structuring element has been considered for opening operation. Thus, the output after boundary removal operation on image in Figure 3.2 has been shown in Figure 3.3.

Phase formation

After initial segmentation, we take up the task of formation of the white phases. Martensite phase may not have uniform high intensity all over the region that it covers. As a result black regions may be trapped in inter-lath positions and also may be splitted into multiple white components as evident in Figure 3.3. Thus, the white components with in the neighbourhood are to be linked and closed contour encompassing the linked components has to be formed to develop a continuous martensite region. Disjoint white components are first identified and labeled using following component labeling [67] algorithm.

1. An arbitrary white pixel (x, y) is chosen from the image, which is known as seed pixel.
2. This pixel is given a unique label UL.
3. 4-neighbouring pixel of the seed pixel is examined. The neighbor(s) which are white are also assigned the unique number UL. Once a new pixel is considered as a member, the 4-neighbors of this new pixel are examined. This process continues until no more pixels is accepted. All the pixels of the current region are marked with UL.
4. Repeat Step 1 to Step 3 until every white pixel is assigned to some region.

A component C_i is linked with another component C_j if either of the following conditions is satisfied.

- C_i and C_j lie within a neighbourhood.
- Bounding box of C_i includes major part of C_j.

In order to link the components, the procedure evolves as follows.

- Consider an array P and initialize each element $P(r, c)$ as black.
- For each component C_i.
    - Dilate [67] the component by a structuring element of size K×K to obtain C_{id}.
    - Mark $P(r, c)$ as white for $(r, c) \in C_{id}$ if C_{id} touches/enters C_j and $(i \neq j)$, otherwise black for $(r, c) \in C_i$.
- Perform component labeling on P.
- Consider an array F and initialize each element $F(r, c)$ as black.
- For each component C_i in P.
    - Consider an array $temp$ and initialize each element $temp(r, c)$ as black.
    - Find the bounding box bb_i of C_i.

  - S be the set of components C_j whose $p\%$ area or more lies within bb_i.
  - Compute the bounding box BB_i encompassing all components $C_j \in S$.
  - $temp(r,c) = P(r,c)$ if $(r,c) \in BB_i$.
  - Execute procedure $closed\_contour(temp)$ and store output in the array CC.
- Mark $F(r,c)$ as white for all (r,c) such that $CC(r,c)$ is white
- F is taken as the output

As it has been indicated in the algorithm, it deals with two major steps. At first level, a component is dilated to identify and link the neighboring components. In our experiment, size of structuring element has been empirically chosen as 5×5. It should neither be too low nor be too high. Along with linking, dilation also helps to smoothen the contour of the component itself that may arise out of non-uniform intensity variation around the contour leading towards omission in thresholding process. Effect of dilation is ignored if it fails to link a component with others. As a result unnecessary growth of the components is also avoided. After such linking, components are relabeled. The second stage of algorithm proceeds with the newly labeled components. At this stage, the neighborhood is defined differently in terms of the bounding box. Presence of low intensity within the white phase may split it in a manner which fails to satisfy the first criteria. Bounding box based definition of neighbourhood addresses these cases. For each component, the minimal bounding box is determined and other components whose major area (in our, experiment it has been taken as at least 50%) falls within the same bounding box are considered as the components to be linked. $closed\_contour()$ procedure is carried out on the bounding box encompassing all the components to be linked. The technique has been elaborated in [78, 79]. It approximates the contour as the pseudo convex hull of the object. The procedure finally generates a closed contour by combining the components and it also removes the shaded region trapped inside.

Let B be the image where $B(r,c) = BB_i(r,c)$ if $(r,c) \in BB_i$ else $B(r,c) = 0$. The steps for the procedure $closed\_contour(B)$ are as follows.

1. Take four other arrays $H(i,j)$, $V(i,j)$, $D1(i,j)$ and $D2(i,j)$ of same size as that of $B(i,j)$, and initialize them with one.
2. For each row of $H(i,j)$
   (a) Start from first column, change its pixel value to zero and move right until $B(i,j) = 1$ or the last column is reached.
   (b) If the last column is not reached then start from last column, change pixel values to zero and move left ward until $B(i,j) = 1$.

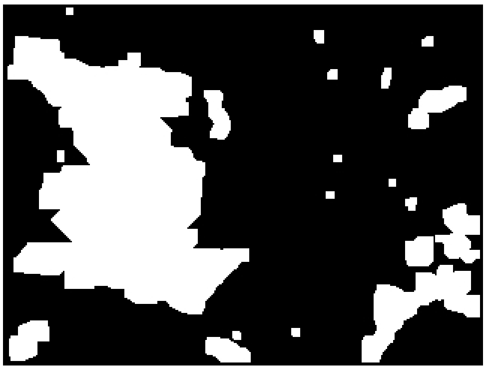

Fig. 3.4 Image after phase formation.

3. Now repeat sub-steps of 2 for $V(i,j)$, $D1(i,j)$ and $D2(i,j)$ with appropriate directions i.e., upward and downward for V and along the two principal diagonals for $D1$ and $D2$.
4. Finally, produce a binary image $F(i,j)$ that contains the pseudo convex hull of the given image B as follows:

$$F(i,j) = \begin{cases} 1 & H(i,j)+V(i,j)+D1(i,j)+D2(i,j) > th \\ 0 & otherwise \end{cases} \tag{3.6}$$

The binary image of which closed region is required is scanned in four directions. Scanning starts from image boundary and goes on marking the pixels as background till it encounters the foreground pixel *i.e.* object boundary. In case there is a discontinuity in the object contour, scan lines may intrude inside the object. Such intrusion varies for different scan directions. Depending on the degree of discontinuity and value of th, such open regions are approximated to form a closed region. Physically, th denotes at least from how many directions a boundary pixels of the foreground object can be reached. In our experiment, th is taken as 2. Thus, a continuous white phase with smooth contour is approximated. The pixels $F(i,j)$ with value 1 constitute the phase. Output corresponding to the image in Figure 3.3 has been shown in Figure 3.4. Now we get the image free from grain boundaries between the ferrite grains and also with distinct martensite regions.

Phase refinement

Once the white phases are formed, we carry out post-processing activities. It consists of two steps as follows.

- Phase linking.

Fig. 3.5 Image after phase refinement.

- Small component removal.

During phase formation stage, components within proximity have been merged together. At this stage, possible merging of phase regions is taken up. Bounding box based criteria can lead to undesirable phase linking. As phase has been already formed by extending the components, a strict approach is followed at this stage. A white phase region is dilated by a $K \times K$ structuring element.

In our experiment K is taken as 5. If because of dilation at a point, the region gets connected with another then effect is retained otherwise previous state is maintained by canceling the growth. In case regions are merged, there is a possibility that black phase may be trapped inside. To remove those, region filling algorithm is applied.

Because of noise, thresholding and other practical limitations small white regions may be formed. Such regions are removed based on the size analysis of the detected regions. Regions with size smaller than a threshold, t_s are removed. t_s is taken as $max(\mu_s - \sigma_s, 0.1\mu_s)$. μ_s and σ_s are the average and standard deviation of the region sizes. After post-processing, the final output corresponding to the image in Figure 3.4 has been shown in Figure 3.5.

3.3.2 Experimental Result

In order to carry out the experiment, we have considered 12 dual phase steel micrographs. They vary in terms grain size and concentration, magnification and illumination level. Such collection has enabled us to judge the robustness of proposed scheme. Representative outputs are shown in Figure 3.6.

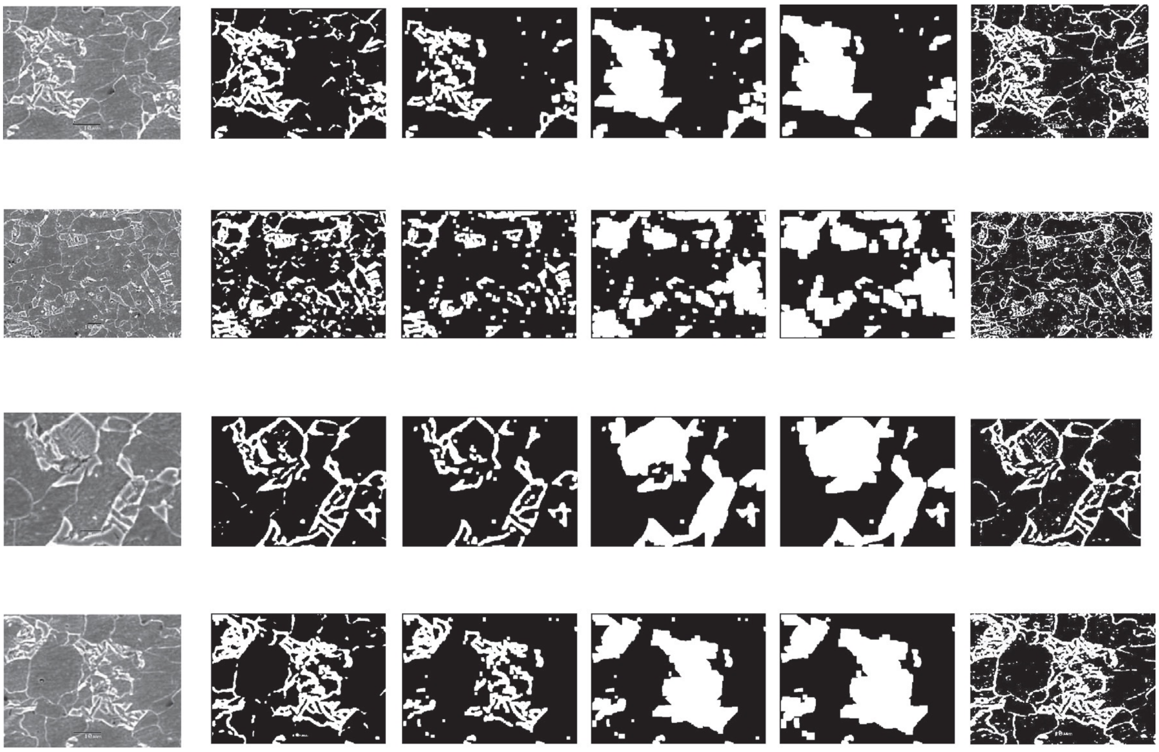

(a) (b) (c) (d) (e) (f)

Fig. 3.6 Few sample results : (a) original grayscale image, (b) image after thresholding, (c) image after boundary removal, (d) image after phase formation, (e) image after phase refinement and (f) image after analysis using Olysia software.

Table 3.1 Volume fraction of the two phases at different stages of processing.

	After thresholding		After Boundary Removal		After Phase Formation		After Phase Refinement		From Olysia Software	
Image	White	Black	White	Black	White	Black	White	Black	White	Black
Image 1	.22	.78	.17	.83	.28	.72	.32	.68	.26	.74
Image 2	.29	.71	.21	.79	.34	.66	.40	.60	.22	.78
Image 3	.19	.81	.17	.83	.33	.67	.37	.63	.21	.79
Image 4	.23	.77	.19	.81	.31	.69	.34	.66	.29	.71

To measure the segmentation performance, we have compared the result with ground-truth information. As white martensitic regions are interfered by the boundaries, analysis is also focused on it. It has been observed that the proposed scheme successfully discards the grain boundaries. Table 1 shows the fraction of white (martensite) and black (ferrite) phases as obtained at the various stages of processing for the samples shown in Figure 3.6(b)-(e). As expected the phase fraction of the white phase decreases significantly after the grain boundary removal (Figure 3.6(c)). But still the volume fraction of the black phase includes inter lath dark regions of the martensite, may be due to the formation of low angle grain boundaries. Due to the joining of white region and formation of phase contour of the martensite phase, the volume fraction of the phase increases in subsequent steps (Figure 3.6(d) and 3.6(e)). The changes in the volume fraction of each phase in every step, shown in Table 3.1, indicate the importance of all operations on the image. Figure 3.6(f) shows the results after analyses using standard software used for analyses and quantification of micrographs (Olysia). The images seem to be almost similar to the images formed after the thresholding step using the present scheme. This actually justifies the steps used after the thresholding to actually recognize and compute two separate phases distinctly. The volume fractions of martensite as calculated by the Olysia software are also depicted in the Table. This also clearly shows the amount of error present in the result using only thresholding operation. It is evident in Figure 3.6 that the proposed methodology can well approximate the phase regions even in presence of intensity variation within a phase which a simple threshold based scheme cannot. The implication of the methodology towards the volume fraction of the phases is also well reflected in Table 3.1. The results also show that present method is superior to the methods applied by the conventional software, and can serve as a practical approach for analysis and quantification of SEM images. The method, as evident from the above results, is not specific for dual phase steel only. It may be applied to many other steel or even other materials, where the micro-structure contains such areas of confusion, as in this case where pixels values of several regions within the second phase matches with that of the primary phase (ferrite) due to higher resolution of the microscope through which the images are grabbed. But the idea has to be practically verified in future.

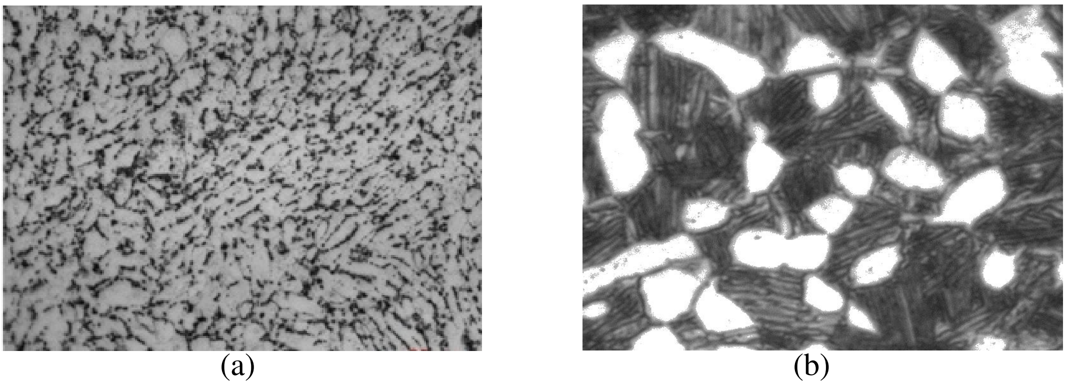

Fig. 3.7 (a) Micro-structure of the material received in the mill annealed condition and (b) Partial view of micro-structure after heat treatment (magnified version).

3.4 Case II : Titanium Alloy

The present work aims for quantitative description of a heat treated Titanium alloy which is an important α/β alloy and finds application in aerospace industry. The micro-structure of the material received in the mill annealed condition is shown in Figure 3.7(a). In the gray scale image brighter (white) regions correspond to α phase and the darker (black) ones belong to β phase. The received sample is heat treated to develop bi-modal structure consisting of primary α and transformed β phase as shown in Figure 3.7(b). It shows the micro-structure of a particular field of view of the sample in magnified form. In this image the dark etching constituent is the transformed lamellar matrix consisting of fine distribution of alternating α and β lamellae. The task is to extract the phases and quantify their relative volume fraction. Island like white regions form the primary α phase and rest are transformed α/β lamellar matrix. Within the transformed phase also α (henceforth referred as secondary α) and β are to be identified.

3.4.1 Proposed Methodology

It is worth noting that the primary α and that in the lamellar matrix are of similar intensity (both are white) and hence only intensity based thresholding will not serve the purpose. Hence, apart from such thresholding, proposed methodology performs further processing to meet the requirement. The broad steps are as follows.

- Detection of primary α phase
  - Intensity based thresholding

  - Removal of secondary α
  - Final segmentation of primary α
- Detection of secondary α and β

Detection of primary α phase

As shown in Figure 3.7(b), primary α and secondary α phases share similar intensity. Hence, only intensity based thresholding can not separate them. Hence, as discussed earlier number of steps are required to achieve the desired goal. The steps are detailed as follows.

Intensity based thresholding: At this stage our goal is to classify the micrograph pixels into two classes based on their intensity values. Primary and secondary α phases are brighter and β phases are of lower intensity. Thus, in the binarized image α phase will appear as white and β phase will be black. Based on the intensity value of the pixels, a threshold is to be chosen. Otsu [64] technique is used for selecting the threshold. Otsu method is applied since the intensity histograms of the micrographs are of bi-modal nature. Furthermore, the method is non parametric and unsupervised. It provides an optimal threshold and the separability of the resultant classes in gray level image is maximized. Pixels with intensity higher than the threshold are represented as white and black otherwise. Figure 3.8(b) shows the binarized output corresponding to the micro-graph shown in Figure 3.8(a).

Removal of secondary α: Both primary and secondary α are part of the white regions in the binarized image. Hence, it is difficult to discriminate them based on intensity and commercial packages fail to do so. But it is important to quantify their volume fraction for better understanding of the material characteristics. In our work, we rely on the geometric features to categorize them. It is observed in Figure 3.7(b) that primary α regions are island like and length of the major and minor axes are close to each other. On the other hand, secondary α components are of elongated nature and length of minor axis is very small in comparison to the major axis. We try to exploit this observation. First of all, morphological opening operation [67] is applied on the binary image to get rid of the small, isolated white regions and also to dissociate the regions touching each other. Size of the structuring element is taken as 5×5. This operation partially removes secondary α regions of very small size. For the removal of the remaining secondary α phase, we consider geometrical features as follows.

1. Disjoint white components are labeled through component labeling [67].
2. For each component C_i

   (a) Compute average length, H_i in horizontal direction
   (b) Compute average length, V_i in vertical direction

3. Compute overall average length in horizontal (vertical) direction, H (V) by taking the average of H_i (V_i).

4. Components C_is with $H_i < H$ or $V_i < V$ are removed.

At first the white components are labeled. It is observed that primary and secondary α regions can be differentiated based on the aspect ratio of the components. Instead of finding the major and minor axes of the components, we have computed their average lengths H_i and V_i in horizontal and vertical direction respectively. To do so line segments within the components are measured at regular interval (in our case, it is taken as 5 pixels apart). Although the components may not be aligned along horizontal or vertical directions, H_i and V_i provide approximate descriptors towards aspect ratio. Secondary α components are likely to have low H_i or V_i. If either of the value is smaller than the corresponding threshold then the component is taken as secondary α. H and V are obtained by averaging H_i and V_i respectively and taken as the thresholds. Result after Removal of secondary α is shown in Figure 3.8(c).

Final segmentation of primary α: Figure 3.8(d) shows the magnified version of a portion of the image shown in Figure 3.8(c). Small black regions are trapped inside the primary α phase. Intensity variation can exist in a micrograph because of various reasons like non-uniform illumination, noise in the image acquisition system. As a result error may creep in affecting the binarized output. Such trapped portions are actually considered as part of α phase and marked as white. Figure 3.8(e) shows the output corresponding to Figure 3.8(d). Figure 3.8(f) is the detected primary α phase (shown in white) corresponding to the image shown in Figure 3.8(a).

Detection of secondary α and β phases

Once the primary α phase is detected, the remaining part is considered as the α/β lamellar mixture (black region in Figure 3.8(f)). This portion is to be classified into secondary α and β. Secondary α is brighter in comparison to β phase regions. Intensity based thresholding can distinguish the two. As secondary α is the outcome of a transformation process, variation in intensity exists. Hence such regions those are detected in the course of extracting the primary α phase may be partial. This consideration forces us to determine the phase in a focused manner. Again a threshold is obtained following Otsu technique from the heat-treated image (Figure 3.8(a) in our example) by excluding the segmented primary α phase. The threshold thus obtained is likely to be liberal to take care of the

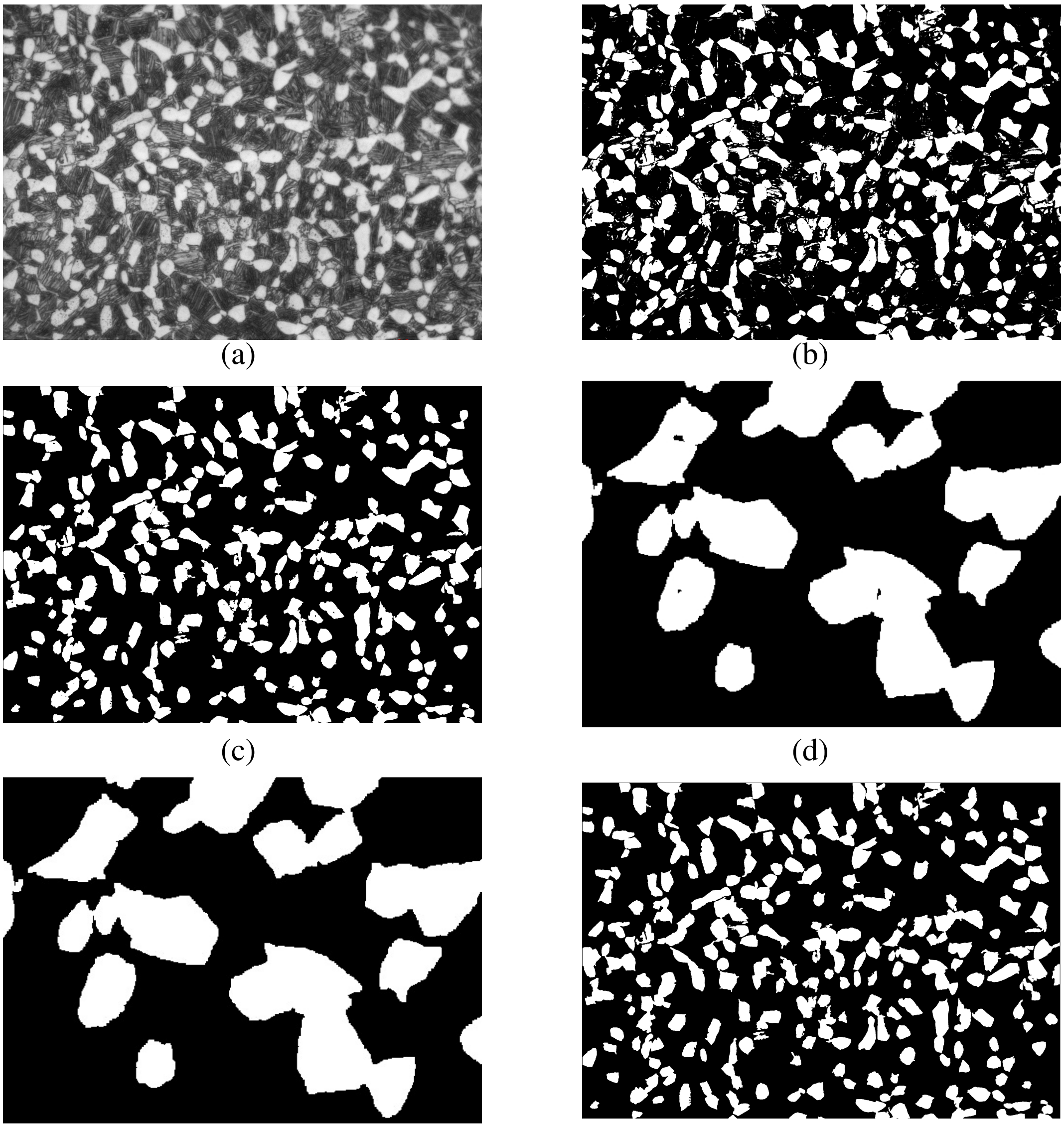

Fig. 3.8 Segmentation of primary α phase: Step-wise output. (a) Sample heat treated microstructure, (b) Output after thresholding, (c) Output after removal of secondary α phase, (d) Partial view (magnified version) of Figure 3.8(c) showing small trapped black region, (e) Final Output corresponding to Figure 3.8(d) after removal of trapped regions and (f) Segmented primary α phase (in white) corresponding to Figure 3.8(a).

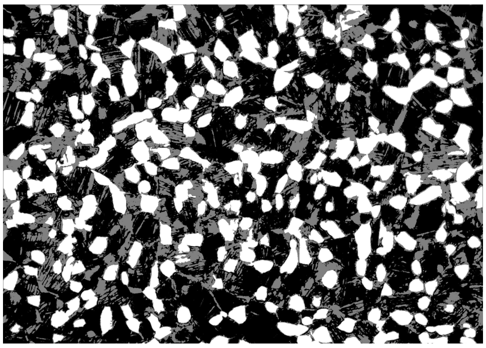

Fig. 3.9 Segmentation output corresponding to Figure 3.8(a): primary α in white, secondary α in gray and β in black.

intensity variation in the secondary α phase. Pixels with intensity higher than the threshold constitute secondary α and rest belongs to β phase. Final output corresponding to Figure 3.8(a) is shown in Figure 3.9 where white, gray and black regions correspond to primary α, secondary α and β phase. Once the segmentation of the phases is achieved, the ratio of the number of pixels in different phases represents their relative volume fraction.

3.4.2 Experimental Result

In our experiment we have used heat treated $Ti-6Al-4V$ alloy. It is an α/β alloy. The heat treatment route consists of heating at 965^{o}C for 1 hour where both α and β phases coexist followed by cooling in still air and aging at 700^{o}C for 2 hours followed by still air cooling. Such heat treatment leads to the development of bi-modal structure. Following heat treatment the specimen was first polished using successively finer grade SiC base emery papers and then cloth polished using an emulsion of Al_2O_3. After complete polishing, the specimens were thoroughly cleaned with water and then with acetone and dried. The cleaned polished surfaces of the specimens were etched with Kroll's reagent (2 vol% HF and 4 vol% HNO_3 in H_2O). The polished and etched surfaces of the specimens were viewed in an upright optical microscope, Leica DM2500. The optical images of the micro-structures were grabbed with the help of a digital camera, Leica interfaced with a personal computer. As many as six different fields of the etched specimen surface were observed and the digital images of the micro-structure was captured and stored in computer for quantitative analysis of phase fractions.

The methodology is applied on each of the six fields of the sample for segmentation and determination of relative volume fraction of the phases. Among these three field of views and corresponding segmentation outputs are shown in Figure 3.10. Volume fraction of the detected phases are listed in Table 3.2. The result conforms the expected characteristics of the titanium alloy.

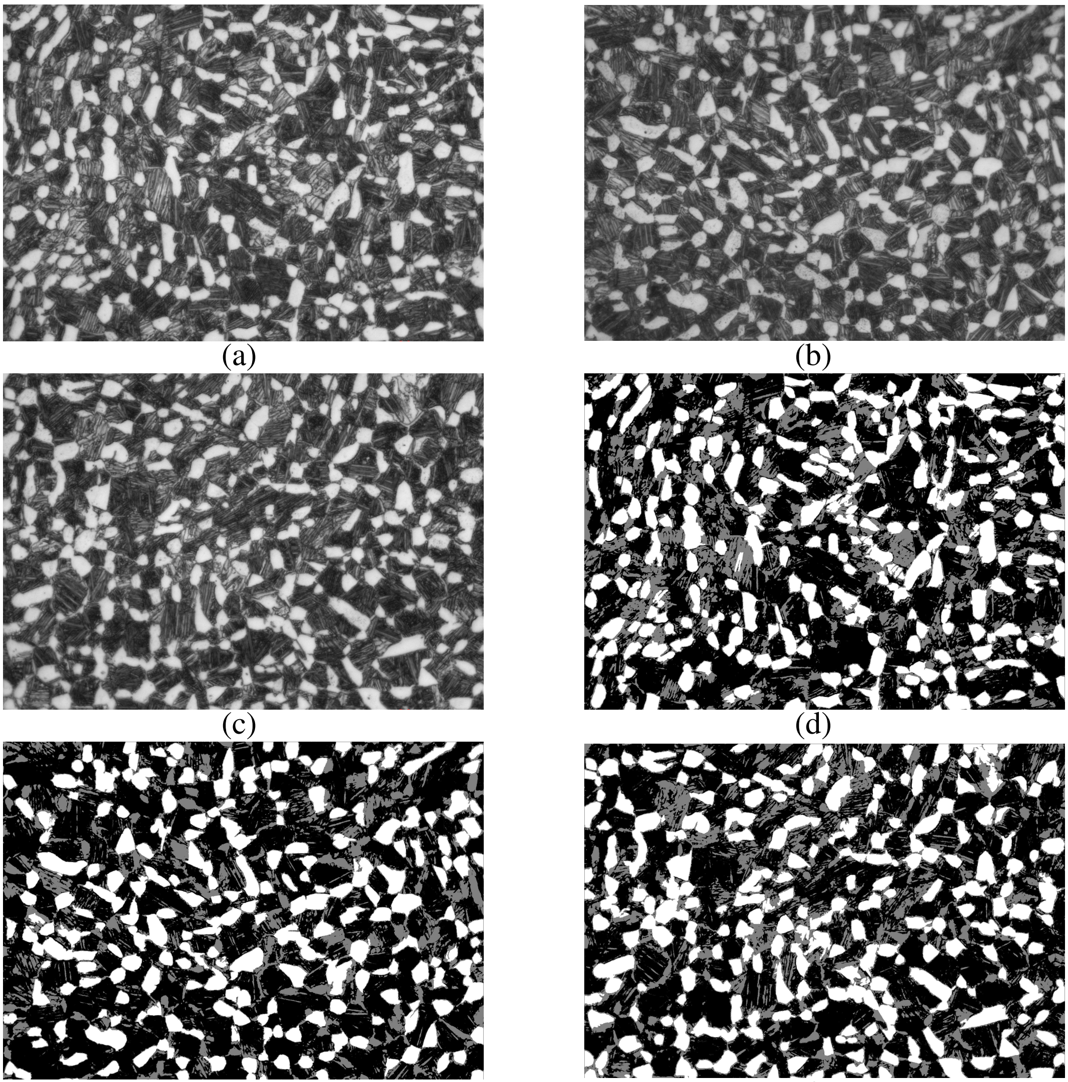

Fig. 3.10 (a)-(c) Micro-structure of different field of views and (d)-(f) corresponding segmentation output (primary α in white, secondary α in gray and β in black).

Table 3.2 Volume fraction of the phases for the six field of views.

		Transformed Phases	
Image	Primary α Phase	Secondary α phase	β phase
Image 1	.50	.25	.25
Image 2	.50	.25	.25
Image 3	.55	.24	.21
Image 4	.51	.26	.23
Image 5	.58	.22	.20
Image 6	.56	.23	.21

3.5 Summary

Novel schemes for automatic extraction of the phases present in the two different types of material namely dual-phase steel and titanium alloy. Number of specimens for each types of material has been developed and proposed methodologies are applied. In both the cases, the limitations of simple threshold based scheme are overcome. Proposed Methodology to work with the specimen of dual-phase steel, can well separate the grain boundary and white (martensite) phase despite of their similarity in terms of intensity value. Moreover, proposed definition of neighbourhood can handle the trapped ferrite and splitted martensite regions. Finally, it generates closed martensite regions. All these have significant impact on the phase volume fraction measurement. To work with the specimen of titanium alloy, along with intensity based thresholding, geometric property is utilized for segmentation.

Chapter 4

Local Strain Analysis

4.1 Introduction

Deformation measurement of materials and structures subjected to various loading conditions (mechanical or thermal) is an important task of experimental solid mechanics. The deformation behaviour of different materials under load that are routinely studied is an average response of the micro-structure of a material. It is by now established and well documented in the literature that plastic deformation in polycrystalline materials is never homogeneous, whether the material consists of a single phase or multiple phases. Orientation difference of individual grain with respect to the loading axis is responsible for grain to grain variation in plastic deformation even when deformation is macroscopically homogeneous [6–8]. Further, deformation heterogeneity also exists within individual grain. Raabe et al. [80] have elaborately discussed the occurrence of deformation heterogeneity within individual grain in coarse grained aluminium specimen. In order to know the influence of different grains and other phases constituting the material's micro-structure, sophisticated experimental and finite element modeling techniques are often used. Nowadays, electron back scatter diffraction technique in conjunction with scanning electron microscopy (SEM) is being exploited to understand the deformation heterogeneity in polycrystalline materials. Deformation experiments directly under SEM also provide scope for studying the deformation response of individual grain under load. In this technique, the grain structure and other constituting phases of the material are directly observed during deformation. It is known that the deformation characteristic of individual grain depends on its crystallographic orientation and also on the orientation of the surrounding grains with respect to loading axis. Collectively, the deformation of individual grain controls the average deformation behaviour of a material. As a result, investigation towards understanding the nature of micro-level deformation has gained impetus over the last few years [9–15]. It is worth mentioning that strain measurements at any point in an area of interest are required for better understanding of the deformation behaviour of materials and structural components. For this reason, researchers are interested on a strain map over a specimen surface. Use of digital image processing techniques has enabled such measurements.

Interstitial free high strength (IFHS) steels of 1 to 2 mm thickness find extensive applications in automotive industries for their very good cold formability and reasonable strength properties. Volumes of work have already been done correlating processing parameters with the development of texture that controls the formability of the steel. Our interest is, however, different, and we focused our attention to develop an automated methodology for knowing the deformation pattern of individual grain when a specimen made of 1 mm thick IFHS steel is subjected to incremental load. The impetus for developing such automated methodology stems from the fact that the commercial DIC software that is used to know the local strain distribution using the images as an input works as a black box. This automated methodology has been developed by employing image analysis procedure on scanning electron micrographs captured during deformation.

4.2 Past Work

Digital image correlation (DIC) is an optical method that uses a mathematical correlation analysis to examine digital image data taken while the specimens are subjected to incremental load. As discussed and reviewed by Pan et al. [81], two-dimensional DIC is a practical and effective tool for quantitative in-plane deformation measurement of a planar surface, and it is widely accepted where contact method of strain measurement is difficult. Measurement of small difference in the images supports such correlation [45]. Electronic speckle photography offers a simple and fast technique for measuring in plane displacement fields in solid and fluid mechanics. An improved algorithm for measuring the correlation between subimages has been presented by Sjodahl [46]. The Vic2D presented by Cintron et al. [47] is an innovative approach that uses the DIC technique for strain measurements in a two-dimensional contour map of planar surfaces. But it cannot provide displacement and strain maps after the specimens show cracks because of poor correlation. The maps obtained from the specimen images that show cracks are not adequate to determine the strain values at some locations inside the area of interest. It is also reported that the DIC technique can also used to determine the heterogeneity and severity of deformation in polycrystals [50]. Besides, in situations where it is difficult to measure the strain directly, this technique finds application in knowing macroscopic strain during creep deformation [51].

A novel microscopic strain mapping technique based on DIC has been developed in recent years for various applications in materials characterization. In these cases, input is a series of SEM images,

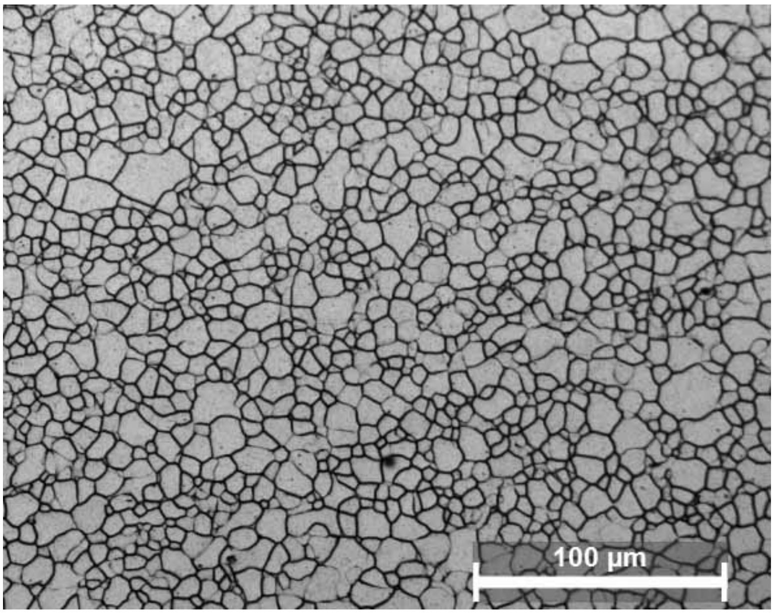

Fig. 4.1 Optical microstructure of investigated IFHS steel.

and strain mapping is done based on the topographic features of the images. For this purpose, many researchers [20, 21] have used commercially available optical strain measurement system (ARAMIS), which utilises the DIC methodology. Cao et al. [48] have proposed a simple and efficient non-contact method to overcome the difficulties of determining Poisson's ratio using traditional contact method. They used DIC method in their work and obtained the relative deformation of specimens using calibrated CCD images.

4.3 Proposed Methodology

The IFHS steel sheet of 1 mm thickness received from TATA Steel, Jamshedpur, India, has been used in the present investigation. The chemistry of the steel in wt. pct is: Fe 0.0029C, 0.39Mn, 0.004Si, 0.007S, 0.05P, 0.005Si, 0.018Cr, 0.044Al, 0.005Cu, 0.001Nb, 0.042Ti, 0.0018N. Optical microscopy reveals that the micro-structure of the steel consists of polyhedral grains of ferrite, as shown in Figure 4.1. The two-dimensional average grain size of the steel is about ASTM 10. Tensile properties of the steel deformed at a strain rate of $10^{-3} sec^{-1}$ are: Y. S = 189 MPa, T. S = 374 MPa, Uniform elongation = 21 pct, Total elongation = 37 pct.

Tensile deformation experiments were also done directly under SEM using miniature sized tensile specimen fabricated by wire electro discharge machining process while keeping the specimen axis parallel to the rolling direction. One surface of the specimen was metallographically polished

Table 4.1 Global stress–strain behaviour corresponding to captured micrographs.

Micrographs	Stress/MPa	Strain measured experimentally/%
Micrograph 1 (Figure 4.2(a))	0	0.00
Micrograph 2 (Figure 4.2(b))	116	1.14
Micrograph 3 (Figure 4.2(c))	174	2.56
Micrograph 4 (Figure 4.2(d))	233	6.00
Micrograph 5 (Figure 4.2(e))	282	8.26

in successive steps, and final polishing has been done using 1 mm diamond paste. The polished specimen has been thoroughly cleaned, dried and then etched with Marshall's reagent in order to reveal the grains lying on the surface. The polished and etched specimen has been deformed under tensile loading at a deformation rate of 1 mm per minute inside the vacuum chamber of an SEM (FEI, Quanta 450). The loading device was screw driven GATAN, UK make tensile/bending deformation stage.

It should be noted here that from a number of trial experiments, we observed that the pin loading arrangement of the tensile deformation stage that we used in the present investigation does not accurately measure the specimen strain because of slackness of the loading arrangement, particularly at the low load level. To overcome this difficulty, we measured the specimen strain between two collinear micro-indentation marks separated by 2000 μm put on the polished and etched specimen surface placed before the deformation experiment. The specimen was then loaded in steps, and high resolution secondary scanning electron images were captured after each step of loading. The strain measured within these two micro-indentation marks is termed here as global strain. Thus, a series of scanning electron micrographs were obtained until complete fracture of the specimen. These images were subsequently processed to find the grain level deformation pattern. Here, the image in the undeformed condition is called as reference image, and image correlations have been done with respect to this undeformed image to find the grain level deformation. Figure 4.2 shows a sequence of secondary scanning electron images corresponding to different load levels. The present study is based on these images. The stress and strain corresponding to the images are shown in Table 4.1.

In general, a micrograph reveals the size, shape and distribution of different constituting phases or grains. During deformation of the specimen, grain shape is changed depending upon its size, crystallographic orientation and load level. Additionally, deformation features, for example, slip lines, also become visible in the high resolution scanning electron micrographs of the deformed specimen. However, crystallographic orientation of the grains with respect to loading axis has not been considered in the present work. The major steps involved in the present study are grain segmentation, tracking the grains in the sequentially captured micrographs and grain level strain measurement. It

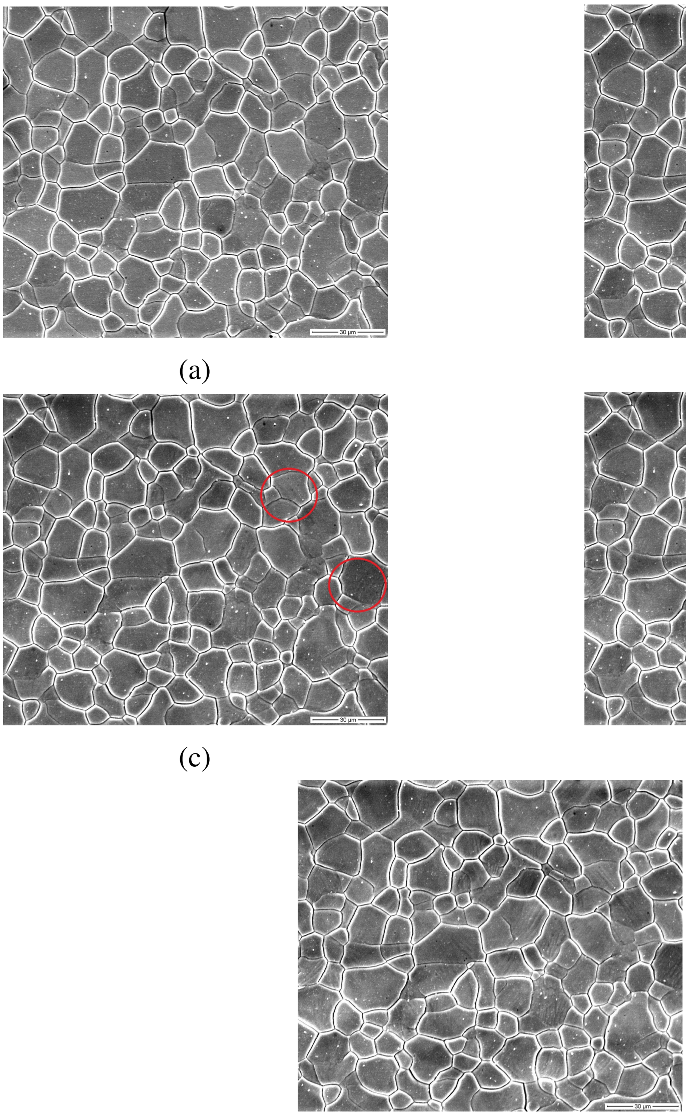

(a) (b) (c) (d) (e)

Fig. 4.2 Sequence of secondary scanning electron images at different loads.

should be noted here that in the present study the estimation of grain level strain has been done only in the loading direction, that is along the tensile axis, which coincides with the horizontal direction of every image frame.

4.3.1 Grain segmentation

Image segmentation refers to the automatic extraction of the regions of interest from the image. Ideally, a region should be homogeneous in terms of a certain property that characterises the region. Identifying such property is an important task in the segmentation process. A closed boundary separates the segmented region from the rest. One common approach of segmentation is to detect the boundary. Since our aim is to develop an automated process for studying the grain level strain distribution, it becomes necessary to extract the individual grain present in a micrograph.

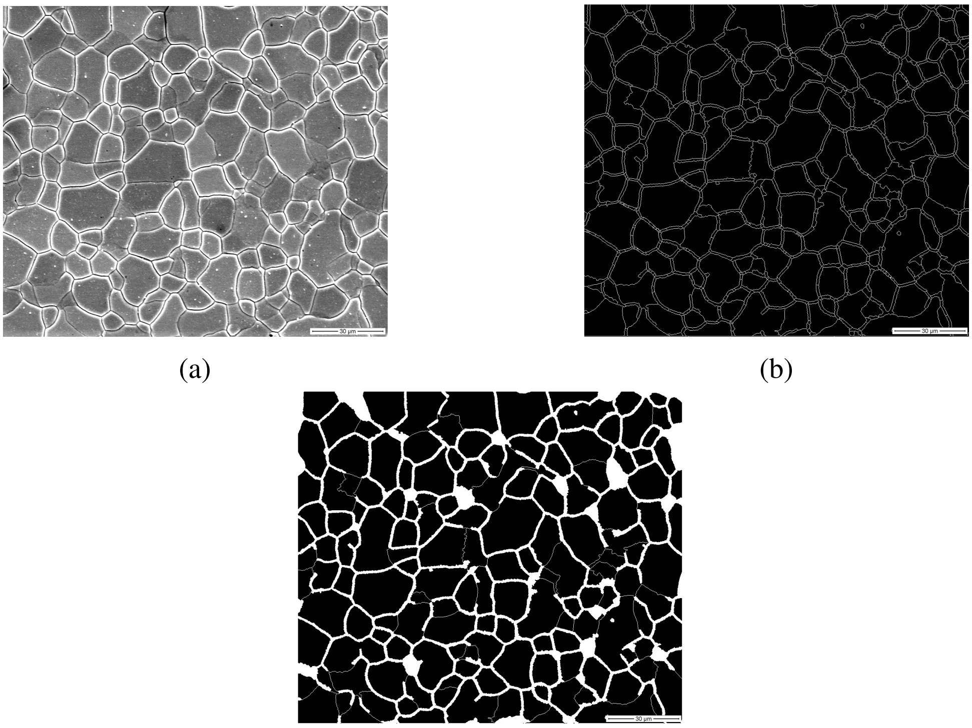
(a) (b)

(c)

Fig. 4.3 Grain segmentation: (a) A sample micrograph, (b) Output of Watershed algorithm and (c) Final output after refinement.

A sample micrograph composed of a number of grains is shown in Figure 4.3(a). It is observed that a grain is normally enclosed within a boundary that separates it from the adjoining grains. It is also observed that mostly the grains consist of pixels with low intensity values. On the contrary, the boundary pixels are of high intensity values. Our motivation is to detect the closed (without any break/discontinuity) boundary encompassing a grain. However, a simple intensity based threshold technique does not always serve the purpose. There may be weak boundaries with not so high intensity value. Again, different grains may have different intensity levels even though a grain is more or less uniform in terms intensity. Thus, it is possible to have an overlap between the intensity values of the pixels inside the grains and those in the boundaries. As a result, some pixels in the grain may be incorrectly marked as boundary. On the other hand, part of the boundary (weak portions) may be missed out and will give rise to discontinuity. Thus, obtaining the desired closed contours that enclose the grain is a major challenge. Furthermore, the selection of proper intensity value as the threshold is also very difficult. Therefore, a suitable property of the image other than the intensity value is to be explored for segmentation purpose. Careful observation of the micrographs reveals that contrast can act as a suitable property in the segmentation problem under consideration. Contrast stands for the difference in intensity values between two regions in the image. The grain boundary in the micrograph becomes visible provided there is a perceivable change in contrast between the boundary and the grain interior. With these observations, we look forward to adopt a suitable scheme that generates a closed contour/boundary of the grains.

Determination of grain contours

Active contour models and its variants [82, 83] are widely used to determine the closed contour of the objects present in an image. For this purpose, an initial guess of the object contour is required. The final contour is then evolved through minimization of an energy function. The energy function is defined based on the image feature (*e.g.*, intensity gradient). It has an external energy component that guides the contour towards the object boundary, and the internal energy component resists the deformation of the contour. The major drawback of the active contour model is that it requires an initial guess for the contour of each object, and it fails for the touching objects. In our context, the micrograph consists of multiple grains. It is prohibitive for the user to provide the initial guess for the contour of each grain. Moreover, one grain touches another. Hence, the active contour model does not satisfy our requirement.

Watershed transform based algorithms [27, 84, 85] are also commonly used in image segmentation, and they also provide a closed contour of the objects present in the image. The concept of watershed was introduced in 1970s. Since then, many improvements have been made on it. In this approach, a gray scale image is considered as a topographic relief where intensity value is thought of as the altitude in the relief. The intuitive idea is to classify the landscape regions as catchment basins and watershed lines. Catchment basins are low altitude regions in the landscape that holds water, and watershed lines (as if, mountains) are of high altitude acting as the barrier between the basins. In a gray scale image, a dark/ low intensity area corresponds to basin, and watershed lines are light/high intensity area. A drop of water falling on a topographic relief flows along a path and finally reaches local minima. Intuitively, the watershed of a relief corresponds to the limits of the adjacent catchment basins of the drops of water. The algorithm identifies the basins and the watershed lines separating the basins. In the context of our problem, the grains correspond to the basin, whereas the grain boundaries are the watershed lines.

Watershed based segmentation algorithms can be classified into two major categories. One category focuses on detecting the basins, and the other focuses on finding the watershed lines. Flooding [27, 84] belongs to the first category. Such schemes have a tendency of over segmenting the regions. In a micrograph, the intensity values within and across the grains (basins) vary, and flooding is likely to split a grain into multiple regions. Moreover, a flooding based approach does not preserve the contrast. A topological watershed [85] is directed towards the generation of watershed lines. A graph based implementation is provided in the work of Couprie et al. [85] and the mathematical foundation of the work has also been established [86]. A topological watershed algorithm works with the gradient image. Thereby, instead of absolute intensity value, it relies on the local contrast. It focuses on the detection of the contour separating the adjacent basins. The detection uses a parameter (t) that specifies the minimal altitude separating the catchment basins. Physically, t can be interpreted as the contrast between the grain interior and the grain boundary. Topological watershed preserves contrast and provides closed contour of the grains as desired in our study.

Applying the topological watershed algorithm, the closed contours of the regions are obtained. The value of the parameter t needs to be chosen carefully. A low value of t over splits a region as it becomes sensitive to smaller intensity variation. On the other hand, a high value of t will accommodate more variation within a region and overlook weak boundaries. In our experiment, a moderate value for t is estimated, which approximates the contrast between the grain region pixels (low intensity value) and boundary pixels (high intensity value), and t has been taken as $2 \times \sigma$, where σ is the standard deviation of the intensity values present in the image. The extracted contour for the grains shown in Figure 4.3(a) has been presented in Figure 4.3(b), where the white lines are the contour lines.

Refinement of contour

The grain boundaries detected by the watershed algorithm are shown in white in Figure 4.3(b). However, all the enclosed regions shown in black are not grains. It is observed in Figure 4.3(a) that the grain boundaries are quite thick because of the deep etching used to reveal them. As a result, the watershed algorithm detects the contrast difference around both inner and outer contours of the white thick boundaries. Finally, all the edges of the thick boundaries are extracted as watershed lines. The small patches enclosed between such lines are also identified as basins (grains). Thus, refinement is required to get rid of such regions that are actually part of the boundary. It is achieved by removing the black regions that are of very small area by applying morphological closing operation [67]. It may be noted that in this process very small grains may be missed out. Figure 4.3(c) shows the final output of segmentation obtained after applying the refinement process on Figure 4.3(b). The black region enclosed within the white boundary corresponds to a grain.

4.3.2 Tracking of grains

Once the grains are segmented, each of them has to be uniquely marked in every sequential micrograph. Given the sequence of micrograph, correspondence between the grains also has to be established to enable the measurement of strain at grain level. It involves two steps:

1. Component labelling.
2. Finding grain correspondence across the micrographs.

In the segmented output, black pixels are part of the grain. Component labelling [67, 66] starts with a black pixel and marks it with a label. It also marks the black pixels in its four-neighbourhood with the same label. The process goes on recursively with newly marked pixels. It stops when no further growth is possible. Thus, all the pixels in a particular grain are marked with the same label. The process then continues starting from another unmarked black pixel with a new label. Thus, when no unmarked black pixel is available, all the grains in the micrograph are uniquely labelled.

Pixels with same label belong to same grain. Because of the deformation, grains may undergo changes in terms of their size, shape, displacement and physical orientation. Thus, corresponding grains in two consecutive micrographs may not bear the same label. Therefore, it is not possible to link them based on the assigned labels. In this work, we establish the correspondence based on the proximity of the centroid (CG) of the grains in the consecutive micrographs in the sequence. The CG of a grain is computed based on the spatial moments [67]. The moment of order (p,q) of a grain can be defined by

$$m(p,q) = \sum_{c}\sum_{r} r^p c^q f(r,c) \tag{4.1}$$

where $f(r,c)$ is the intensity of the grain pixel at (r,c), r and c spread over the grain. $m(0,1)$ and $m(1,0)$ are the first order moments. $m(0,0)$ is known as the mass of the object. The coordinate of the CG is computed as follows

$$\left(\frac{m(1,0)}{m(0,0)}, \frac{m(0,1)}{m(0,0)}\right) \tag{4.2}$$

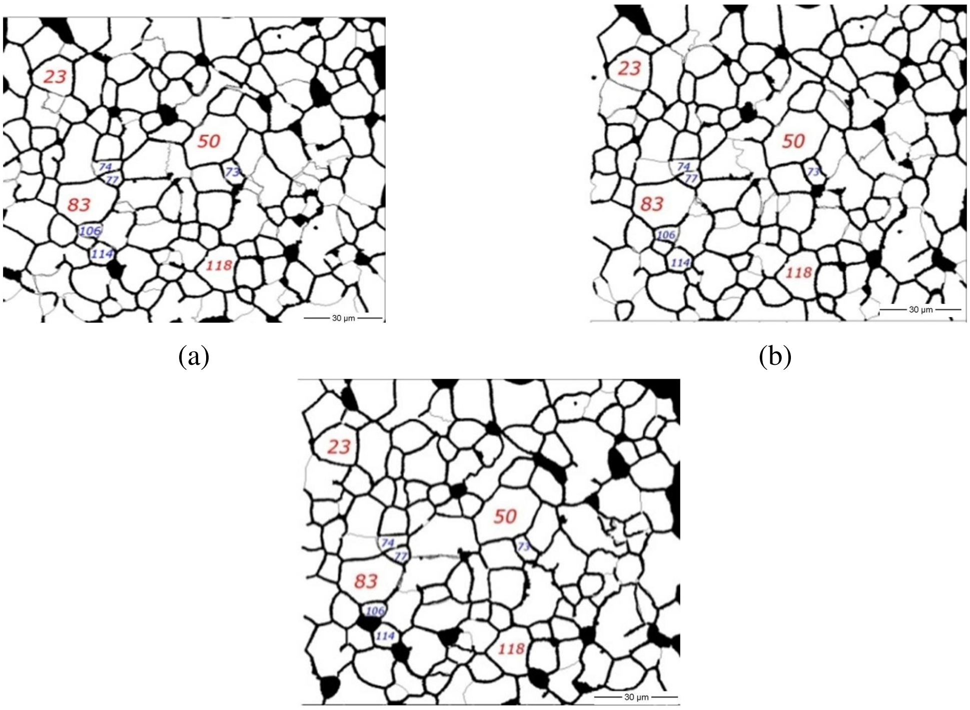

(a) (b)

(c)

Fig. 4.4 Tracked grains in sequence of micrographs: (a) A reference micrograph, (b) and (c) Corresponding micrographs under deformed condition.

The *CG*s of the grains are computed in each micrograph. Let (r_{ij}, c_{ij}) denote the CG of a grain g_j in the i-th micrograph. Corresponding to (r_{ij}, c_{ij}), the nearest CG is searched in the $(i+1)$-th micrograph. Suppose the nearest one corresponds to the grain g_k in the $(i+1)$-th micrograph. Then, g_i is tracked as g_k in the next micrograph. The process continues over the pairs of successive micrographs, and thereby, the grains are linked. Figure 4.4 shows the tracking of a few marked grains.

4.3.3 Strain measurement: DIC based technique

For measuring the grain level strain, the intensity values of each micrograph are first normalised. It reduces the impact of contrast/brightness variation (if any) during the capturing of different images. After tracking the individual grain of interest in the series of micrograph, a two-dimensional grid is drawn on that grain for correlation among consecutive images. In this technique, physical grids are not laid on the specimen surface as practised by lithography [16–19]. But in this experiment, an imaginary grid is placed on the reference image. It has been done in a manner so that the grid covers the grains over the area of interest on the specimen surface (Figure 4.5(a)). The corresponding grid patterns on subsequent images of the deformed specimen are generated by the correlation technique, as shown in Figure 4.5(b)-(e).

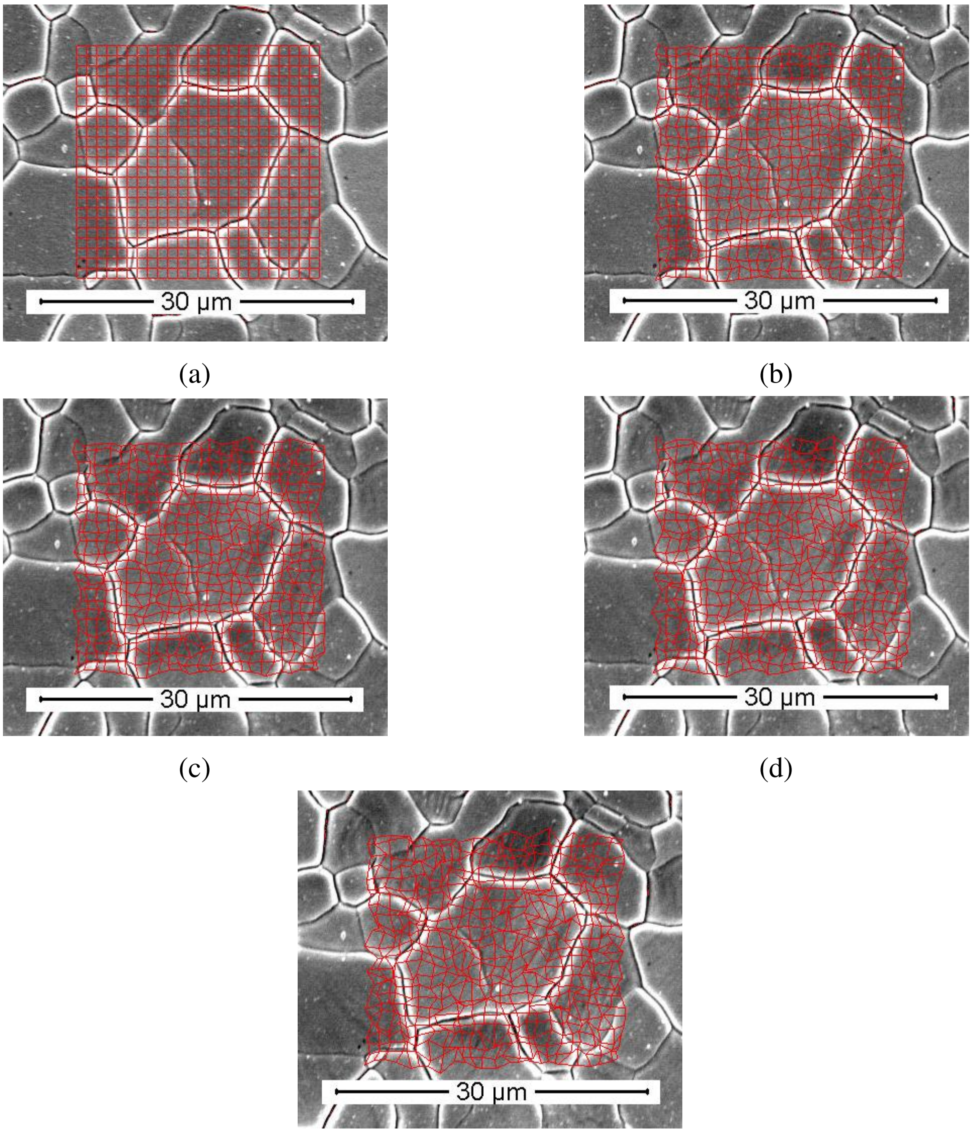

(a) (b)

(c) (d)

(e)

Fig. 4.5 (a) Grid drawn on portion of reference micrograph and (b)–(e) Grid drawn by DIC technique on corresponding portion of subsequent micrographs.

Correlation among the consecutive micrographs has been established using intensity based similarity. The schematic diagram of image correlation process is shown in Figure 4.6. An imaginary grid is placed on the reference image. Figure 4.6(a) shows such horizontal and vertical grid lines in red colour, and the black squares represent the image pixels. Red squares formed by the intersecting grid lines are referred as subgrids. Each subgrid covers a small region of an image (10×10 pixels in our case). Let S_r denotes the set of intersection points of the vertical and horizontal grid lines (i.e. corner pixel of the subgrids) in the reference image. Corresponding to each element in S_r, the corresponding pixel in the next image is determined using intensity based correlation. Let p be an element in S_r with coordinates (X_p, Y_p). There may be a number of pixels in the next image with intensity similar to that of p. To surmount this problem, block matching is considered instead of individual pixel intensity based matching. This is similar to the commonly used approach in estimating the motion in video.

As shown in Figure 4.6(a), a block Br (in blue) centred at p is taken. In our case, the size of the block is 3×3 pixels, and it comprises of the pixel p along with its 8-neighbours. To search the best match for Br, a search window (SW) is considered in the next image. The search window is of size $K \times K$ (must be larger than the block size), and it is centred at (X_p, Y_p), as shown in green in Figure 4.6(b). In our experiment, K is taken as 11. The best match for Br is exhaustively searched in SW. A few cases are shown in Figure 4.6(c) and (d). Br and a block in SW are compared based on the sum of absolute difference (SAD) of the intensity values of corresponding pixels in the blocks. The block in SW with minimum SAD is the adjudged as the match for Br. The centre pixel of the matched block in SW is taken as the correlated pixel for p. Thus, for each pixel in S_r, a set of correlated points (S_c) in the next image is obtained. Figure 4.6(e) shows four corner points of a subgrid of reference image in red, and correlated points are in yellow. Correlated points corresponding to each side of the reference subgrid are joined by straight lines, and a deformed subgrid (shown in yellow) is obtained. To continue the correlation process for the subsequent images, S_c obtained in the previous step is taken as S_r for the next image, and the same process is followed.

To measure the grain level strain at a load, we restrict ourselves within the part of the grid covering the grain of interest. Let the rectangular bounding box with upper left corner (X_l, Y_l) and bottom right corner (X_r, Y_r) enclose the grain in the reference micrograph. After deformation, the bounding box may vary. To accommodate such variation, the rectangular region of the grid with upper left corner $(X_l - 20, Y_l - 20)$ and bottom right corner $(X_r + 20, Y_r + 20)$ in the reference micrograph is considered. Furthermore, the subgrids lying in the grain interior are taken into consideration for strain measurement.

Let the length of a side of the subgrids in the reference micrograph be l_0, and l be the length of the corresponding side on the micrograph of subsequent image in the loading direction. Then, the strain is calculated as $[(l - l_0)/l_0]$. The average strain of the grain is determined by averaging the strain of all such sides that are inside the grain. It should be noted here that the deformation of all the subgrids does not always follow the same direction as that of the applied load. As a result, in presence of tensile load, negative deformation of the subgrids frequently occurs. However, the overall deformation of individual grain consisting of subgrids has been found positive.

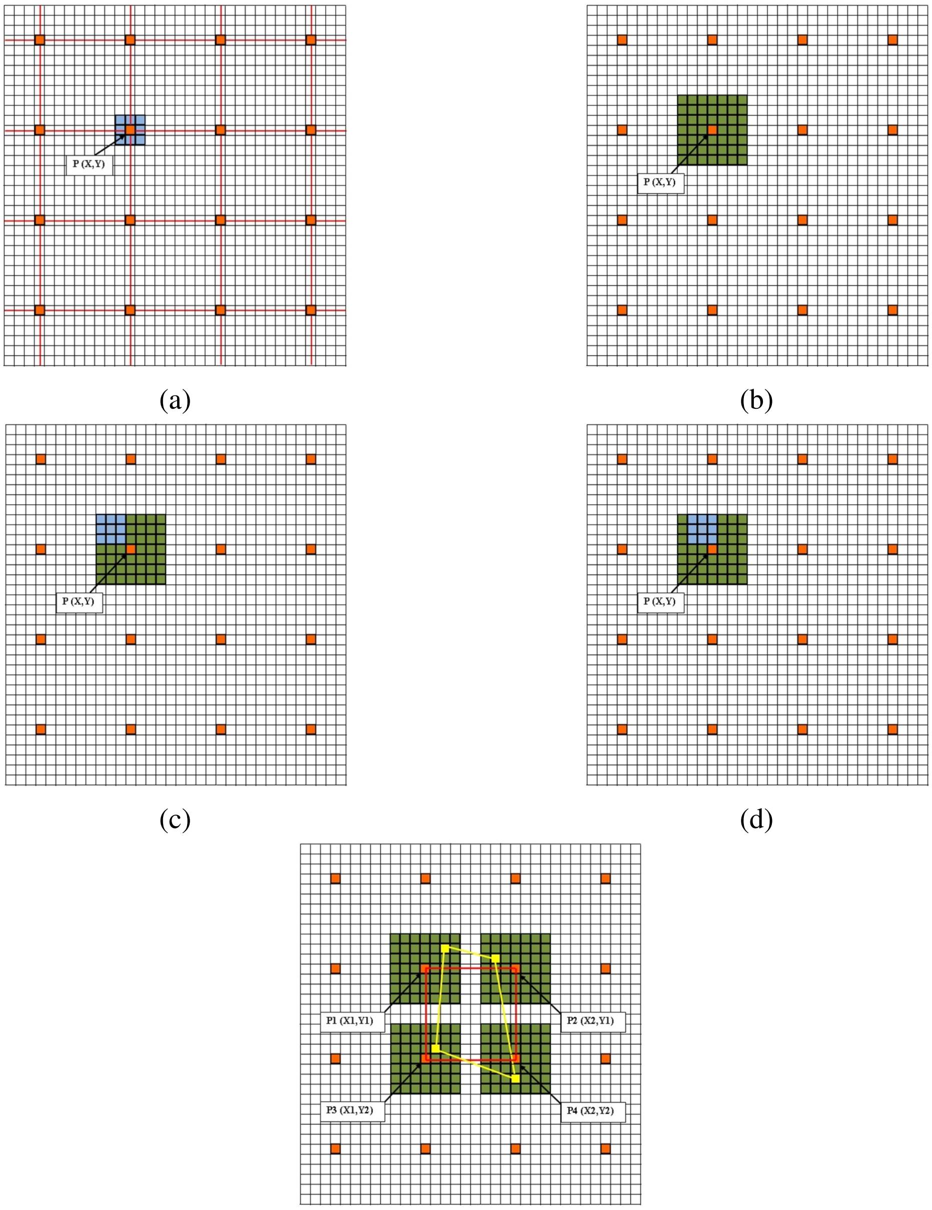

(a) (b) (c) (d) (e)

Fig. 4.6 Schematic diagram for DIC: (a) imaginary grid and block of 8-neighbour pixels (in blue) corresponding to P(X, Y), subgrid corner in reference image, (b) search window (in green) for P(X,Y) in image following reference image, (c) and (d) search process to find match for block around P(X,Y) in search window and (e) subgrid of reference window (in red) and corresponding deformed subgrid (in yellow) superimposed on reference image.

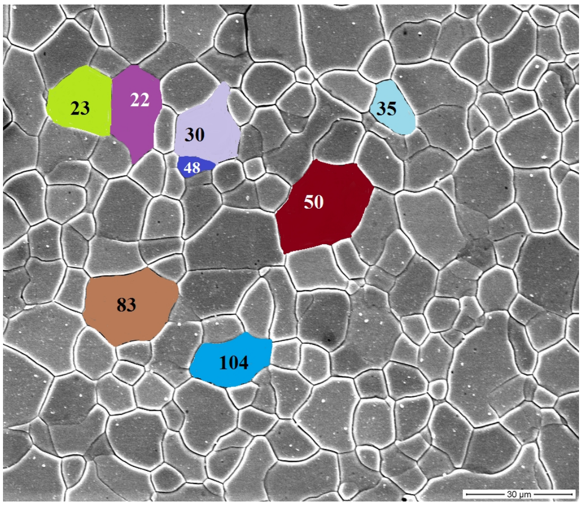

Fig. 4.7 Marked grains in reference image.

4.4 Experimental Result

Few grains over which the experiment has been carried out are marked in the reference image and shown in Figure 4.7. The average strains for these grains on varying stress are shown in Figure 4.8. The detailed strain distribution over the marked grains is also studied. Figure 4.9 shows the strain distribution over the grain marked 50, as an example, for different load values. The figure also shows the global strain of the particular grain at different loads. Note that the x axis represents the subgrids in the grain in raster scan order.

It is known that plastic deformation of metals and alloys occurs through movement of dislocations on slip planes. This mechanism of plastic deformation is known as slip. Although each grain of a polycrystalline material is in itself a single crystal, the orientation difference of the grains with respect to the loading axis does not permit all the grains to deform to the same extent. In the present study, it is observed that the slip lines (identified by red circle in Figure 4.2(c)) become visible only when stress exceeds 174 MPa. The corresponding global strain at this load level is 2.56 pct. The slip lines are oriented at 45^o to the loading axis, which coincides with the horizontal direction of the micrographs. It should be noted that using standard tensile specimen, the experimentally determined tensile yield strength of the steel is found as 189 MPa. The difference of 15 MPa between the measured yield strength and the stress corresponding to the first visible slip lines in some grains arises from the differences in tensile deformation behaviour between macroscale and microscale (grain scale). With further increase of load, the slip lines become prominent and found in many grains as expected. All these observations point to the fact that all the grains do not deform to the same extent and at the same instant. The reason behind such grain to grain variation in strain arises because of the orientation difference of the grains with respect to the loading axis [87].

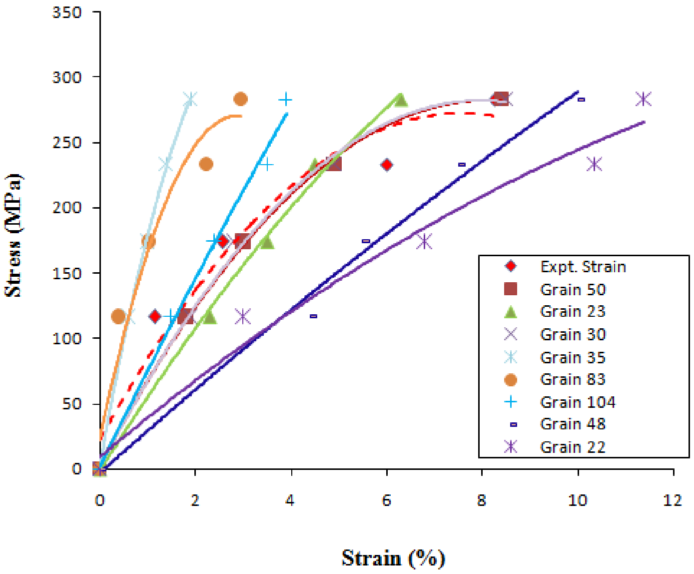

Fig. 4.8 Stress-strain behaviour of different grains obtained using DIC method; macroscopic behaviour is shown in dashed line.

To verify the above conclusion, a methodology has been developed based on the DIC technique to estimate the local strain. It is found that all the grains do not deform to the same extent, but the extent of average deformation of any grain increases with the increase of load. Similar heterogeneous deformation in tensile deformed 1 mm thick commercial interstitial free steel has also been reported by Ghadbeigi et al. [49]. In order to find the grain level strain, we have selected the grains quite arbitrarily and run our program. It is observed that all the selected grains do not deform plastically within the experimental domain, and these grains are termed as hard grains; hard in the sense of their orientation with respect to the loading axis. In the present investigation, it is observed that one or two grains out of eight different grains studied follow the global deformation pattern. Ghadbeigi et al. [49] also reported a similar observation in interstitial free steel, even for very large global deformation.

The methodology that has been developed and followed for measuring grain level strain also brings out that even within a grain there is substantial point to point variation of deformation. This variation also exists in those grains that closely follow the global specimen deformation. The point to point variation of strain within a grain leads to infer that the very local activation of slip systems even within a grain is different. However, detail characterization of the activation of slip systems in individual grains using electron back scatter diffraction technique is necessary to support this inference. Qualitatively, it is also found that the density of slip lines is less in those grains that are comparatively smaller in size. This observation is well connected with the well known Hall–Petch relationship. According to the Hall–Petch relationship, plastic deformation becomes difficult with lowering of grain size. It means that with lowering of grain size, the onset of plastic deformation

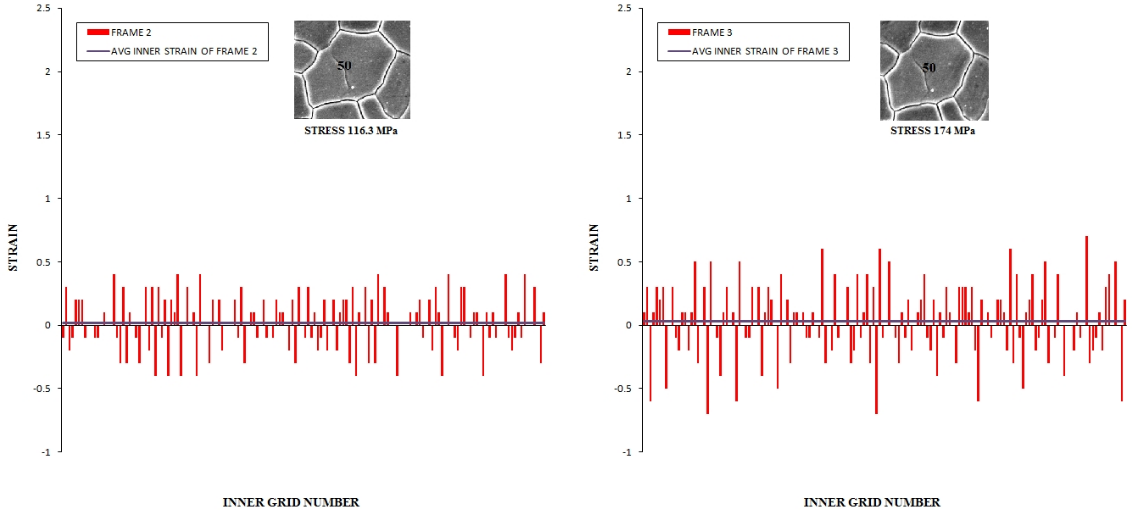

(a) Micrograph 2 (b) Micrograph 3

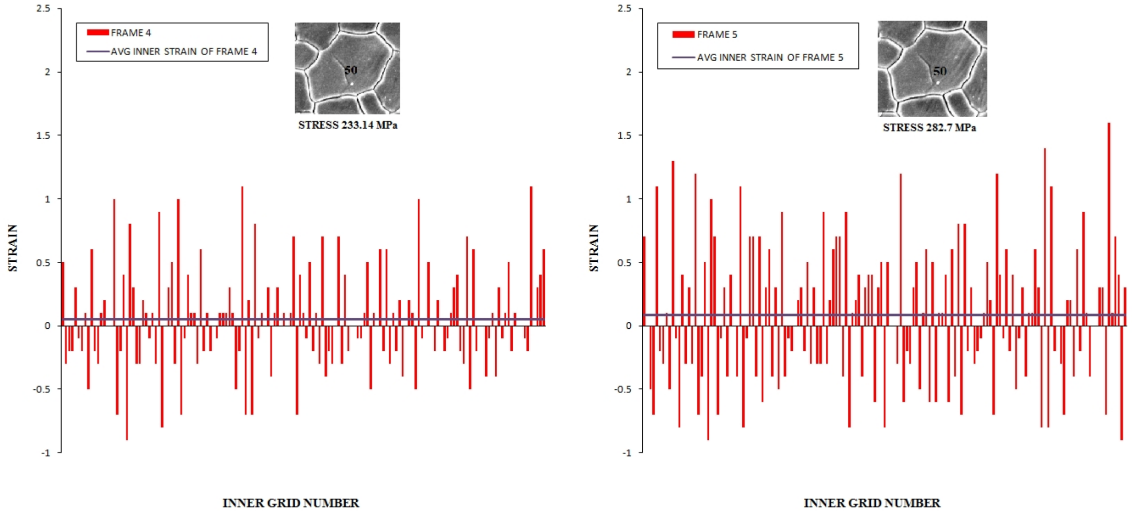

(c) Micrograph 4 (d) Micrograph 5

Fig. 4.9 Strain distribution of individual subgrid over grain 50.

occurs at higher load. It should be noted that the present methodology to find the grain level strain fails at large global deformation. This happens because of the undulation of the specimen surface due to out of the plane movement of the grains.

The DIC methodology developed and used in the present study for measuring local strain is, however, not free from error. The sources for error are (i) the difficulties associated with correlating the subgrid corners in deformed images and (ii) drifting of electron beam in SEM. The difficulty of correlating the subgrid corners also arises with change of contrast and brightness of the images of deformed specimens. To minimize the corresponding error, normalization of intensity values in all images has been done at the very beginning. Besides, to correlate the subgrid corners instead of point matching, a block based matching has been adopted. The best match for the block of size 3×3 centred at the subgrid corners (say, coordinate (x, y)) has been searched in a bigger search window of size 11×11 centred at (x, y) in the next image. The concept of block has been used so that it captures the neighbourhood of the particular point. Such procedure minimizes the possibility of mistracking of the subgrid corners. Tracking of the grains over the series of micrographs and matching the blocks in a bigger search window minimize the error introduced by drifting of electron beam.

In our study, we have estimated the error over a number of reference images, that is, of undeformed specimen, captured at different time intervals, which is about 5 minutes. Hence, the effect due to drifting of electron beam remains in the captured images. Additionally, to find the effect of brightness/contrast on the correlation process, the images of specimens were captured at different brightness/contrast levels. Based on the proposed image correlation technique, it has been found that the error associated with the tracked grains lies within the range of 0.1 to 0.6 %. The error range takes account of all sources of error.

Implementation of our methodology on images of tensile deformed IFHS steel shows that for a global strain of 8.26 pct, the average strains of the marked grains (Figure 4.7) are different. As an example, while for grain no. 35, the average strain is 1.9 pct, and it is 11.37 pct for grain no. 22. As already mentioned, such a large variation in the average strain at the grain level arises due to orientation difference of the grains with respect to the loading axis. In our study, we also found grain to grain variation in the maximum local strain value in the loading direction. In conformity with the observation of Ghadbeigi et al. [49] in our study, it is also found that local maximum tensile strain varies across the grains. For example, while the local maximum tensile strain is 180 pct in grain no. 83, it is 70 pct in grain no. 48.

4.5 Summary

From the results and discussion presented above, it is concluded that tensile deformation of the investigated IFHS steel occurs heterogeneously. The heterogeneity of deformation not only exists among different grains but also within a grain itself. The DIC methodology developed to segment and track the grains considerably reduced the error in measuring the grain level average strain and also the local strain within a grain varying between 0.1 and 0.6 pct. This error value also takes into account the error due to contrast/brightness of the images. The present methodology is capable to segment and track all the grains without any intervention of the user. Finally, the technique developed measures the average strain and local strain of each grain. However, it is necessary to incorporate electron back scattering diffraction characterization of the specimen in the undeformed and deformed conditions at the individual grain level so to correlate the slip system activation of the individual grain with the measured strain. The beauty of the present methodology is that it uses artificial grids over the images and does not require any other sophisticated experimental technique to lay the grids on the specimen surface itself. The present methodology reveals that deformation is heterogeneous, and for an applied global strain of 8.26 pct locally within the grain interior, strain is magnified by many times reaching as high as 150 percent. Further, this local magnification of strain increases with the increase of global strain.

Chapter 5

Fracture Surface Analysis

5.1 Introduction

Failure of engineering components during operational lifetime is an important issue. Some of the common types of failure are: overload failure, torsional failure, impact, fatigue, creep and corrosion related failure. The root cause(s) of failure are investigated by examining the fracture surfaces of failed components. When engineering structure/component fails, it leaves certain signatures on the fracture surfaces. The study of these signatures with the aid of Scanning Electron Microscope (SEM) provides valuable information to - (a) understand the failure process *i.e.* crack initiation and propagation directions; (b) prevailing loading conditions at the time of failure; and (c) underpin the causes of failure etc.

Broadly, failure of components or laboratory specimens is classified as ductile failure and brittle failure. Depending upon deformation characteristics of a material ductile failure is known to occur by void nucleation, void growth and void coalescence leading to the formation of a crack which finally propagates to failure [88, 52, 89]. The dimples observed in fractographs which are the high resolution SEM images of fracture surface are essentially related with the halves of such voids on fracture surfaces. Because a pure dimple structure is a trans-granular mode of ductile fracture, it is indicative of acceptable bulk material properties. It is well established that by delaying or suppressing the void nucleation processes there would be an increase in tensile ductility. For ductile materials, the engineering properties are determined by the interaction of stress and strain fields with the microstructure of a material. The contribution of deformation processes in the development of voids is well established. While void growth mechanisms depends on temperature [90] the nucleation voids result from non homogeneous deformation on a micro-scale. There have been many investigations to understand the void nucleation mechanisms in different materials and ultimate fracture originating from these voids. It is thus expected that fractographic features extracted by post-mortem analysis of fracture surfaces bear certain relationships with mechanical properties of materials. This, however, requires very careful analysis of the fractographic features.

Quantitative fractography is an analytical tool that provides true estimates of the feature characteristics and topography of fracture surfaces. Image processing techniques are being used for fractographic image analysis to correlate mechanical properties of materials [91, 53, 22, 54, 56]. However, the methodologies are not well reported. Generally the image processing tools offer support for fundamental image processing or image analysis operations. Mostly, researchers apply sequences of operations as per their requirement. Such tool based solutions are not general in nature. Moreover, devising such a solution also demands the understanding of image processing. Thus, the outcome depends on the ability of the individual. It, therefore, necessitates the development of an automated system to study the fracture surface characteristics.

5.2 Past Work

Bandstra et al. [52] employed micro-mechanical modeling using finite element analysis to examine the deformation behavior of micro-structures of HY-100 steel. Image-based multi-hole models have been utilized to identify the significance of the critical features (like size, spacing and clustering) of the void micro-structure on the deformation process, void coalescence and failure. The results also show that at high stress deformation develops more rapidly.

Deformation and fracture in steel at room temperature are investigated by Benzerga et al. [91]. Tension and compression tests are used for this purpose. Experiments are carried out to characterize the deformation behavior, and finding out stress state and specimen orientation effects on fracture. The micro-structure is characterized to get initial average values of porosity, void aspect ratio and void spacing ratio since these three playing central role in the fracture process.

Chae et al. [53] characterized damage accumulation in the form of the volume fractions and void number densities for HSLA-100 steel. The experiment reveals that the dependence of void volume fraction on strain is due to the presence of a void growth stage. Void growth stage is sensitive to stress-state that follows a relationship predicted by Rice and Tracey.

Salemi et al. [92] in their study focus on the mechanical properties and the fracture morphology of a NiCrMoV steel. The results of tensile testing indicate that the yield strength (YS) and ultimate tensile strength (UTS) are decreased with increasing tempering temperature but the ductility is increased. However, UTS decreased at a higher rate than YS.

Ductile fracture behaviour of 304LN stainless steel at various strain rates has been studied by Das et al. [22]. Void morphologies (*i.e.* void size, void density and void size distribution) are examined on the tensile fracture surface. An image-processing technique has been employed to quantify the metrices. It has been observed that, the void number density and the strength was higher at lower strain rate but the average circular diameter of void and the ductility was lower. High strain rates show a reverse correlation between void features and mechanical properties.

The deformation behavior of copper strengthened High Strength Low Alloy (HSLA) 100 steel has been investigated by Das at al. [54]. In the experiment, change in coherency, size, shape, and distribution of the copper precipitates has been introduced by various aging treatments. Two-dimensional dimple morphologies are quantified from tensile fracture surfaces. Deformation parameters are correlated with aging treatment.

Venkataswamy [93] used Scanning Electron Microscope (SEM) to study the signatures left on the fracture surface. The experiment shows that signature provides valuable information to (a) understand the failure process *i.e.* crack initiation and propagation directions, (b) existence of loading conditions at the time of failure (c) strengthen the causes of failure etc.

CFRP (Carbon Fiber Reinforced Polymer) materials show high roughness due to the fracture mode known as pulling out. The fractographic analysis using bi-dimensional images is inefficient due to the fact that it not consider the so important vertical resolution as much as the horizontal resolution. Knowledge of this heights distribution may allows a better insight on the fracture mechanisms of the composite material. Surface with high roughness due to the variation in height, should be reconstructed three-dimensionally. Lobo et al. [94] use 3D reconstruction in two different ways. The variable focus reconstruction was done through a stack of images obtained by optical microscopy (OM) and the parallax reconstruction is carried by scanning electron microscopy (SEM) images.

The micro-structural characterization of GG20 and GG25 gray cast iron materials and their fracture behavior was examined by Taslicukur et al. [55]. At first stage, the presence of ferrite/pearlite phases along with morphology and distribution of graphite were determined using light microscope and scanning electron microscope. Leica QWin software package was used to determine the amount of graphite by means of image analysis. In the second stage, mechanical properties were determined using micro-hardness measurements, tensile tests and Charpy impact tests. Fractographic analysis was carried out in the third stage to establish the relationship among phase, loading type and test temperature of the fracture surface.

The micro-structural and fractographic analysis of damage in carbon/epoxy is carried out by Bienias et al. [95] after static and fatigue strength (shear) tests at elevated temperature. The complexity of degradation process and degradation mechanisms in composite structure is confirmed by fractographic analysis and micro-structural test.

Khokhlov et al. [96] describes a new multi-scale stereo-photogrammetry system for inspection of fracture surfaces based on SEM images. A new method has been proposed for geometric reconstruction of a 3D textured mesh from SEM stereo images.

Dutta et al. [97, 56] present texture analyses methods for fractal analysis. Micrographs and fractographs of Cu-strengthened High Strength Low Alloy (HSLA) steel are automatically characterized by Box-counting, grey level co-occurrence matrix (GLCM) technique and run length statistical (RLS) analysis technique. The results show that there is a systematic correlation of the mechanical properties and image texture features with ageing temperatures. In another work, Dutta et al. [98] followed thresholding and texture based methodology for void detection and analysis. Deep learning have also been tried [99].

All the studies cited above shows a strong correlation between mechanical properties and fracture surface morphology. There is no commercially available software for this purpose. Some researchers applied image processing tools but the application generally depends on the visual criterion of the analyst. This initiates the development of an automated approach for void analysis.

5.3 Proposed Methodology

The morphology of the fracture surface depends on different factors *e.g.* service condition, micro-structure of material. Service condition includes parameters like temperature, loading rate, and types of loading. Besides the stress, state of components or specimens also has great influence on fracture morphology. It is well known that ductile fracture occurs due to the formation of voids, their growth and coalescence forming a microcrack. Quantitative estimation like average circular diameter of voids; void density on the fracture surface *etc.* are very significant in understanding the mechanical properties of materials undergoing ductile fracture. For such quantitative analysis detection of void regions is the most important task.

The present work deals with complete dimple fracture surface which develops from full grown voids of different size. Detecting the void region corresponds to the segmentation problem in image processing. From the gray scale images of fracture surfaces under study, it is observed that voids are in general of low intensity and the boundary of a void is of higher intensity. We intend to extract the closed contour of the voids. Thus, the proposed methodology consists of following steps:

- Detection of closed contour of voids.
- Refinement of void contour.

These steps are detailed in following sections.

5.3.1 Detection of closed contour of voids

A sample fractograph is shown in Figure 5.1(a). It can be observed that there exists large number of voids separated by white boundaries. Voids are mostly of low intensity. But variation in intensity exists within the voids and also around the boundaries. As a result simple edge detection technique gives rise to additional edges apart from the boundaries. Hence, we followed the intensity based thresholding method for obtaining the high intensity boundary pixels. But it is not guaranteed that closed boundary will be obtained. In order to obtain the closed contour (boundary) of the voids, we considered the following steps:

- Intensity based Thresholding.
- Detection of preliminary contour.
- Formation of closed contour of voids.

Intensity based thresholding

It can be observed in Figure 5.1(a) that voids possess low intensity values and the boundaries separating the voids are brighter in appearance. Thus any intensity based threshold technique can be applied to convert the grayscale image into a binary one. Two levels will correspond to void region and the boundary. Since the intensity histograms of the fractographs are bimodal in nature, we relied on Otsu technique [64] to select the threshold. It selects an optimal threshold that maximizes the separability of the resultant classes in grayscale image. Finally, pixels with intensity more than the threshold are represented as black and the other pixels are converted to white. A fractograph image and the corresponding thresholded image are shown in Figure 5.1(a) and Figure 5.1(b) respectively.

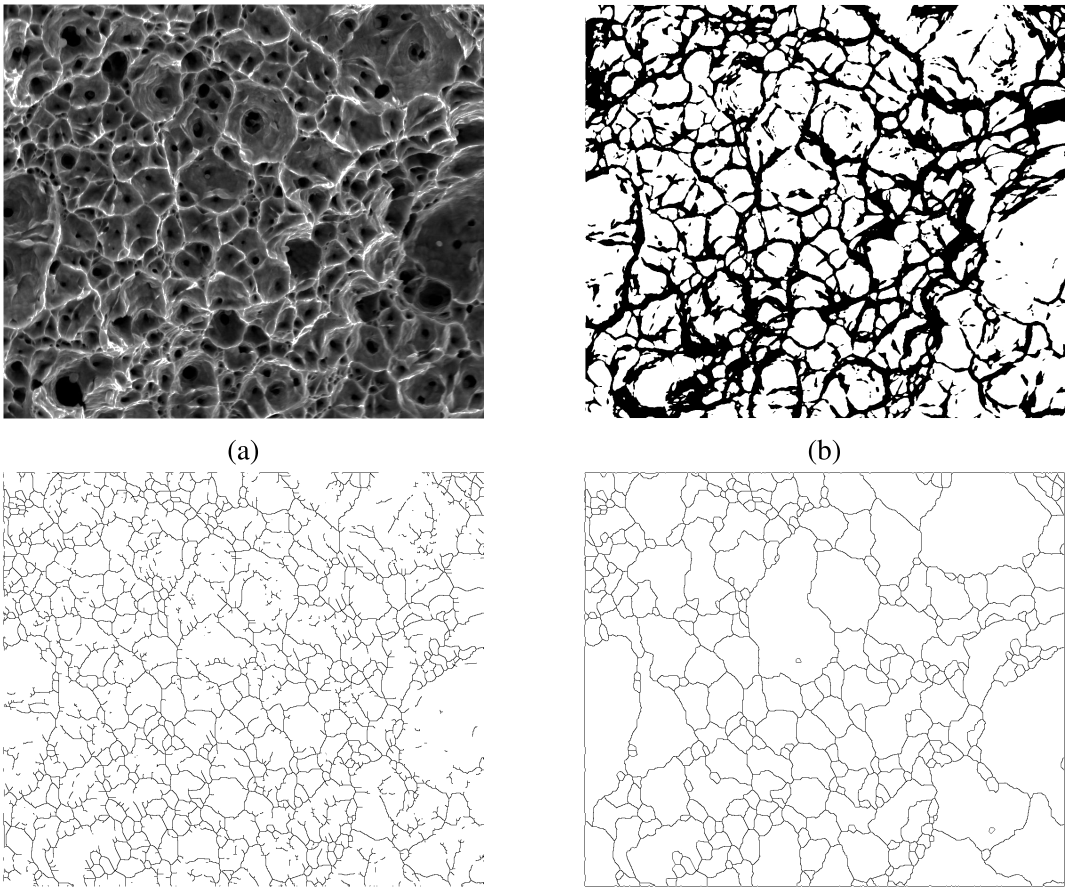

(a) (b)

(c) (d)

Fig. 5.1 Stepwise output of closed contour detection: (a) Sample fractograph, (b) Output After thresholding, (c) Thinned image and (d) Detected closed contour.

Detection of preliminary contour

In this step the primary goal is to form the initial contour of the voids. The thresholded image in Figure 5.1(b) reveals that the boundaries can have discontinuities. Moreover similar intensity value around the boundaries results into thick boundary. Pixels within the voids with higher intensity values may also be erroneously categorized as boundary pixels. From these observations initially a morphological closing [67] operation has been performed to minimize the discontinuity in boundaries. In the present work 5 x 5 structuring element has been considered as a larger structuring element may eliminate some small voids. After the closing operation, thinning algorithm [66] has been applied to get rid from the thick boundary to make it of single pixel width. The result obtained after thinning operation is shown in Figure 5.1(c). However, it is observed that the issue of discontinuity is not completely resolved.

Formation of closed contour of voids

At this stage the goal is to obtain the closed contour of voids. For this purpose the open edge segments have been removed based on component labelling [67]. A component stands for a unit consisting of spatially connected pixels with similar property. The basic principle is that a white pixel is taken as the seed. All its neighbouring white pixels are considered to be part of same component. For every included white pixel the component grows recursively till any black (contour) pixel is encountered. Finally, the component is taken as a void region and outer contour of the component is taken as closed contour of the void. The process further continues by considering a seed from the remaining white pixels which are not part of any component identified so far. When no white pixel is left, component labelling is complete and thereby closed contours of the voids are also extracted. The closed contour thus obtained corresponding to Figure 5.1(a) is shown in Figure 5.1(d).

5.3.2 Refinement of void contour

The contour obtained so far is based on the global characteristics of the fractograph. Local intensity and its variation have been ignored. As a result certain weak edges were missed and that resulted into porous contour. In turn, subsequent component labelling may merge multiple neighbouring voids. A sample fractograph is shown in Figure 5.2(a) and corresponding void contour is shown in Figure 5.2(b). The marked areas reflect the merging of multiple voids. Hence, it is required to refine the contours by considering the local information. The refinement process is restricted within the large components (voids). The steps of refinement are as follows

- Splitting of large components.
- Formation of final contour.

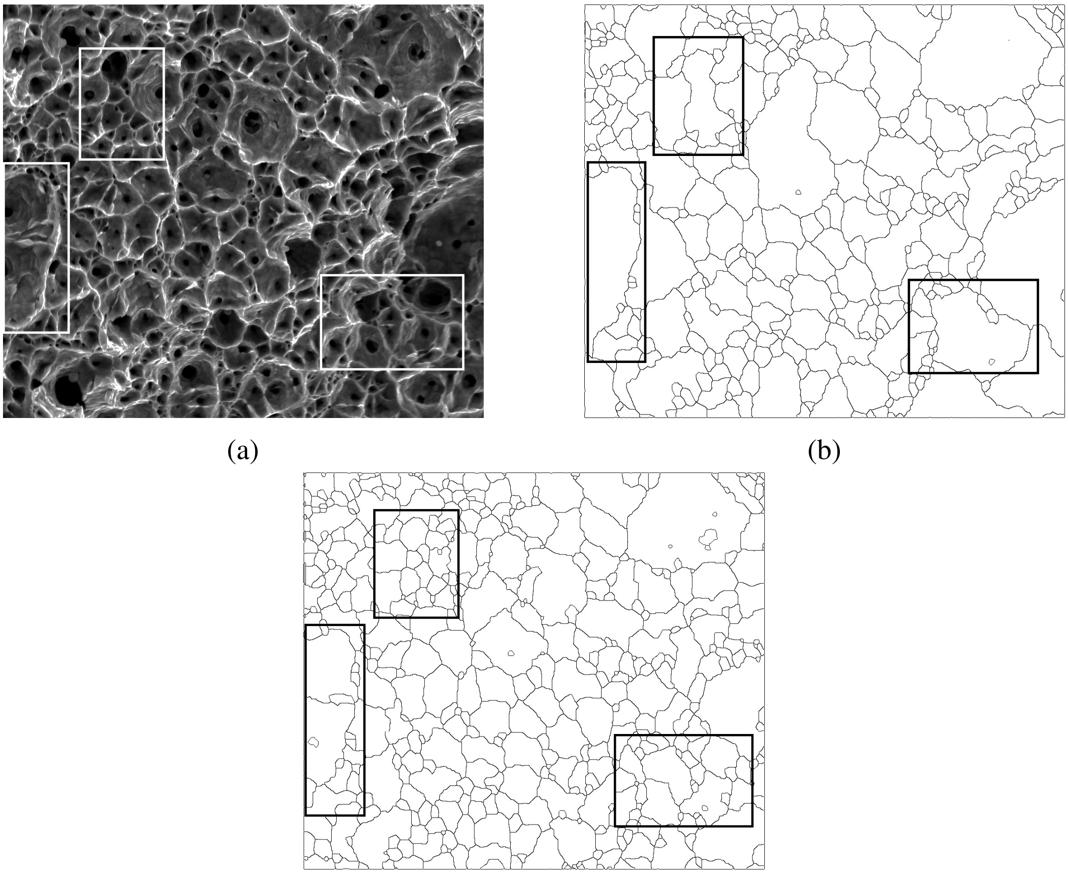

(a) (b) (c)

Fig. 5.2 (a) Sample fractograph, (b) Initial contour of voids and (c) Refined contour of voids. Marked regions indicate the areas that required refinement.

Splitting of large Components

The voids obtained so far vary in their sizes. Because of the removal of some local boundaries, erroneously certain large voids may be identified. To take corrective measures, large voids (components) are to be defined first. Voids with area more than $\mu + \sigma$ are considered as large void, where μ and σ correspond to mean and standard deviation of the area of the voids. Each of the identified large voids has been considered as the mask on the original gray scale image. On each masked region thresolding, closing and thinning operations as described in Section 5.3.1 have been applied. As focusing on local regions, intensity distribution of the specific region will come into play revealing additional boundary pixels.

Formation of final contour

The new edge segments detected in the large components may not form the closed contour. We refer such edges as open edges. To ensure the division of large voids, linking of the open edges has been attempted as follows.

For each open edge, open end point is first determined. An edge pixel with only one more edge pixel in its 3×3 neighbourhood is marked as open end point. Let P be an open end point. All the edge points in its $K \times K$ neighbourhood are the possible elements with which P can be linked. One among these elements is chosen based on their similarity of gray level intensity. If no edge pixel is found in the neighbourhood then search is continued by increasing K. In our work, initially K was taken as 4 and restricted to 7 for avoiding over splitting. Still open edges may exist which could not be linked. Such spurious edge segments were pruned following the component labelling based scheme discussed in Section 5.3.1. The final output is shown in Figure 5.2(c). Marked regions indicate the refinement over the initial contours. This methodology has been applied on the fractograph of tensile fracture surfaces of each specimen to obtain the closed contour of the voids present.

5.4 Experimental Result

The steel used in the present investigation was a commercial variety 304 austenitic stainless steel. The chemistry of the steel in wt. pct is: C-0.05, Ni-8.0, Cr-18.2, Mn-1.6, Si-0.40, S-0.02, P- 0.02, Mo-0.39, Ti-0.0001. Round section specimen blanks of 14 mm diameter and 120 mm length were solution annealed at 1100^oC for 60 minutes and then quenched in water at ambient temperature ($\sim 25^oC$). Micro-structure of the solution annealed specimens was developed following usual metallographic polishing and etching techniques. Etching was done using Glycergia (1 part Glycerol, 3 parts HCl and 1 part HNO_3). The polished and etched specimens were observed in optical microscope (Leica DM 2500M) and the optical image of the micro-structure were captured with the help of digital camera, Leica DFC550, interfaced with a personal computer. From these optical images grain size of the investigated steel was measured using ImageJ software.

Tensile specimens were fabricated out of the solution annealed specimen blanks. Tension tests were done under strain-control mode at four different strain rates in a computer controlled servohydraulic universal testing machine of ± 100 kN capacity at ambient temperature (25^oC). The tests were done and data acquisition was accomplished using InstronBlueHill Tensile test software. The tensile fracture surfaces were carefully preserved and examined in a scanning electron microscope (Jeol, JSM6360) under secondary electron imaging mode. These fractographic images were used for

Fig. 5.3 Micro-structure of solution annealed 304 stainless steel.

Table 5.1 Results of Tensile Tests.

Strain rate (per sec)	0.2 pct offset yield strength (MPa)	Tensile Strength (MPa)	% Uniform elongation	% Total elongation	% Reduction in area
10^{-4}	221	665	76.14	88.20	84.30
10^{-3}	235	622	70.94	86.00	81.70
10^{-2}	264	597	53.96	69.13	80.60
10^{-1}	278	577	51.25	67.30	75.23

developing the automated procedure to quantify different parameters of the voids constituting the tensile fracture surfaces.

Optical microscopy reveals that the solution annealed micro-structure of the steel consists of polyhedral grains of austenite with annealing twins dispersed in some grains as shown in Figure 5.3. The average grain size was found as 68 microns as measured by using ImageJ Software.

Tensile test results at different strain rates are shown below, Table 5.1. In the present investigation it is observed that while yield strength increases tensile strength is decreased with increase of strain rate, Figure 5.4. Generally, it is a common belief that both yield and tensile strength are increased with increase of strain rate. However, whether tensile strength would always increase with increase of strain rate in all types of materials is not universally true. There are existing reports where it is found that with increase of strain rate yield strength increases and tensile strength decreases in case of 304L and 304 steel [100, 101]. In the present investigation it is found that this variation of yield strength and tensile strength with strain rate follows power relationship with very good correlations ($R^2 > 0.97$). Similar variation of yield strength and tensile strength with strain rate has also been reported by Kundu et al. [102] in case of 304 stainless steel.

When considering the ductility parameters (e_u, e_t and R.A) it is observed that the tensile ductility decreases with increase of strain rate. The degree of reduction of uniform and total strain with increase of strain rate is quite substantial with increase of strain rate from 10^{-3} to 10^{-2} per sec.

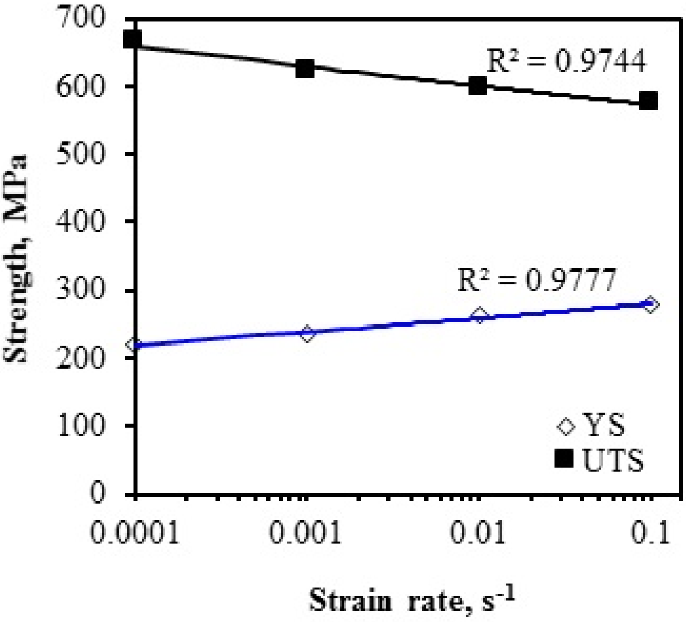

Fig. 5.4 Effect of strain rate on the variation of yield strength and tensile strength.

It is interestingly observed that trend in the variation of uniform and total strain with strain rate is exactly same and follows a pattern which shows an upper shelf at low strain rates and a lower shelf at high strain rates with an intermediate transition region, Figure 5.5. Exactly similar behaviour is observed in case of impact toughness variation of ferritic steel with lowering of temperature. Though for all strain rates the investigated steel failed in a ductile manner, the present results indicate that with change in strain rate the fracture surface morphology will also be changed and that will bear a similar correlation with tensile ductility as that observed with strain rate.

The tensile fracture surfaces were examined in scanning electron microscope. Scanning electron fractographs of the tensile fracture surfaces of the specimens at different strain rates of 10^{-1}, 10^{-2}, 10^{-3} and 10^{-4} s^{-1} are shown in Figure 5.6((a) - (d)) respectively. It is found irrespective of strain rate failure of specimens occurred through void nucleation and growth and thereby a complete dimple fracture surfaces characteristic of ductile fracture were developed. The void networks after application of proposed image processing based methodology corresponding to each of the fractographs (Figure 5.6((a) - (d))), have been shown in Figure 5.6((e) - (h)).

It is observed that fracture surfaces contain a number of voids of different sizes. In the present study the variation of average void diameter, number density of voids as a function of strain rate have been studied. To obtain void diameter, first area of a void has been computed. Thereafter, considering the void as circular in shape, its radius and hence the diameter has been estimated. It is found that each of the fractographs consists of very large fraction (0.6 to 0.7) of small voids. These large fraction of

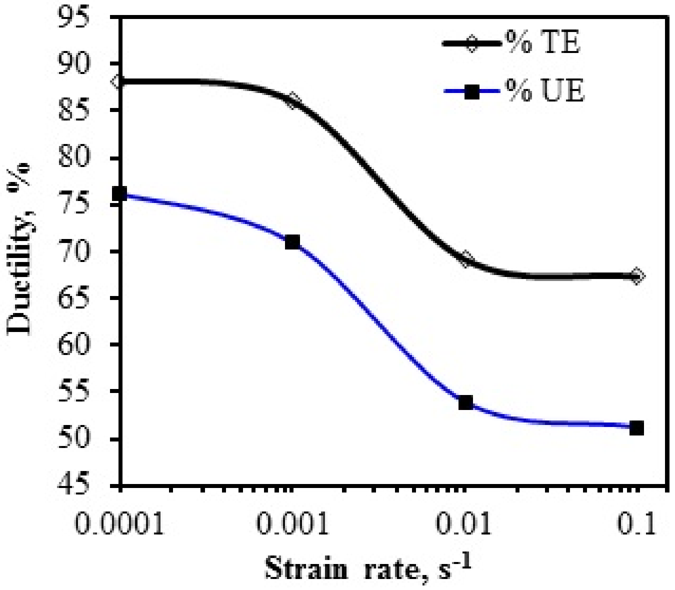

Fig. 5.5 Effect of strain rate on the variation of tensile ductility.

small voids dominates over the large voids in the estimated average void diameter. As a result global average diameter when estimated taking account of all small and large voids lies in a close range (2.11 μm to 2.40 μm) at different strain rates. But, it is worthwhile to mention that the area fraction of these small voids is only 0.17 to 0.24. Hence, to study the variation of average void diameter we considered only the large voids whose diameters are larger than the global average diameter assuming that the tensile properties of the steel under investigation would correspond by the features of those voids that cover more than three-fourth area fraction of the fractographs.

It is found that while the average diameter of the large voids increases with increase of strain rate, the number density of large voids is decreased with strain rates, both following very good power relationship as shown in Figure 5.7. Further, a very beautiful inverse linear relationship is obtained between average circular diameter and number density of large voids as in Figure 5.8. The inverse relationship between number density and average circular diameter of the voids is well expected. But, it is difficult to comment whether the relationship between these two parameters will always be linear in all types of materials and test conditions. In the work of Das et al. [22] these two parameters were shown to be related through inverse power relationship in case of 304LN steel.

In order to see how the void size and density are related with strength and ductility of the investigated steel yield strength and tensile strength have been plotted against average circular diameter and number density of the voids. As shown in Figure 5.9 and Figure 5.10 it is observed that yield strength and tensile strength linearly varies both with average diameter and number density of voids, but in opposite direction. The tensile ductility parameters of the steel at different strain rates, *e.g.*

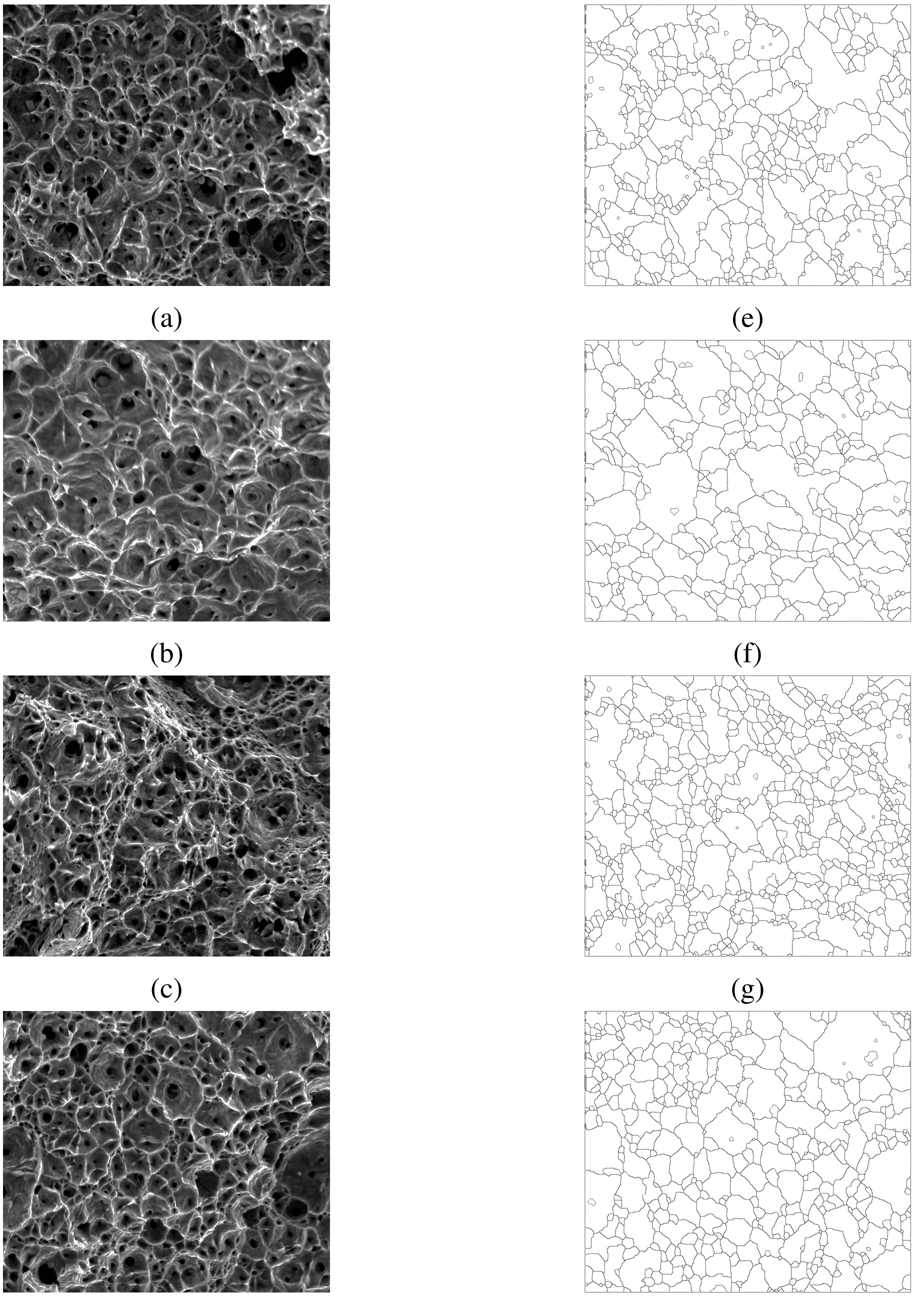

(a) (e)

(b) (f)

(c) (g)

(d) (h)

Fig. 5.6 (a) - (d) Tensile fracture surface of stainless steel at strain rate 10^{-1}, 10^{-2}, 10^{-3} and 10^{-4} s^{-1} respectively at elevated temperature $1100^{o}C$ and (e) - (h) Corresponding void network after application of proposed methodology.

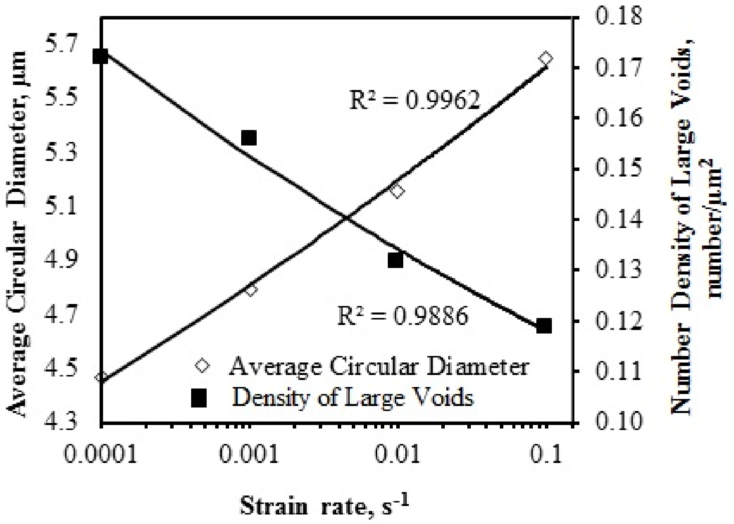

Fig. 5.7 Effect of strain rate on the variation of average circular diameter and number density of voids.

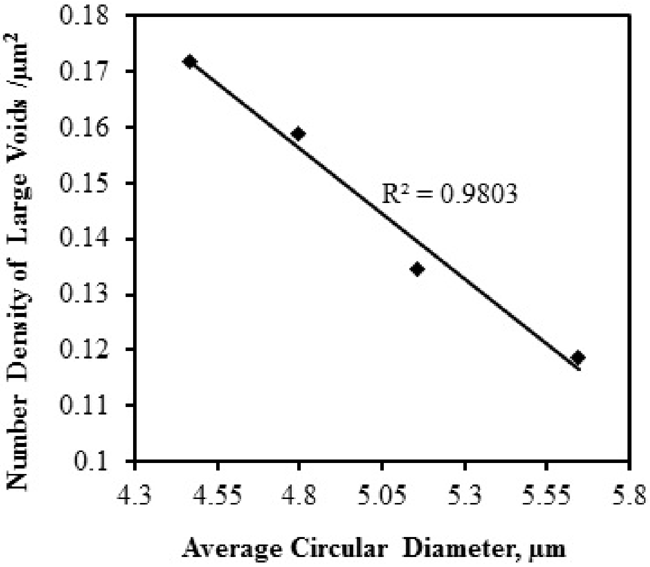

Fig. 5.8 Relationship between number density and average circular diameter of the voids.

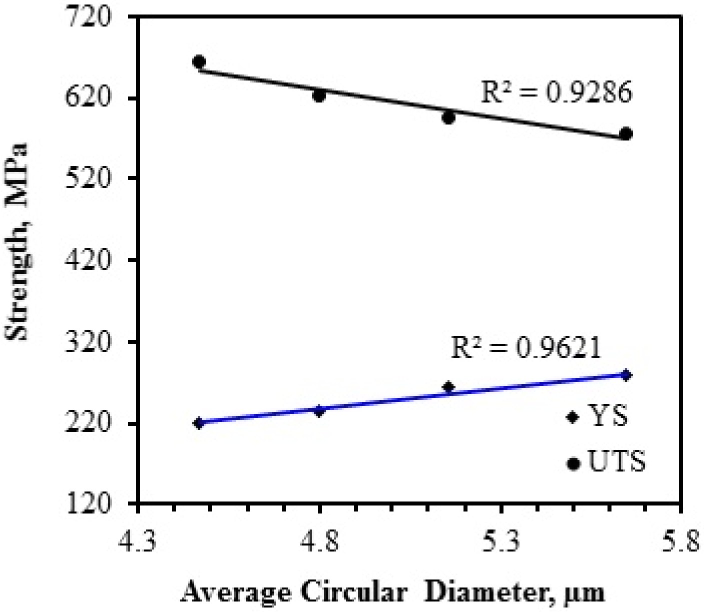

Fig. 5.9 Relationship between average circular diameter of the voids and Strength properties.

uniform and total elongations, have also been plotted against average circular diameter and number density of voids. As shown in Figure 5.11 one can see that the variation of tensile ductility with average circular diameter follows exactly similar pattern as that has been observed with strain rate, Figure 5.5. Because of the linearly inverse relationship of the average void diameter with number density of voids (Figure 5.8) the variation of tensile ductility with number density of voids follows an opposite pattern (Figure 5.12) to what is shown in Figure 5.11.

The present results thus show that tensile fracture morphologies can very well correlate the tensile properties. However, for one-to-one correspondence of mechanical properties of different materials under different test conditions a large data bank is required. The present automated technique to analyse the fractographs can be helpful in this venture.

5.5 Summary

An automated system based on image processing techniques has been proposed for extracting the voids in fractograph. The void extraction process involves a sequence of operation and finally closed contours of the voids are obtained. However, it does not require any intervention of the end user and prior knowledge of image processing is also not essential. The study reveals that void features, like void size and void density at different strain rates bear good correlations with tensile properties of ductile materials.

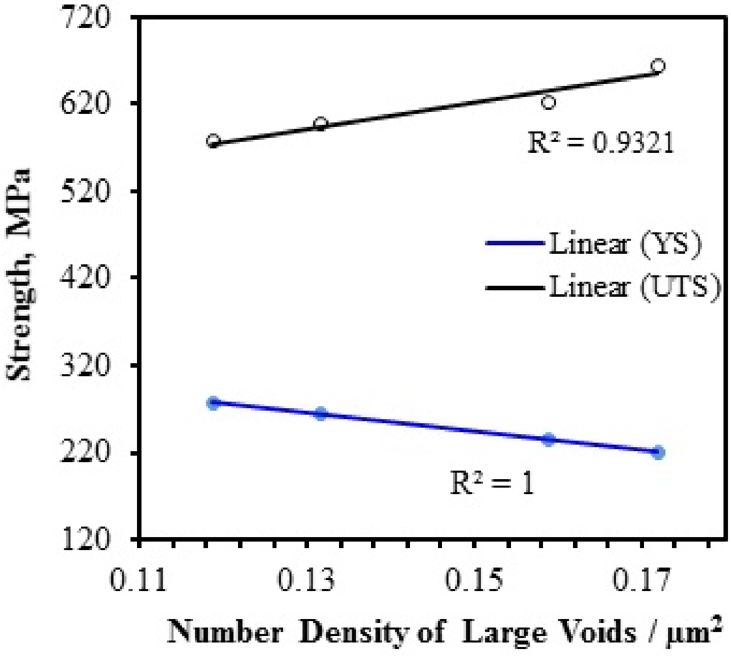

Fig. 5.10 Relationship between number density of large voids and Strength properties.

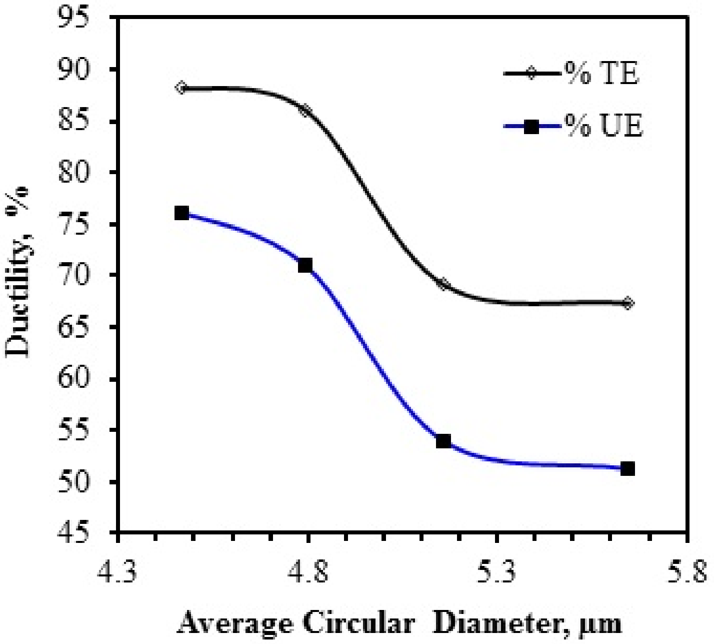

Fig. 5.11 Relationship between average circular diameter of the voids and Ductility properties.

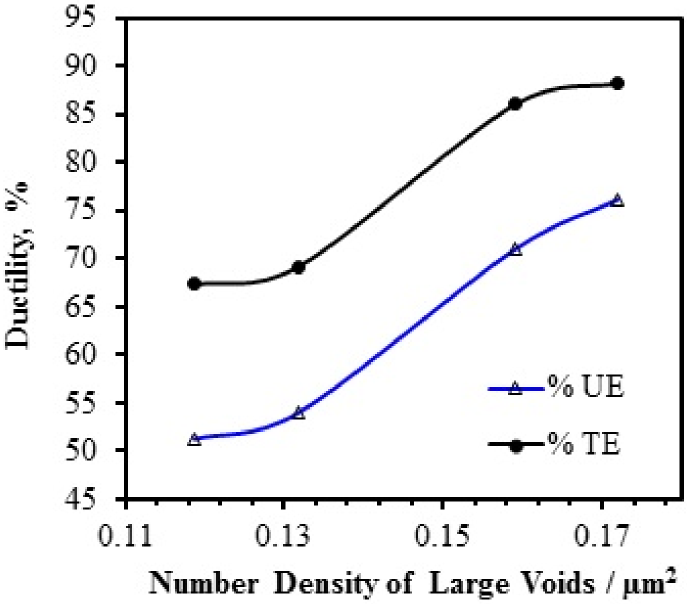

Fig. 5.12 Relationship between number density of large voids and Ductility properties.

Chapter 6

Conclusion and Future Scope

Metals and alloys are extensively used for engineering purpose. Strength, ductility, toughness, creep, wear or abrasion, fatigue etc. are generally considered to be some very important mechanical properties of the materials in different applications. Properties of metals and alloys are governed by their micro-structures which are evolved through different thermal and mechanical processing. Hence, the study of micro-structure of metals and alloys is very important.

The properties which are largely governed by grain size are: yield strength, tensile strength, toughness, ductility, fatigue strength, creep strength and susceptibility to brittle fracture. Knowledge of grain size is, therefore, very important. In case of materials with micro-structures of multiple phases, relative volume fraction of phases concerned governs the average properties of the material. Grain size and phase volume fraction help in correlating the average or macro level strength property of the material. It is known that deformation response of all the grains under the influence of external load cannot remain same and depends upon the crystallographic orientation of the grains with respect to the loading axis and also on the orientation of the surrounding grains. As a result, investigation towards understanding the nature of micro-level deformation is essential. Micro-structure controls the deformation behaviour of any material; it is also connected with the fracture or failure of a component during service. It becomes necessary to understand the role of micro-structure on the fracture processes. With this background, the objective of present work was to develop image processing based automated methodologies for analysing the micro-structures of material and fracture surface. In this respect four tasks have been considered which are: (i) studying grain size distribution in the micro-structure of single phase material, (ii) measuring the volume fraction of different phases present in a material, (iii) studying micro level deformation in a single phase material and finally, (iv) studying distribution of void in a ductile fracture surface. To fulfil the objectives, developing the segmentation methodologies to extract the regions of interest (grain, phase and void) becomes the significant task.

In Chapter 2, the methodology developed for grain identification and grain size analysis has been described. Commercially available image analysis software which works with gray level thresholding are routinely used for this purpose. It requires clear discrimination between grain body and grain boundary. In reality it can not be ensured because of non uniform etching of polished specimen surface. The proposed methodology is edge oriented and quite robust. On the edge image, a sequence of post-processing operations (like, edge linking, removal of spurious edges) are carried out to form the closed contour. Despite the intensity variation within the grain and similarity between the intensities of grain boundary and grain interior, closed contours obtained by present methodology can well approximate the actual grain. The computed grain size is found to be very close to ASTM reference value. The performance has also been compared with other methods, which consider the commonly used threshold based segmentation.

Chapter 3 has detailed the methodology for phase identification and phase volume fraction measurement. The major task is to identify the phases present. We have worked with two different material namely dual phase steel and titanium alloy. In the dual phase steel two phases correspond to two different intensity levels. But non uniform intensity values in a phase and overlap between the phase and phase boundary pose the challenge. It limits the effectiveness of commercial packages. Proposed methodology though relied on thresholding but carried out post-processing to address the challenges. It has well separated the grain boundary and white (martensite) phase despite of their similarity in terms of intensity value. Moreover, it has dealt with the trapped ferrite and splitted martensite regions by introducing the concept of neighbourhood. In case of titanium alloy there is primary α phase and transformed phase consisting of α/β lamellar matrix. The primary challenge is to extract two types of α (both having similar intensity) and β. Simple thresholding cannot identify the phase, particularly two types of α. Proposed methodology has discriminated them based on geometric property.

In chapter 4 an automated methodology for local strain analysis has been described. The simplest case is to study the grain level behaviour for a single phase material. In this work we have investigated the tensile deformation of IFHS steel. The specimen is put under varying load and a sequence of micrographs at different load conditions are studied. Proposed methodology extracts the grains and tracks them over the sequence of micrographs. It uses artificial grids over the images and does not require any other sophisticated experimental technique to lay the grids on the specimen surface itself. Finally, grain level strain is measured. It has been observed that deformation is heterogeneous.

Present scope of the work includes the study of ductile fracture. The methodology has been elaborated in Chapter 5. Stages of ductile fractures (like, void nucleation, void growth and void coalescence) result into dimple fracture surface. Void size and their distribution are well connected to the deformation process leading to failures. An automated methodology has been proposed to extract the voids and to find their size and distribution. The study has also revealed that void features, like void size and void density at different strain rates bear good correlations with tensile properties of ductile materials.

The salient feature of the methodologies is that no intervention from the end user is required. Moreover the usage and outcome are not prejudiced by the prior understanding of image processing. In case of grain size analysis extraction of grains are important step. The methodology successfully extracts the grains even if the grain boundaries are not properly revealed. For quantification of phase volume fraction the proposed methodology has taken care in isolating different phases even in images with low contrast and non-uniform brightness. One of the major advantages of the proposed methodologies for grain level strain measurements, lies in its capability for tracking of any grain starting from initial state to any amount deformation and subsequent grain level strain measurement. Further the feature associated with artificial grid pattern obviates the difficulty of putting grid pattern on specimen surface using lithography technique. In case of analysis of ductile fracture surfaces the methodology is very rapid and has the capability for analyzing large number of fractographs.

Future Scope: The present work though devised automated methodologies required for grain size analysis, quantification of phase volume fraction, local strain analysis and for ductile fracture surfaces, it requires direct correlation of the outputs obtained from these methodologies with mechanical properties to find the promise of the methodologies. To do so, it requires comprehensive testing of the methodologies over a large number of specimens of different materials with the objective to correlate with mechanical properties. In this task, a handshaking between two communities, namely image processing and materials science is required. In most of the analysis, segmentation plays major role. Deep learning can be applied for the same. To make it feasible, in future, efforts may be directed in preparing a benchmark dataset of large volume and variety. It will further help to validate the outcome of analysis.

References

[1] S. Berbenni, V. Favier, and M. Berveiller. Micro–macro modelling of the effects of the grain size distribution on the plastic flow stress of heterogeneous materials. *Computational Materials Science*, 39(1):96–105, 2007.

[2] B. Raeisinia, C. W. Sinclair, W. J. Poole, and C. N. Tome. On the impact of grain size distribution on the plastic behaviour of polycrystalline metals. *Modelling and Simulation in Materials Science and Engineering*, 16(2), 2008.

[3] K. J. Kurzydlowski and J. J. Bucki. Flow stress dependence on the distribution of grain size in polycrystals. *Acta Metallurgica et Materialia*, 41(11):3141–3146, 1993.

[4] E. O. Hall. The Deformation and Ageing of Mild Steel: III Discussion of Results. In *Proceedings of the Physical Society, Section B*, pages 747–753, 1951.

[5] N. J. Petch. The Cleavage Strength of Polycrystals. *Journal of Iron Steel Institute*, 174:25–28, 1953.

[6] K. Hashimoto and H. Margolin. The role of elastic interaction stresses on the onset of slip in polycrystalline alpha brass-I. experimental determination of operating slip systems and qualitative analysis. *Acta Metallurgica*, 31(5):773–785, 1983.

[7] A. Musienko, A. Tatschl, K. Schmidegg, O. Kolednik, R. Pippan, and G. Cailletaud. Three-dimensional finite element simulation of a polycrystalline copper specimen. *Acta Materialia*, 55(12):4121–4136, 2007.

[8] M. Kamaya, Y. Kawamura, and T. Kitamura. Three-dimensional local stress analysis on grain boundaries in polycrystalline material. *International Journal of Solids and Structures*, 44(10):3267–3277, 2007.

[9] P. V. Makarov, S. Schmauder, O. I. Cherepanov, I. Yu, V. A. Smolin, R. R. Ramanova, D. Balokhonov, Y. Saraev, E. Soppa, P. Kizler, G. Fischer, S. Hu, and M. Ludwig. Simulation of elastic-plastic deformation and fracture of materials at micro-, meso- and macro levels. *Theoretical and Applied Fracture Mechanics*, 37(1-3):183–244, 2001.

[10] A. Rusinko. Non-Classical Problems of Irreversible Deformation in Terms of the Synthetic Theory. *Acta Polytechnica Hungarica*, 7(3):25–62, 2010.

[11] E. M. Gunel and C. Basaran. Micro-deformation mechanisms in thermoformed alumina trihydrate reinforced poly (methyl methacrylate). *Materials Science and Engineering: A*, 523(1-2):160–172, 2009.

[12] K. J. Kurzydlowski. Microstructural refinement and properties of metals processed by severe plastic deformation. *Bulletin of the Polish Academy of Sciences, Technical Sciences*, 52(4):301–311, 2004.

[13] I. Okipnyi, P. Maruschak, A. Sorochak, and F. Sergejev. Measurement of deformation hardening of heat-resistant steel of the WWER-type reactor. In *Proceedings of 8th International DAAAM Baltic Conference on Industrial engineering, Tallinn, Estonia*, pages 694–699, 2012.

[14] J. Piwnik and K. Mogielnicki. Deformations in micro extrusion of metals. *Archives of Foundary Engineering*, 10(3):87–90, 2010.

[15] P. K. Pradhan, P. R. Dash, P. S. Robi, and S. K. Roy. Micro void coalescence of ductile fracture in mild steel during tensile straining. *Frattura ed Integrità Strutturale*, 19:51–60, 2012.

[16] K. Stoshi, H. Kazuhiro, M. Yanada, I. Minami, Y. Kimura, and S. Ikeda. Direct drawing method for microfabrication based on selective metal plating technology. *Sensors and Actuators A: Physical*, 103(1-2):135–142, 2003.

[17] S. C. Jacobsen, D. L. Wells, C. C. Davis, and J. E. Wood. Fabrication of micro-structures using non-planar lithography (NPL). In *Proceedings of Micro Electro Mechanical Systems, IEEE*, pages 45–50, 1991.

[18] C. Beuret, G. A. Racine, J. Gobet, R. Luthier, and N. F. Rooij. Microfabrication of 3D multidirectional inclined structure by UV lithography and electroplating. In *Proceedings of Micro Electro Mechanical Systems, IEEE*, pages 81–85, 1994.

[19] S. Konishi, K. Honsho, and S. Sugiyama. Direct drawing for microfabrication without photolithography. In *Proceedings of Micro Electro Mechanical Systems, IEEE*, pages 194–199, 1999.

[20] J. Kang. Microscopic Strain Mapping Based on Digital Image Correlation. In *Proceedings of the 11th International Congress and Exposition, Orlando, Florida, USA*, 2008.

[21] M. Gom. *ARAMIS deformation measurement using the grating method.* User's Manual, V5.3.0-8, Braunschweig, Germany, 2003.

[22] A. Das, S. Sivaprasad, P. C. Chakraborti, and S. Tarafder. Correspondence of fracture surface features with mechanical properties in 304LN stainless steel. *Materials Science and Engineering: A*, 496(1-2):98–105, 2008.

[23] A. Das, S. K. Das, S. Sivaprasad, and S. Tarafder. Fracture-property correlation in copper-strengthened high-strength low-alloy steel. *Scripta Materialia*, 59(7):681–683, 2008.

[24] Arpan Das. Martensite – Void Interaction. *Scripta Materialia*, 68(7):514–517, 2013.

[25] ASTM Standard E112-96. *Standard Test Methods for Determining Average Grain Size*. ASTM International, 2004.

[26] ASTM Standard E1382-97. *Standard Test Methods for Determining Average Grain Size Using Semiautomatic and Automatic Image Analysis*. ASTM International, 2015.

[27] S. Beucher and C. Lantuejoul. Use of Watershed in Contour Detection. In *Proceedings of International workshop on image processing, real-time edge and motion detection, Rennes, France*, 1979.

[28] L. Vincent and P. Soilee. Watersheds in digital spaces: an efficient algorithm based on immersion simulations. *IEEE Transaction Pattern Analysis and Machine Intelligence*, 13(6):583–598, 1991.

[29] F. Meyer. Topographic distance and watershed lines. *Signal Processing*, 38(1):113–125, 1994.

[30] T. Roussillon, H. Piègay, I. Sivignon, L. Tougne, and F. Lavigne. Automatic computation of pebble roundness using digital imagery and discrete geometry. *Computers and Geosciences*, 35(10):1992–2000, 2009.

[31] B. Lu, M. Cui, Q. Liu, and Y. Wang. Automated grain boundary detection using the level set method. *Computers and Geosciences*, 35(2):267–275, 2009.

[32] J. Barraud. The use of watershed segmentation and GIS software for textural analysis of thin sections. *Journal of Volcanology and Geothermal Research*, 154(1):17–33, 2006.

[33] G. Gauthier, M. Coster, L. Chermant, and J. Chermant. Morphological Segmentation of Cutting Tools. *Microscopy Microanalysis Microstructures*, 7(5):339–344, 1996.

[34] R. Heilbronner. Automatic grain boundary detection and grain size analysis using polarization micrographs or orientation images. *Journal of Structural Geology*, 22(7):969–981, 2000.

[35] O. Dengiz, A. E. Smith, and I. Nettleship. Grain boundary detection in microstructure images using computational intelligence. *Computers in Industry*, 56(8-9):854–866, 2005.

[36] I. M. Zhuravel and L. M. Svirska. Measurement of the mean grain size in a metal by using fractal dimensions. *Materials Science*, 46(3):418–420, 2010.

[37] H. Peregrina-Barreto, I. R. Terol-Villalobos, J. J. Rangel-Magdaleno, A. M. Herrera-Navarro, L. A. Morales-Hernàndez, and F. Manrìquez-Guerrero. Automatic grain size determination in microstructures using image processing. *Measurement*, 46(1):249–258, 2013.

[38] K. S. Raju, M. G. Krishna, K. A. Padmanabhan, K. Muraleedharan, N. P. Gurao, and G. Wilde. Grain size and grain boundary character distribution in ultra-fine grained (ECAP) nickel. *Material science and Engineering: A*, 491(1-2):1–7, 2008.

[39] J. Liu, D. M. Aruguete, J. R. Jinschek, J. D. Rimstidt, and M. F. HochellaJr. The non-oxidative dissolution of galena nanocrystals: Insights into mineral dissolution rates as a function of grain size, shape, and aggregation state. *Geochimica et Cosmochimical Acta*, 72(24):5984–5996, 2008.

[40] J. Komenda. Automatic recognition of complex microstructures using the Image Classifier. *Materials Characterization*, 46(2-3):87–92, 2001.

[41] ContextVision AB. *Contextvision Users's Guide, MicroGOP2000/S Software V. 3.1*. ContextVision, 1999.

[42] V. H. C. de Albuquerque, A. R. de Alexandria, P. C. Cortez, and J. M. R. S. Tavares. Evaluation of multilayer perceptron and self-organizing map neural network topologies applied on microstructure segmentation from metallographic images. *NDT & E International*, 42(7):644–651, 2009.

[43] O. Chatterjee, K. Das, S. Dutta, S. Datta, and S. K. Saha. Phase extraction and boundary removal in dual phase steel micrographs. In *Proceedings of India Conference (INDICON), IEEE*, 2010.

[44] A. Gruttadauria, D. Mombelli, E. M. Castrodeza, and C. Mapelli. Processing and characterization of dual phase steel foam. *Revista Materia*, 15(2):182–188, 2010.

[45] M. S. Ulstad. An algorithm for estimating small scale differences between two digital images. *Pattern Recognition*, 5(4):323–333, 1973.

[46] M. Sjodahl. Electronic speckle photography: Increased accuracy by non integral pixel shifting. *Applied Optics*, 33(28):6667–6673, 1994.

[47] R. Cintròn and V. Saouma. *Strain Measurements with the Digital Image Correlation System Vic 2D*. Technical report, University of Colorado, Boulder, CO, USA, 2008.

[48] X. Cao, Z. Bi, X. Wei, and Y. Xie. Determination of Poisson's Ratio of Kraft Paper Using Digital Image Correlation. *Mechanical Engineering and Technology*, 125:51–57, 2012.

[49] H. Ghadbeigi, C. Pinna, and S. Celotto. Quantitative Strain Analysis of the Large Deformation at the Scale of Microstructure: Comparison between Digital Image Correlation and Microgrid Techniques. *Experimental Mechanics*, 52(9):1483–1492, 2012.

[50] D. Rugg. Materials for future gas turbine applications. *Materials Science and Technology*, 30(15):1848–1852, 2014.

[51] J. R. Davenport, L. Mendez-Garcia, S. Purkayastha, M. E. Hancock, R. J. Stearn, and W. J. Clegg. Material needs for turbine sealing at high temperature. *Materials Science and Technology*, 30(15):1877–1883, 2014.

[52] J. P. Bandstra, D. A. Koss, A. Geltmacher, P. Matic, and R. Everett. Modeling void coalescence during ductile fracture of a steel. *Material Science and Engineering: A*, 366(2):269–281, 2004.

[53] D. Chae and D. A. Koss. Damage accumulation and failure of HSLA-100 steel. *Materials Science and Engineering: A*, 366(2):299–309, 2004.

[54] A. Das, S. K. Das, and S. Tarafder. Correlation of Fractographic Features with Mechanical Properties in Systematically Varied Microstructures of Cu-Strengthened High-Strength Low-Alloy Steel. *Metallurgical and Materials Transactions A*, 40A:3138–3146, 2009.

[55] Z. Taslicukur, G. S. Altug, S. Polat H. Atapek, and E. Turedi. Characterization of Microstructure and Fracture Behavior of GG20 and GG25 Cast Iron Materials Used in Valves. In *Proceedings of 21st International Conference on Metallurgy and Materials*, 2012.

[56] S. Dutta, K. Barat, A. Das, S. K. Das, A. K. Shukla, and H. Roy. Characterization of micrographs and fractographs of Cu-strengthened HSLA steel using image texture analysis. *Measurement*, 47:130–144, 2014.

[57] S. Banerjee, P. C. Chakraborti, and S. K. Saha. An automated methodology for grain segmentation and grain size measurement from optical micrographs. *Measurement*, 140:142–150, 2019.

[58] S. Banerjee, S. Dutta S. K. Ghosh, and S. K. Saha. Segmentation of dual phase steel micrograph: An automated approach. *Measurement*, 46(8):2435–2440, 2013.

[59] S. Banerjee, S. Bhunia, P. C. Chakraborti, and S. K. Saha. An Automated Approach for Volume Fraction Measurement of Titanium Alloy using Digital Image Processing. In *Proceedings of the 7-th International Conference on Computer and Communication Technology*, pages 95–99, 2017.

[60] S. Banerjee, T. Dasgupta, S. Mukherjee, M. Shome, P. C. Chakraborti, and S. K. Saha. Digital image correlation for grain scale strain measurement in interstitial free high strength steel. *Materials Science and Technology*, 32(4):328–337, 2016.

[61] S. Banerjee, K. Basu, P. C. Chakraborti, and S.K. Saha. Extraction of Region Contour in SEM Fractograph. In *Proceedings of 2nd International Conference on Emerging Applications of Information Technology, IEEE CS Press*, pages 98–101, 2011.

[62] S. Banerjee, K. Basu, P. C. Chakraborti, and S.K. Saha. Segmentation of SEM Fractograph into Void and Surface Region. In *Proceedings of the International Conference on Advances in Materials and Materials Processing (ICAMMP)*, 2011.

[63] J. S. Weszka. A survey of threshold selection techniques. *Computer Graphics and Image Processing*, 7(2):259–265, 1978.

[64] N. Otsu. A Threshold Selection Method from Gray-Level Histograms. *IEEE Transactions on Systems, Man, and Cybernetics*, 9(1):62–66, 1979.

[65] T. W. Riddler and S. Calvard. Picture Thresholding Using an Iterative Selection Method. *IEEE Transaction on Systems, Man and Cybernetics*, 8(8):630–632, 1978.

[66] R. C. Gonzalez and R. E. Woods. *Digital Image Processing*. Prentice Hall, India, 1992.

[67] B. Chanda and D. D. Majumder. *Digital Image Processing and Analysis*. Prentice-Hall, India, 2001.

[68] S. Dutta, A. Karmakar, H. Roy, and K. Barat. Evaluation of primary phase morphology of cooling slope cast Al-Si-Mg alloy samples using image texture analysis. *Journal of Engineering Manufacture*, 227(10):1474–1483, 2013.

[69] A. Campbell, P. Murray, E. Yakushina, S. Marshall, and W. Ion. Automated microstructural analysis of titanium alloys using digital image processing. *Materials Science and Engineering*, 179, 2017.

[70] K. Dutta and K. K. Ray. Ratcheting strain in interstitial free steel. *Materials Science and Engineering: A*, 575:127–135, 2013.

[71] J. Canny. A Computational Approach to Edge Detection. *IEEE Transaction of Pattern Analysis and Machine Intelligence*, 8(6):679–698, 1986.

[72] M. Paulic, D. Mocnik, M. Ficko, J. Balic, T. Irgolic, and S. Klancnik. Intelligent system for prediction of mechanical properties of material based on metallographic images. *Tehnički Vjesnik*, 22(6):1419–1424, 2015.

[73] A. A. Salem, J. B. Shaffer, R. A. Kublik, L. A. Wuertemberger, and D. P. Satko. Microstructure-Informed Cloud Computing for Interoperability of Materials Databases and Computational Models: Microtextured Regions in Ti Alloys. *Integrating Materials and Manufacturing Innovation*, 6(1):111–126, 2017.

[74] A. Campbell, P. Murray, E. Yakushina, S. Marshall, and W. Ion. New methods for automatic quantification of microstructural features using digital image processing. *Materials and Design*, 141:395–406, 2018.

[75] S. M. Azimi, D. Britz, M. Engstler, M. Fritz, and F. Mucklich. Advanced Steel Microstructural Classification by Deep Learning Methods. *Scientific Reports*, 8, 2018.

[76] D. L. Naik, H. U. Sajid, and R. Kiran. Texture-based metallurgical phase identification in structural steels: A supervised machine learning approach. *Metals*, 9(5), 2019.

[77] D. Yang and Z. Liu. Quantification of Microstructural Features and Prediction of Mechanical Properties of a Dual-Phase Ti-6Al-4V Alloy. *Materials*, 9, 2016.

[78] S. K. Saha, A. K. Das, and B. Chanda. Graytone Image Retrieval Using Shape Feature Based On Petal Projection. In *Proceedings of International Conference On Advances In Patern Rcognition*, pages 252–256, 2003.

[79] S. K. Saha, A. K. Das, and B. Chanda. An Automatic Image Segmentation Technique Based on Pseudo-convex Hull. In *Proceedings of Indian Conference on Computer Vision, Graphics and Image Processing*, pages 70–81, 2006.

[80] D. Raabe, M. Sachtleber, Z. Zhao, F. Roters, and S. Zaefferer. Micromechanical and macromechanical effects in grain scale polycrystal plasticity experimentation and simulation. *Acta Materialia*, 49(17):3433–3441, 2001.

[81] B. Pan, K. Qian, H. Xie, and A. Asundil. Two dimensional digital image correlation for inplane displacement and strain measurement: a review. *Measurement Science and Technology*, 20(6):1–17, 2009.

[82] M. Kass, A. Witkin, and D. Terzopoulos. Snakes: Active contour models. *International Journal of Computer Vision*, 1(4):321–331, 1988.

[83] T. McInerney and D. Terzopoulos. T-snake: Topology adaptive snakes. *Medical Image Analysis*, 4(2):73–91, 2000.

[84] F. Meyer and S. Beucher. Morphological segmentation. *Journal of Visual Communication and Image Representation*, 1(1):21–46, 1990.

[85] M. Couprie, L. Najman, and G. Bertrand. Algorithms for the Topological Watershed. *Discrete Geometry for Computer Imagery*, 3429:172–182, 2005.

[86] G. Bertrand. On Topological Watersheds. *Journal of Mathematical Imaging and Vision*, 22(2-3):217–230, 2005.

[87] M. A. Tschopp, B. B. Bartha, W. J. Porter, P. T. Murry, and S. B. Fairchild. Microstructure Dependent Local Strain Behaviour in Polycrystals through In-Situ Scanning Electron Microscope Tensile Experiments. *Metallurgical and Materials Transactions A*, 40(10):2363–2368, 2009.

[88] A. L. Gurson. Continuum Theory of Ductile Rupture by Void Nucleation and Growth: Part I—Yield Criteria and Flow Rules for Porous Ductile Media. *Journal of Engineering Materials and Technology*, 99(1):2–15, 1977.

[89] J. Wen, Y. Huang, K. Hwang, C. Liu, and M. Li. The modified Gurson model accounting for the void size effect. *International Journal of Plasticity*, 21(2):381–395, 2005.

[90] W. Y. Lu, M. Horstemeyer, J. Korellis, R. Grishibar, and D. Mosher. High temperature sensitivity of notched AISI 304L stainless steel tests. *Theoretical and Applied Fracture Mechanics*, 30(2):139–152, 1998.

[91] A. A. Benzerga, J. Besson, and A. Pineau. Anisotropic ductile fracture: Part I: Experiments. *Acta Materialia*, 52(15):4623–4638, 2004.

[92] A. Salemi and A. Abdollah-zadeh. The effect of tempering temperature on the mechanical properties and fracture morphology of a NiCrMoV steel. *Materials Characterization*, 59(4):484–487, 2008.

[93] M. A. Venkataswamy. Scanning Electron Microscopy in Failure Analysis and Accident Investigation. In *Proceedings of National Conference on Scientific Achievements of SC & ST Scientists & Technologists*, pages 125–129, 2009.

[94] R. M. Lobo and A. H. Andrade. Analysis of Fracture Surface of CFRP Material by Three-Dimensional Reconstruction Methods. In *Proceedings of International Nuclear Atlantic Conference (INAC)*, pages 194–199, 2009.

[95] J. Bienias, M. Ostapiuk, and B. Surowska. Fractography and damage analysis of carbon/epoxy composites under static and dynamic loading at elevated temperatures. *Acta Mechanica et Automatica*, 6(1):17–20, 2012.

[96] M. Khokhlov, A. Fischer, and D. Rittel. Multi-Scale Stereo-Photogrammetry System for Fractographic Analysis Using Scanning Electron Microscopy. *Experimental Mechanics*, 52(8):975–991, 2012.

[97] S. Dutta, A.Das, K. Barat, and H. Roy. Automatic characterization of fracture surfaces of aisi 304ln stainless steel using image texture analysis. *Measurement*, 45(5):1140–1150, 2012.

[98] S. Dutta, A. Karmakar, H. Roy, and K. Barat. Automatic estimation of mechanical properties from fractographs using optimal anisotropic diffusion and voronoi tessellation. *Measurement*, 134:574–585, 2019.

[99] I. Konovalenko, P. Maruschak, J. Brezinová, and J. Brezina. Morphological Characteristics of Dimples of Ductile Fracture of VT23M Titanium Alloy and Identification of Dimples on Fractograms of Different Scale. *Materials*, 12(13), 2019.

[100] J. A. Lichtenfeld, C. J. V. Tyne, and M. C. Mataya. Effect of strain rate on stress-strain behavior of alloy 309 and 304l austenitic stainless steel. *Metallurgical and Materials Transactions A*, 37(1):147–161, 2006.

[101] J. Talonen, H. Hanninen, P. Nenonen, and G. Pape. Effect of strain rate on the strain-induced $Y \rightarrow \alpha'$-martensite transformation and mechanical properties of austenitic stainless steels. *Metallurgical and Materials Transactions A*, 36(2):421–432, 2005.

[102] A. Kundu and P. C. Chakraborti. Effect of strain rate on quasistatic tensile flow behaviour of solution annealed 304 austenitic stainless steel at room temperature. *Journal of Materials Science*, 45(20):5482–5489, 2010.

Materials Science and Technology

ISSN: 0267-0836 (Print) 1743-2847 (Online) Journal homepage: https://www.tandfonline.com/loi/ymst20

Digital image correlation for grain scale strain measurement in interstitial free high strength steel

S. Banerjee, T. Dasgupta, S. Mukherjee, M. Shome, P. C. Chakraborti & S. K. Saha

To cite this article: S. Banerjee, T. Dasgupta, S. Mukherjee, M. Shome, P. C. Chakraborti & S. K. Saha (2016) Digital image correlation for grain scale strain measurement in interstitial free high strength steel, Materials Science and Technology, 32:4, 328-337, DOI: 10.1179/1743284715Y.0000000075

To link to this article: https://doi.org/10.1179/1743284715Y.0000000075

Digital image correlation for grain scale strain measurement in interstitial free high strength steel

S. Banerjee[1], T. Dasgupta[2], S. Mukherjee[3], M. Shome[4], P. C. Chakraborti[5] and S. K. Saha*[2]

Deformation measurement of materials and structures subjected to various loading conditions is an important task of experimental solid mechanics. Apart from the widely used point wise strain gauge technique, various full field non-contact optical methods are used for this purpose. In this work, an automated scheme to measure the grain level deformation in tensile deformed interstitial free high strength steel has been introduced. The method is based on digital image correlation technique. The proposed scheme utilised high resolution scanning electron images of the specimen surface that are sequentially captured during tensile loading. It is found that grain to grain there is large variation in deformation response at a given load. The present work also reveals point to point variation of strain within a grain interior.

Keywords: Image correlation, Strain measurement, Grain segmentation, Micrograph processing, IFHS steel

This paper is part of a Special Issue on Thematic Issue on Microstructurally driven materials development

Introduction

Deformation measurement of materials and structures subjected to various loading conditions (mechanical or thermal) is an important task of experimental solid mechanics. The deformation behaviour of different materials under load that are routinely studied is an average response of the microstructure of a material. It is by now established and well documented in the literature that plastic deformation in polycrystalline materials is never homogeneous, whether the material consists of a single phase or multiple phases. Orientation difference of individual grain with respect to the loading axis is responsible for grain to grain variation in plastic deformation even when deformation is macroscopically homogeneous.[1–3] Further, deformation heterogeneity also exists within individual grain. Raabe *et al.*[4] have elaborately discussed the occurrence of deformation heterogeneity within individual grain in coarse grained aluminium specimen. In order to know the influence of different grains and other phases constituting the material's microstructure, sophisticated experimental and finite element modeling techniques are often used. Nowadays, electron back scatter diffraction technique in conjunction with scanning electron microscopy (SEM) is being exploited to understand the deformation heterogeneity in polycrystalline materials. Deformation experiments directly under SEM also provide scope for studying the deformation response of individual grain under load. In this technique, the grain structure and other constituting phases of the material are directly observed during deformation. It is known that the deformation characteristic of individual grain depends on its crystallographic orientation and also on the orientation of the surrounding grains with respect to loading axis. Collectively, the deformation of individual grain controls the average deformation behaviour of a material. As a result, investigation towards understanding the nature of microlevel deformation has gained impetus over the last few years.[5–11] It is worth mentioning that strain measurements at any point in an area of interest are required for better understanding of the deformation behaviour of materials and structural components. For this reason, researchers are interested on a strain map over a specimen surface. Use of digital image processing techniques has enabled such measurements.

Digital image correlation (DIC) is an optical method that uses a mathematical correlation analysis to examine digital image data taken while the specimens are subjected to incremental load. As discussed and reviewed by Qian *et al.*[12], two-dimensional DIC is a practical and effective tool for quantitative in-plane deformation measurement of a planar surface, and it is widely accepted where contact method of strain measurement is difficult. Measurement of small difference in the images supports such correlation.[13] Electronic speckle photography offers a simple and fast technique for measuring in plane displacement fields in solid and

---

[1] R. K. M. Residential College, Narendrapur, South 24 Parganas, West Bengal, Kolkata 700103, India
[2] Computer Science and Engineering Department, Jadavpur University, Kolkata 700032, India
[3] Metallurgical and Material Engineering Department, Jadavpur University, Kolkata 700032, India
[4] Research and Development, Tata Steel Limited, Jamshedpur 831001, India
[5] Metallurgical and Material Engineering Department, Jadavpur University, Kolkata 700032, India

*Corresponding author, email sks_ju@yahoo.co.in

Received 12 February 2015; accepted 25 April 2015
DOI 10.1179/1743284715Y.0000000075

fluid mechanics. An improved algorithm for measuring the correlation between subimages has been presented by Sjodahl.[14] The Vic2D presented by Cintron *et al.*[15] is an innovative approach that uses the DIC technique for strain measurements in a two-dimensional contour map of planar surfaces. But it cannot provide displacement and strain maps after the specimens show cracks because of poor correlation. The maps obtained from the specimen images that show cracks are not adequate to determine the strain values at some locations inside the area of interest. It is also reported that the DIC technique can also used to determine the heterogeneity and severity of deformation in polycrystals.[16] Besides, in situations where it is difficult to measure the strain directly, this technique finds application in knowing macroscopic strain during creep deformation.[17]

A novel microscopic strain mapping technique based on DIC has been developed in recent years for various applications in materials characterisation. In these cases, input is a series of SEM images, and strain mapping is done based on the topographic features of the images. For this purpose, many researchers[18,19] use commercially available optical strain measurement system (ARAMIS), which utilises the DIC methodology. Cao *et al.*[20] have proposed a simple and efficient non-contact method to overcome the difficulties of determining Poisson's ratio using traditional contact method. They used DIC method in their work and obtained the relative deformation of specimens using calibrated CCD images.

Interstitial free high strength (IFHS) steels of 1 to 2 mm thickness find extensive applications in automotive industries for their very good cold formability and reasonable strength properties. Volumes of work have already been done correlating processing parameters with the development of texture that controls the formability of the steel. Our interest is, however, different, and we focused our attention to develop an automated methodology for knowing the deformation pattern of individual grain when a specimen made of 1 mm thick IFHS steel is subjected to incremental load. The impetus for developing such automated methodology stems from the fact that the commercial DIC software that is used to know the local strain distribution using the images as an input works as a black box. This automated methodology has been developed by employing image analysis procedure on scanning electron micrographs captured during deformation.

Experimental

The IFHS steel sheet of 1 mm thickness received from TATA Steel, Jamshedpur, India, has been used in the present investigation. The chemistry of the steel in wt. pct is: Fe–0.0029C–0.39Mn–0.004Si–0.007S–0.05P–0.005Si–0.018Cr–0.044Al – 0.005Cu – 0.001Nb – 0.042Ti–0.0018N. Optical microscopy reveals that the microstructure of the steel consists of polyhedral grains of ferrite, as shown in Fig. 1. The two-dimensional average grain size of the steel is about ASTM 10. Tensile properties of the steel deformed at a strain rate of 10^{-3} sec^{-1} are: Y.S = 189 MPa, T.S = 374 MPa, Uniform elongation = 21 pct, Total elongation = 37 pct.

Tensile deformation experiments were also done directly under SEM using miniature sized tensile specimen fabricated by wire electrodischarge machining process while keeping the specimen axis parallel to the rolling direction. One surface of the specimen was metallographically polished in successive steps, and final polishing has been done using 1 μm diamond paste. The polished specimen has been thoroughly cleaned, dried and then etched with Marshall's reagent in order to reveal the grains lying on the surface. The polished and etched specimen has been deformed under tensile loading at a deformation rate of 1 mm per minute inside the vacuum chamber of an SEM (FEI, Quanta 450). The loading device was screw driven GATAN, UK make tensile/bending deformation stage.

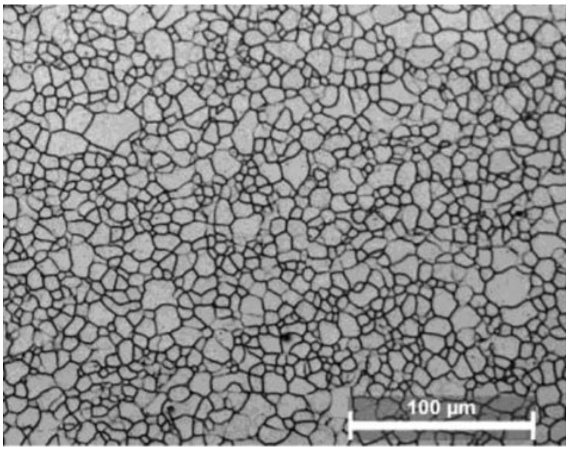

1 Optical microstructure of investigated IFHS steel

It should be noted here that from a number of trial experiments, we observed that the pin loading arrangement of the tensile deformation stage that we used in the present investigation does not accurately measure the specimen strain because of slackness of the loading arrangement, particularly at the low load level. To overcome this difficulty, we measured the specimen strain between two collinear microindentation marks separated by 2000 μm put on the polished and etched specimen surface placed before the deformation experiment. The specimen was then loaded in steps, and high resolution secondary scanning electron images were captured after each step of loading. The strain measured within these two microindentation marks is termed here as global strain. Thus, a series of scanning electron micrographs were obtained until complete fracture of the specimen. These images were subsequently processed to find the grain level deformation pattern. Here, the image in the undeformed condition is called as reference image, and image correlations have been done with respect to this undeformed image to find the grain level deformation. Figure 2 shows a sequence of secondary scanning electron images corresponding to different load levels. The present study is based on these images. The stress and strain corresponding to the images are shown in Table 1.

Proposed methodology for evaluating grain strain

In general, a micrograph reveals the size, shape and distribution of different constituting phases or grains. During deformation of the specimen, grain shape is changed depending upon its size, crystallographic orientation and load level. Additionally, deformation

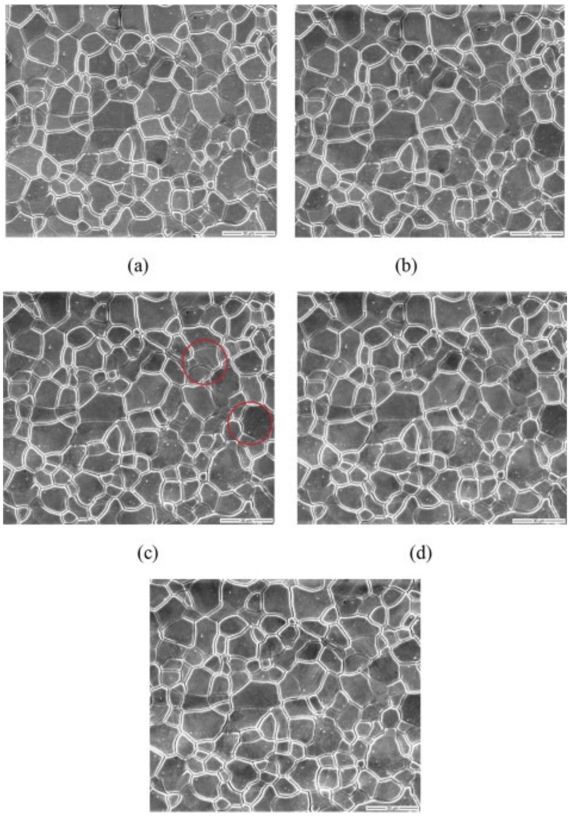

(a) (b)

(c) (d)

(e)

2 Sequence of secondary scanning electron images at different loads

Table 1 Global stress–strain behaviour corresponding to captured micrographs

Micrographs	Stress/MPa	Strain measured experimentally/%
Micrograph 1 (Fig. 2*a*)	0	0.00
Micrograph 2 (Fig. 2*b*)	116	1.14
Micrograph 3 (Fig. 2*c*)	174	2.56
Micrograph 4 (Fig. 2*d*)	233	6.00
Micrograph 5 (Fig. 2*e*)	282	8.26

features, for example, slip lines, also become visible in the high resolution scanning electron micrographs of the deformed specimen. However, crystallographic orientation of the grains with respect to loading axis has not been considered in the present work. The major steps involved in the present study are grain segmentation, tracking the grains in the sequentially captured micrographs and grain level strain measurement. It should be noted here that in the present study the estimation of grain level strain has been done only in the loading direction, that is along the tensile axis, which coincides with the horizontal direction of every image frame.

Grain segmentation

Image segmentation refers to the automatic extraction of the regions of interest from the image. Ideally, a region should be homogeneous in terms of a certain property that characterises the region. Identifying such property is an important task in the segmentation process. A closed boundary separates the segmented region from the rest. One common approach of segmentation is to detect the boundary. Since our aim is to develop an automated process for studying the grain level strain distribution, it becomes necessary to extract the individual grain present in a micrograph.

A sample micrograph composed of a number of grains is shown in Fig. 3*a*. It is observed that a grain is normally enclosed within a boundary that separates it from the adjoining grains. It is also observed that mostly the grains consist of pixels with low intensity values. On the contrary, the boundary pixels are of high intensity values. Our motivation is to detect the closed (without any break/discontinuity) boundary encompassing a grain. However, a simple intensity based threshold technique does not always serve the purpose. There may be weak boundaries with not so high intensity value. Again, different grains may have different intensity levels even though a grain is more or less uniform in terms intensity. Thus, it is possible to have an overlap between the intensity values of the pixels inside the grains and those in the boundaries. As a result, some pixels in the grain may be incorrectly marked as boundary. On the other hand, part of the boundary (weak portions) may be missed out and will give rise to discontinuity. Thus, obtaining the desired closed contours that enclose the grain is a major challenge. Furthermore, the selection of proper intensity value as the threshold is also very difficult. Therefore, a suitable property of the image other than the intensity value is to be explored for segmentation purpose. Careful obser-

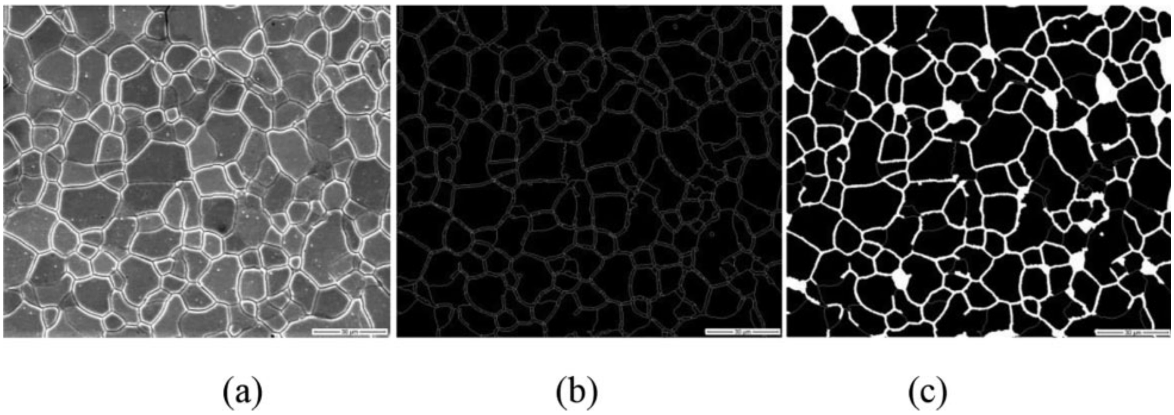

3 Grain segmentation: *a* sample micrograph; *b* output of Watershed algorithm; *c* final output after refinement

vation of the micrographs reveals that contrast can act as a suitable property in the segmentation problem under consideration. Contrast stands for the difference in intensity values between two regions in the image. The grain boundary in the micrograph becomes visible provided there is a perceivable change in contrast between the boundary and the grain interior. With these observations, we look forward to adopt a suitable scheme that generates a closed contour/boundary of the grains.

Determination of grain contours

Active contour models and its variants[21,22] are widely used to determine the closed contour of the objects present in an image. For this purpose, an initial guess of the object contour is required. The final contour is then evolved through minimisation of an energy function. The energy function is defined based on the image feature (e.g., intensity gradient). It has an external energy component that guides the contour towards the object boundary, and the internal energy component resists the deformation of the contour. The major drawback of *the* active contour model is that it requires an initial guess for the contour of each object, and it fails for the touching objects. In our context, the micrograph consists of multiple grains. It is prohibitive for the user to provide the initial guess for the contour of each grain. Moreover, one grain touches another. Hence, the active contour model does not satisfy our requirement.

Watershed transform based algorithms[23–26] are also commonly used in image segmentation, and they also provide a closed contour of the objects present in the image. The concept of watershed was introduced in 1970s. Since then, many improvements have been made on it. In this approach, a gray scale image is considered as a topographic relief where intensity value is thought of as the altitude in the relief. The intuitive idea is to classify the landscape regions as catchment basins and watershed lines. Catchment basins are low altitude regions in the landscape that holds water, and watershed lines (as if, mountains) are of high altitude acting as the barrier between the basins. In a gray scale image, a dark/low intensity area corresponds to basin, and watershed lines are light/high intensity area. A drop of water falling on a topographic relief flows along a path and finally reaches local minima. Intuitively, the watershed of a relief corresponds to the limits of the adjacent catchment basins of the drops of water. The algorithm identifies the basins and the watershed lines separating the basins. In the context of our problem, the grains correspond to the basin, whereas the grain boundaries are the watershed lines.

Watershed based segmentation algorithms can be classified into two major categories. One category focuses on detecting the basins, and the other focuses on finding the watershed lines. Flooding[23,24] belongs to the first category. Such schemes have a tendency of over-segmenting the regions. In a micrograph, the intensity values within and across the grains (basins) vary, and flooding is likely to split a grain into multiple regions. Moreover, a flooding based approach does not preserve the contrast. A topological watershed[26] is directed towards the generation of watershed lines. A graph based implementation is provided in the work of Couprie *et al.*,[26,27] and the mathematical foundation of the work has also been established.[28] A topological watershed algorithm works with the gradient image. Thereby, instead of absolute intensity value, it relies on the local contrast. It focuses on the detection of the contour separating the adjacent basins. The detection uses a parameter **(t)** that specifies the minimal altitude separating the catchment basins. Physically, **t** can be interpreted as the contrast between the grain interior and the grain boundary. Topological watershed preserves contrast and provides closed contour of the grains as desired in our study.

Applying the topological watershed algorithm, the closed contours of the regions are obtained. The value of the parameter **t** needs to be chosen carefully. A low value of **t** oversplits a region as it becomes sensitive to smaller intensity variation. On the other hand, a high value of **t** will accommodate more variation within a region and overlook weak boundaries. In our experiment, a moderate value for **t** is estimated, which approximates the contrast between the grain region pixels (low intensity value) and boundary pixels (high intensity value), and **t** has been taken as $2*\sigma$, where σ is the standard deviation of the intensity values present in the image. The extracted contour for the grains shown in Fig. 3*a* has been presented in Fig. 3*b*, where the white lines are the contour lines.

Refinement of contour

The grain boundaries detected by the watershed algorithm are shown in white in Fig. 3*b*. However, all the enclosed regions shown in black are not grains. It is observed in Fig. 3*a* that the grain boundaries are quite thick because of the deep etching used to reveal them. As a result, the watershed algorithm detects the contrast difference around both inner and outer contours of the white thick boundaries. Finally, all the edges of the thick boundaries are extracted as watershed lines. The small patches enclosed between such lines are also identified as basins (grains). Thus, refinement is required to get rid of such regions that are actually part of the boundary. It is achieved by removing the black regions that are of very small area or by applying morphological closing operation.[29] It may be noted that in this process very small grains may be missed out. Figure 3*c* shows the final output of segmentation obtained after applying the refinement process on Fig. 3*b*. The black region enclosed within the white boundary corresponds to a grain.

Tracking of grains

Once the grains are segmented, each of them has to be uniquely marked in every sequential micrograph. Given the sequence of micrograph, correspondence between the grains also has to be established to enable the measurement of strain at grain level. It involves two steps:

1. Component labelling
2. Finding grain correspondence across the micrographs

In the segmented output, black pixels are part of the grain. Component labelling[29,30] starts with a black pixel and marks it with a label. It also marks the black pixels in its four-neighbourhood with the same label. The process goes on recursively with newly marked pixels. It stops when no further growth is possible. Thus, all the pixels in a particular grain are marked with the same label. The process then continues starting from another unmarked black pixel with a new label. Thus, when no unmarked black pixel is available, all the grains in the micrograph are uniquely labelled.

Pixels with same label belong to same grain. Because of the deformation, grains may undergo changes in terms of their size, shape, displacement and physical orientation. Thus, corresponding grains in two consecutive micrographs may not bear the same label. Therefore, it is not possible to link them based on the assigned labels. In this work, we establish the correspondence based on the proximity of the centroid (CG) of the grains in the consecutive micrographs in the sequence. The CG of a grain is computed based on the spatial moments.[27] The moment of order (p, q) of a grain can be defined by

$$m(p,q)=\sum\nolimits_{c}\sum\nolimits_{r} r^p c^q f(r,c) \tag{1}$$

where $f(r, c)$ is the intensity of the grain pixel at (r, c), r and c spread over the grain. $m(0,1)$ and $m(1,0)$ are the first order moments. $m(0,0)$ is known as the mass of the object. The coordinate of the CG is computed as follows

$$\left(\frac{m(1,0)}{m(0,0)},\frac{m(0,1)}{m(0,0)}\right) \tag{2}$$

The CGs of the grains are computed in each micrograph. Let (r_{ij}, c_{ij}) denote the CG of a grain g_i in the ith micrograph. Corresponding to (r_{ij}, c_{ij}), the nearest CG is searched in the $(i+1)$th micrograph. Suppose the nearest one corresponds to the grain g_k in the $(i+1)$th micrograph. Then, g_i is tracked as g_k in the next micrograph. The process continues over the pairs of successive micrographs, and thereby, the grains are linked. Figure 4 shows the tracking of a few marked grains.

Strain measurement: DIC based technique

For measuring the grain level strain, the intensity values of each micrograph are first normalised. It reduces the impact of contrast/brightness variation (if any) during the capturing of different images. After tracking the individual grain of interest in the series of micrograph, a two-dimensional grid is drawn on that grain for correlation among consecutive images. In this technique, physical grids are not laid on the specimen surface as practised by lithography.[31–34] But in this experiment, an imaginary grid is placed on the reference image. It has been done in a manner so that the grid covers the grains over the area of interest on the specimen surface (Fig. 5*a*). The corresponding grid patterns on subsequent images of the deformed specimen are generated by the correlation technique, as shown in Fig. 5*b–e*.

Correlation among the consecutive micrographs has been established using intensity based similarity. The schematic diagram of image correlation process is shown in Fig. 6. An imaginary grid is placed on the reference image. Figure 6*a* shows such horizontal and vertical grid lines in red colour, and the black squares represent the image pixels. Red squares formed by the intersecting grid lines are referred as subgrids. Each subgrid covers a small region of an image (10 × 10 pixels in our case). Let S_r denotes the set of intersection points of the vertical and horizontal grid lines (i.e. corner pixel of the subgrids) in the reference image. Corresponding to each element in S_r, the corresponding pixel in the next image is determined using intensity based correlation. Let p be an element in S_r with coordinates (X_p, Y_p). There may be a number of pixels in the next image with intensity similar to that of p. To surmount this problem, block matching is considered instead of individual pixel intensity based matching. This is similar to the commonly used approach in estimating the motion in video.

As shown in Fig. 6*a*, a block Br (in blue) centred at p is taken. In our case, the size of the block is 3×3 pixels, and it comprises of the pixel p along with its 8-neighbours. To search the best match for B_r, a search window (SW) is considered in the next image. The search window is of size $K \times K$ (must be larger than the block size), and it is centred at (X_p, Y_p), as shown in green in Fig. 6*b*. In our experiment, K is taken as 11. The best match for B_r is exhaustively searched in SW. A few cases are shown in Fig. 6*c* and *d*. B_r and a block in SW are compared based on the sum of absolute difference (SAD) of the intensity values of corresponding pixels in the blocks. The block in SW with minimum SAD is the adjudged as the match for B_r. The centre pixel of the matched block in SW is taken as the correlated pixel for p. Thus, for each pixel in S_r, a set of correlated points (S_c) in the next image is obtained. Figure 6*e* shows four corner points of a subgrid of reference image in red, and correlated points are in yellow. Correlated points corresponding to each side of the reference subgrid are joined by straight lines, and a deformed subgrid (shown in yellow) is obtained. To continue the correlation process for the subsequent images, S_c obtained in the previous step is taken as S_r for the next image, and the same process is followed.

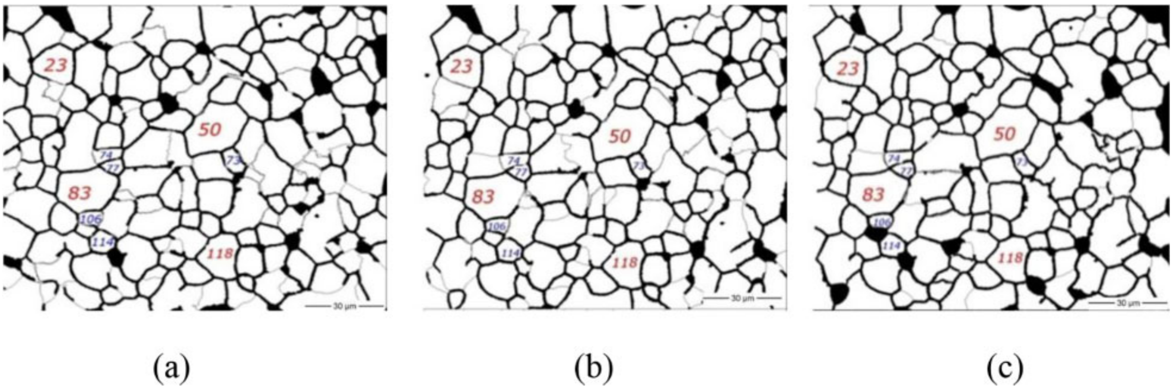

4 Tracked grains in sequence of micrographs: *a* reference micrograph; *b* and *c* corresponding mocrographs under deformed condition

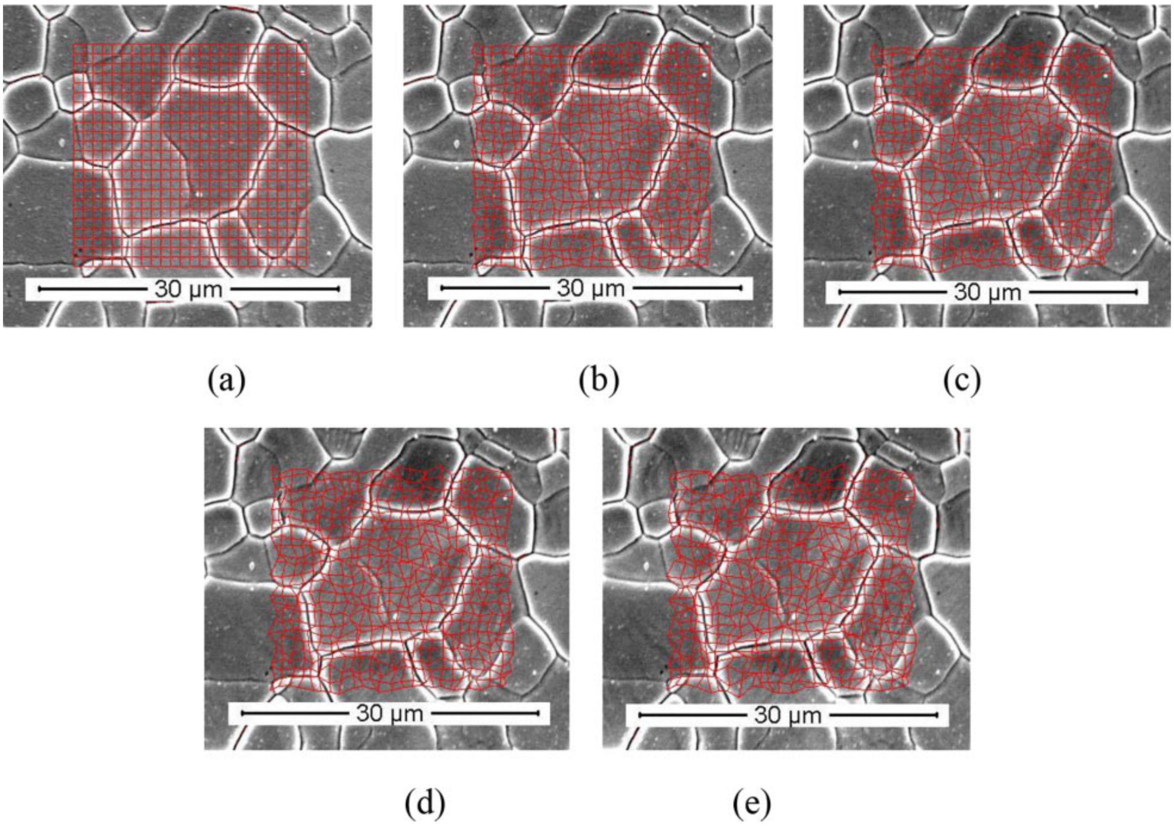

5 ***a*** **grid drawn on portion of reference micrograph and** ***b–e*** **grid drawn by DIC technique on corresponding portion of subsequent micrographs**

To measure the grain level strain at a load, we restrict ourselves within the part of the grid covering the grain of interest. Let the rectangular bounding box with upper left corner (X_l, Y_l) and bottom right corner (X_r, Y_r) enclose the grain in the reference micrograph. After deformation, the bounding box may vary. To accommodate such variation, the rectangular region of the grid with upper left corner ($X_l - 20$, $Y_l - 20$) and bottom right corner ($X_r + 20$, $Y_r + 20$) in the reference micrograph is considered. Furthermore, the subgrids lying in the grain interior are taken into consideration for strain measurement.

Let the length of a side of the subgrids in the reference micrograph be l_0, and l be the length of the corresponding side on the micrograph of subsequent image in the loading direction. Then, the strain is calculated as $[(l - l_0) / l_0]$. The average strain of the grain is determined by averaging the strain of all such sides that are inside the grain. It should be noted here that the deformation of all the subgrids does not always follow the same direction as that of the applied load. As a result, in presence of tensile load, negative deformation of the subgrids frequently occurs. However, the overall deformation of individual grain consisting of subgrids has been found positive. Few grains over which the experiment has been carried out are marked in the reference image and shown in Fig. 7. The average strains for these grains on varying stress are shown in Fig. 8. The detailed strain distribution over the marked grains is also studied. Figure 9 shows the strain distribution over the grain marked 50, as an example, for different load values. The figure also shows the global strain of the particular grain at different loads. Note that the x axis represents the subgrids in the grain in raster scan order.

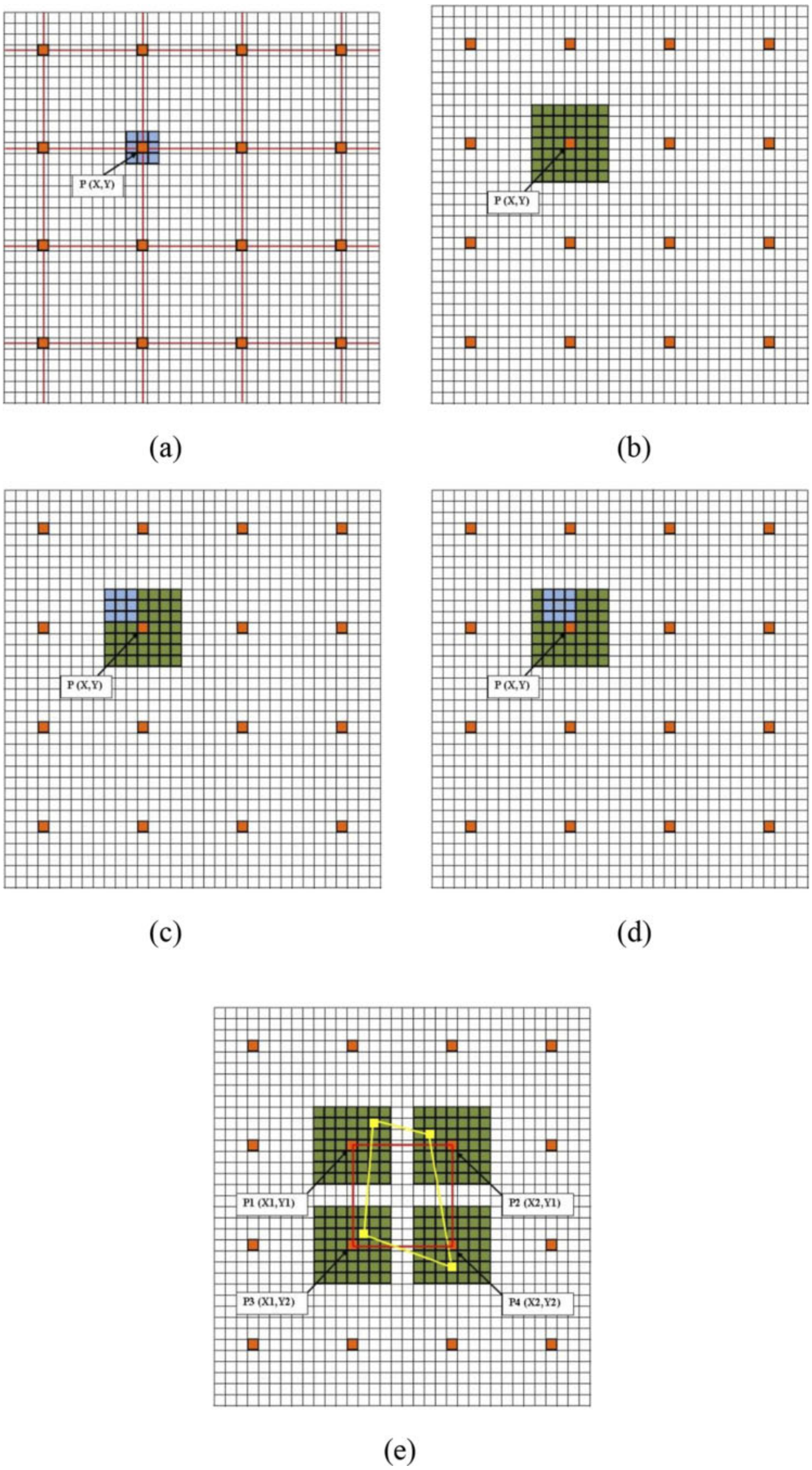

a imaginary grid and block of 8-neighbour pixels (in blue) corresponding to *P*(*X*, *Y*), subgrid corner in reference image; *b* search window (in green) for *P*(*X*,*Y*) in image following reference image; *c*, *d* search process to find match for block around *P*(*X*,*Y*) in search window; *e* subgrid of reference window (in red) and corresponding deformed subgrid (in yellow) superimposed on reference image

6 Schematic diagram for DIC

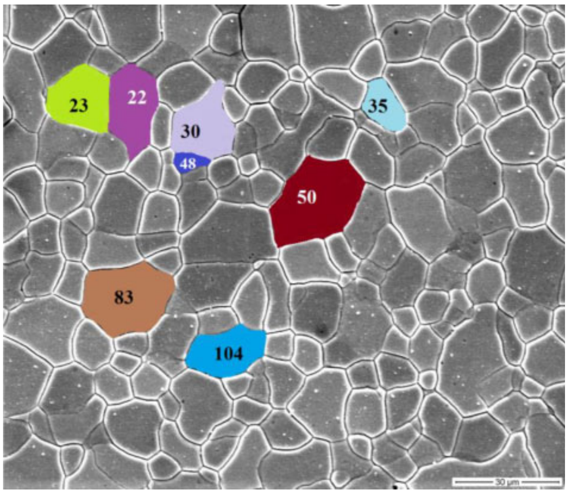

7 Marked grains in reference image

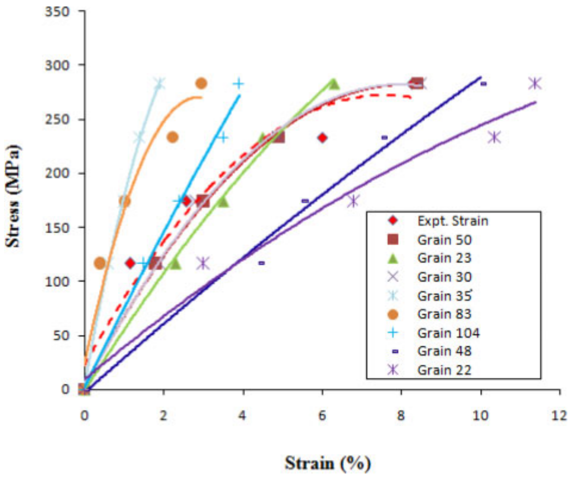

8 Stress–strain behaviour of different grains obtained using DIC method; macroscopic behaviour is shown in dashed line

Discussion

It is known that plastic deformation of metals and alloys occurs through movement of dislocations on slip planes. This mechanism of plastic deformation is known as slip. Although each grain of a polycrystalline material is in itself a single crystal, the orientation difference of the grains with respect to the loading axis does not permit all the grains to deform to the same extent. In the present study, it is observed that the slip lines (identified by red circle in Fig. 2*c*) become visible only when stress exceeds 174 MPa. The corresponding global strain at this load level is 2.56 pct. The slip lines are oriented at 45° to the loading axis, which coincides with the horizontal direction of the micrographs. It should be noted that using standard tensile specimen, the experimentally determined tensile yield strength of the steel is found as 189 MPa. The difference of 15MPa between the measured yield strength and the stress corresponding to the first visible slip lines in some grains arises from the differences in tensile deformation behaviour between macroscale and microscale (grain scale). With further increase of load, the slip lines become prominent and found in many grains as expected. All these observations point to the fact that all the grains do not deform to the same extent and at the same instant. The reason behind such grain to grain variation in strain arises because of the orientation difference of the grains with respect to the loading axis.[35]

To verify the above conclusion, a methodology has been developed based on the DIC technique to estimate the local strain. It is found that all the grains do not deform to the same extent, but the extent of average deformation of any grain increases with the increase of load. Similar heterogeneous deformation in tensile deformed 1 mm thick commercial interstitial free steel has also been reported by Ghadbeigi *et al.*[36] In order to find the grain level strain, we have selected the grains quite arbitrarily and run our programme. It is observed that all the selected grains do not deform plastically within the experimental domain, and these grains are termed as hard grains; hard in the sense of their orientation with respect to the loading axis. In the present investigation, it is observed that one or two grains out of eight different grains studied follow the global deformation pattern. Ghadbeigi *et al.*[36] also reported a similar observation in interstitial free steel, even for very large global deformation.

The methodology that has been developed and followed for measuring grain level strain also brings out that even within a grain there is substantial point to point variation of deformation. This variation also exists in those grains that closely follow the global specimen deformation. The point to point variation of strain within a grain leads to infer that the very local activation of slip systems even within a grain is different. However, detail characterisation of the activation of slip systems in individual grains using electron back scatter diffraction technique is necessary to support this inference. Qualitatively, it is also found that the density of slip lines is less in those grains that are comparatively smaller in size. This observation is well connected with the well known Hall–Petch relationship. According to the Hall–Petch relationship, plastic deformation becomes difficult with lowering of grain size. It means that with lowering of grain size, the onset of plastic deformation occurs at higher load. It should be noted that the present methodology to find the grain level strain fails at large global deformation. This happens because of the undulation of the specimen surface due to out of the plane movement of the grains.

The DIC methodology developed and used in the present study for measuring local strain is, however, not free from error. The sources for error are (i) the difficulties associated with correlating the subgrid corners in deformed images and (ii) drifting of electron beam in SEM. The difficulty of correlating the subgrid corners also arises with change of contrast and brightness of the images of deformed specimens. To minimise the corresponding error, normalisation of intensity values in all images has been done at the very beginning. Besides, to correlate the subgrid corners instead of point matching, a block based matching has been adopted. The best match for the block of size 3 × 3 centred at the subgrid corners (say, coordinate x,y) has been searched in a bigger search window of size 11 × 11 centred at (x,y) in the next image. The concept of block has been used so

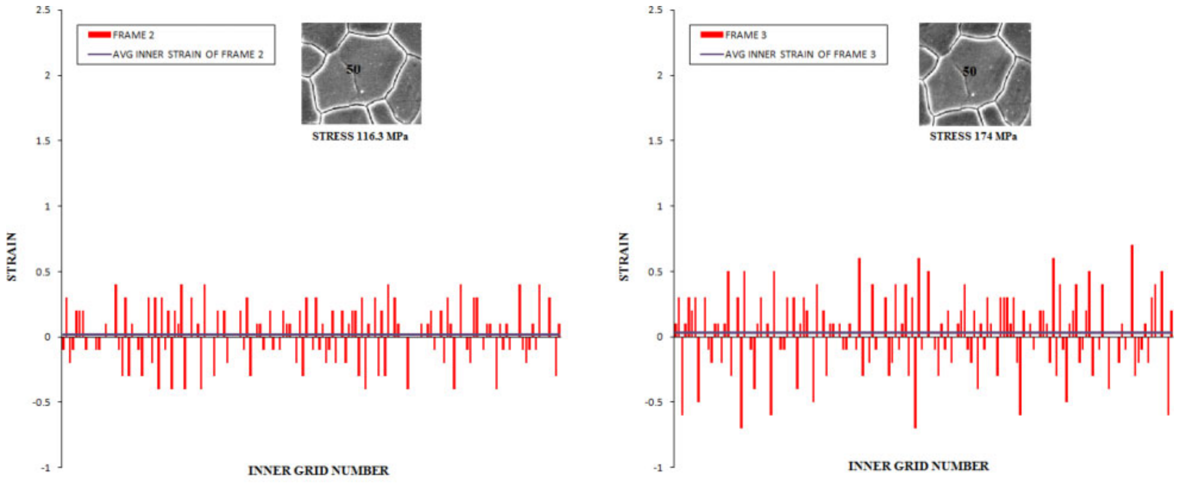

(a) Micrograph 2 (b) Micrograph 3

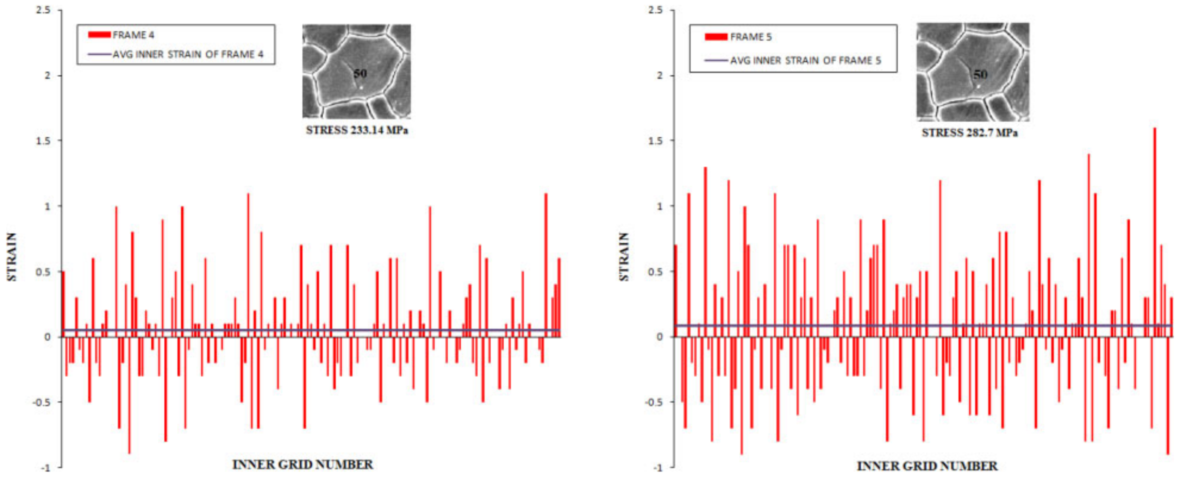

(c) Micrograph 4 (d) Micrograph 5

9 Strain distribution of individual subgrid over grain 50

that it captures the neighbourhood of the particular point. Such procedure minimises the possibility of mistracking of the subgrid corners. Tracking of the grains over the series of micrographs and matching the blocks in a bigger search window minimise the error introduced by drifting of electron beam.

In our study, we have estimated the error over a number of reference images, that is, of undeformed specimen, captured at different time intervals, which is about 5 minutes. Hence, the effect due to drifting of electron beam remains in the captured images. Additionally, to find the effect of brightness/contrast on the correlation process, the images of specimens were captured at different brightness/contrast levels. Based on the proposed image correlation technique, it has been found that the error associated with the tracked grains lies within the range of 0.1 to 0.6%. The error range takes account of all sources of error.

Implementation of our methodology on images of tensile deformed IFHS steel shows that for a global strain of 8.26 pct, the average strains of the marked grains (Fig. 7) are different. As an example, while for grain no. 35, the average strain is 1.9 pct, and it is 11.37 pct for grain no. 22. As already mentioned, such a large variation in the average strain at the grain level arises due to orientation difference of the grains with respect to the loading axis. In our study, we also found grain to grain variation in the maximum local strain value in the loading direction. In conformity with the observation of Ghadbeigi *et al.*,[36] in our study, it is also found that local maximum tensile strain varies across the grains. For example, while the local maximum tensile strain is 180 pct in grain no. 83, it is 70 pct in grain no. 48.

Conclusions

From the results and discussion presented above, it is concluded that tensile deformation of the investigated IFHS steel occurs heterogeneously. The heterogeneity of deformation not only exists among different grains but also within a grain itself. The DIC methodology developed to segment and track the grains considerably reduced the error in measuring the grain level average strain and also the local strain within a grain varying between 0.1 and 0.6 pct. This error value also takes into account the error due to contrast/brightness of the images. The present methodology is capable to segment and track all the grains without any intervention of the user. Finally, the technique developed measures the average strain and local strain of each grain. However, it is necessary to incorporate electron back scattering diffraction characterisation of the specimen in the undeformed and deformed conditions at the individual grain level so to correlate the slip system activation of the individual grain with the measured strain. The beauty of the present methodology is that it uses artificial grids over the images and does not require any other sophisticated experimental technique to lay the grids on the specimen surface itself. The present methodology reveals that deformation is heterogeneous, and for an applied global strain of 8.26 pct locally within the grain interior, strain is magnified by many times reaching as high as 150 percent. Further, this local magnification of strain increases with the increase of global strain.

Acknowledgement

The authors deeply acknowledge the Ministry of Steel (GOI) and TATA Steel Ltd., Jamshedpur, India, for providing research grant (file no. 11(7)/SDF/2007-TW) to create the experimental facility and carry out the investigation.

References

1. K. Hashimoto and H. Margolin: 'The role of elastic interaction stresses on the onset of slip in polycrystalline alpha brass-I Experimental determination of operating slip systems and qualitative analysis', *Acta Metall.*, 1983, **31**, 773–785.
2. A. Musienko, A. Tatschl, K. Schmidegg, O. Kolednik, R. Pippan and G. Cailletaud: 'Three-dimensional finite element simulation of a polycrystalline copper specimen', *Acta Mater.*, 2007, **55**, 4121–4136.
3. M. Kamaya, Y. Kawamura and T. Kitamura: 'Three-dimensional local stress analysis on grain boundaries in polycrystalline material', *Int. J. Solids Struct.*, 2007, **44**, 3267–3277.
4. D. Raabe, M. Sachtleber, Z. Zhao, F. Roters and S. Zaefferer: 'Micromechanical and macromechanical effects in grain scale polycrystal plasticity experimentation and simulation', *Acta Mater.*, 2001, **49**, 3433–3441.
5. P. V. Makarov, S. Schmauder, O. I. Cherepanov, I. Yu, V. A. Smolin, R. R. Ramanova, D. Balokhonov, Yu. Saraev, E. Soppa, P. Kizler, G. Fischer, S. Hu and M. Ludwig: 'Simulation of elastic-plastic deformation and fracture of materials at micro-, meso- and macro levels', *Theor. Appl. Fract. Mech.*, 2001, **37**, 183–244.
6. A. Rusinko: 'Non-classical problems of irreversible deformation in terms of the synthetic theory, Acta Polytech', *Hung*, 2010, **7**, (3), 25–62.
7. E. M. Gunel and C. Basaran: 'Micro-deformation mechanisms in thermoformed alumina trihydrate reinforced poly (methyl methacrylate)', *Mater. Sci. Eng. A*, 2009, **A523**, 160–172.
8. K. J. Kurzydlowski: 'Microstructural refinement and properties of metals processed by severe plastic deformation', *Bull. Pol. Acad. Tech. Sci.*, 2004, **52**, (4).
9. I. Okipnyi, P. Maruschak, A. Sorochak and F. Sergejev: 'Measurement of deformation hardening of heat-resistant steel of the WWER-type reactor', Proc. 8th Int. DAAAM Baltic Conf. on 'Industrial engineering, Tallinn, Estonia, April 2012, DAAAM Baltic, Tallinn University of Technology, 694–699.
10. J. Piwnik and K. Mogielnicki: 'Deformations in micro extrusion of metals', *Arch. Foundry Eng.*, 2010, **10**, (3), 87–90.
11. P. K. Pradhan, P. R. Dash, P. S. Robi and S. K. Roy: 'Micro void coalescence of ductile fracture in mild steel during tensile straining', *Frattura ed Integrità Strutturale*, 2012, **19**, 51–60.
12. K. Qian, H. Xie and A. Asundil: 'Two dimensional digital image correlation for inplane displacement and strain measurement: a review', *Meas. Sci. Technol.*, 2009, **20**, (6).
13. M. S. Ulstad: 'An algorithm for estimating small scale differences between two digital images', *Pattern Recognit.*, 1973, **5**, (4), 323–333.
14. M. Sjodahl: 'Electronic speckle photography: Increased accuracy by non integral pixel shifting', *Appl. Opt.*, 1994, **33**, (28), 6667–6673.
15. R. Cintron and V. Saouma: 'Strain measurements with the digital image correlation system Vic 2d', 'Technical report, University of Colorado, Boulder, CO, USA'; 2008.
16. D. Rugg: 'Materials for future gas turbine applications', *Mater. Sci. Technol.*, 2014, **30**, (15), 1848–1852.
17. J. R. Davenport, L. Mendez-Garcia, S. Purkayastha, M. E. Hancock, R. J. Stearn and W. J. Clegg: 'Material needs for turbine sealing at high temperature', *Mater. Sci. Technol.*, 2014, **30**, (15), 1877–1883.
18. J. Kang: 'Microscopic strain mapping based on digital image correlation', Int. Cong. Expo. on Experimental and Applied Mechanics, Society for Experimental Mechanics, Orlando, FL, USA; 2008.
19. M. Gom: 'Aramis-deformation measurement using the grating method', User's Manual, V5.3.0-8, Braunschweig, Germany; 2003.
20. X. Cao, Z. Bi, X. Wei and Y. Xie: 'Determination of poissons ratio of kraft paper using digital image correlation', *Mech. Eng. Technol. Adv. Intell. Soft Comput.*, 2012, **125**, 51–57.
21. M. Kass, A. Witkin and D. Terzopoulous: 'Snakes: active contour models', *Int. J. Comput. Vision*, 1988, **1**, (4), 321–331.
22. T. McInerney and D. Terzopoulous: 'T-snake: Topology adaptive snakes', *Med. Image Anal.*, 2000, **4**, (2), 73–91.
23. S. Beucher and C. Lantuéj: 'Use of watershed in contour detection', Int. Workshop on 'Image processing, real-time edge and motion detection', Rennes, France, 1979. Available at: http://cmm.ensmp.fr/~beucher/publi/watershed.pdf
24. F. Meyer and S. Beucher: 'Morphological segmentation', *J. Visual Commun. Image Represent.*, 1990, **1**, (1), 21–46.
25. S. Beucher: 'The watershed transformation applied to image segmentation', *Scanning Microsc.*, 1992, 299–314.
26. M. Couprie and G. Bertrand: 'Topological grayscale watershed transform', *SPIE Vision Geom. Proc.*, 1997, **3168**, 136–146.
27. M. Couprie, L. Najman and G. Bertrand: 'Algorithms for the topological watershed', Proc. Int. Conf. on 'Discrete geometry for computer imagery, Poitiers, France, April 2005; Springer 172–182.
28. G. Bertrand: 'On topological watersheds', *J. Math. Imaging Vision*, 2005, **22**, (2-3), 217–230.
29. B. Chanda and D. D. Majumder: 'Digital image processing and analysis'; 2009, New York, Prentice Hall India.
30. R. C. Gonzalez and R. E. Woods: 'Digital image processing'; 1992, Upper Saddle, NJ, Prentice Hall.
31. K. Stoshi, H. Kazuhiro, M. Yanada, I. Minami, Y. Kimura and S. Ikeda: 'Direct drawing method for microfabrication based on selective metal plating technology', *Sens. Actuators A, 103A*, 2003, **135**, 142.
32. S. C. Jacobsen, D. L. Wells, C. C. Davis and J. E. Wood: 'Fabrication of micro-structures using non-planar lithography (NPL)', Proc. MEMS'91, Nara, Japan, January 1991, IEEE, 74–79.
33. C. Beuret, G. A. Racine, J. Gobet, R. Luthier and N. F. Rooij: 'Microfabrication of multidirectional inclined structure by uv lithography and electroplating', Proc. MEMS'94, Oiso, Japan, January 1994, IEEE, 81–85.
34. S. Konishi, K. Honsho and S. Sugiyama: 'Direct drawing for micro-fabrication without photolithography', Proc. MEMS'99, Florida, January 1999, IEEE, 194–199.
35. M. A. Tschopp, B. B. Bartha, W. J. Porter, P. T. Murry and S. B. Fairchild: 'Microstructure dependent local strain behaviour in polycrystals through in-situ scanning electron microscope tensile experiments', *Metall. Mater. Trans. A*, 2009, **40A**, (10), 2363–2368.
36. H. Ghadbeigi, C. Pinna and S. Celotto: 'Quantitative strain analysis of the large deformation at the scale of microstructure: comparison between digital image correlation and microgrid techniques', *Exp. Mech.*, 2012, **52**, (9), 1483–1492.

Measurement 46 (2013) 2435–2440

Contents lists available at SciVerse ScienceDirect

Measurement

journal homepage: www.elsevier.com/locate/measurement

Segmentation of dual phase steel micrograph: An automated approach

Siddhartha Banerjee [a], Swarup Kumar Ghosh [b], Shubhabrata Datta [c], Sanjoy Kumar Saha [d,*]

[a] *Dept. of Computer Science, RK Mission Residential College, Narendrapur, 24 Parganas (South), West Bengal, India*
[b] *Dept. of Metallurgy & Material Engg., Bengal Engg. & Science University, Shibpur, Howrah, India*
[c] *Dev Bhoomi Institute of Technology & Engineering, Dehradun, India*
[d] *Dept. of Computer Science & Engg., Jadavpur University, Kolkata, India*

ARTICLE INFO

Article history:
Received 9 November 2012
Received in revised form 28 January 2013
Accepted 25 April 2013
Available online 15 May 2013

Keywords:
Phase extraction
Micrograph segmentation
Microstructure analysis
Phase quantification
Scanning electron micrograph

ABSTRACT

Digital image processing is used to analyze the microscopic images of the materials. Extraction of grains/phases present in the material is the fundamental step to achieve the description of the microstructure. In this work, we present an automated scheme for segmenting the phases present in the scanning electron microscopic images of dual phase steel. The challenges posed by the presence of revealed grain boundaries bearing striking similarity with one of the phases and intensity variation within the phase regions also has been addressed successfully. The proposed scheme successfully approximates the closed phase regions for a variety of micrographs. Moreover, the proposed scheme does not make any assumption regarding the factors like magnification and any other imaging condition affecting the image characteristics.

1. Introduction

Proper identification of phases and their quantitative description is an important aspect in the field of materials characterization. Direct technique includes steps like microscopic observation and image collection, image processing and analysis [1]. Many variations of microscopes like optical microscope, scanning electron microscope (SEM) and transmission electron microscope (TEM), are used with great success allowing us to peer into spaces small enough to be seen with the unaided eye. Thus these instruments have become an indispensable tool in materials research.

The images/micrographs produced by a microscope are easily converted into digital form for subsequent storage, analysis, or processing prior to display and/or interpretation [2–6]. Digital Image processing greatly enhances the process of extracting information about the specimen from a micrograph and has become an integral part of microscopy related experimentation in metallurgy and materials engineering [7,8]. Major steps in image analysis based measurement techniques are image acquisition, extraction/segmentation of area of interest and measurement of properties. Once the images are converted into digital form, phase/grain segmentation and identification appear as the major challenge. Grains/phases to be extracted are normally discriminated using the gray level intensity. Most of the software available for this purpose uses this technique and generates more or less acceptable results in case of optical micrographs. But for images generated from scanning electron microscope having higher resolution the procedure of gray level intensity for discrimination of phases is a complete failure, though increasing use of SEM images and requirement of image analysis and quantification of SEM images with low to moderate magnification is becoming a necessity. SEM images with higher resolution could easily resolve the phases like pearlite, bainite or martensite into black and white portions. If these images are analyzed and quantified using conventional

---

* Corresponding author. Tel.: +91 3324296470.
E-mail address: sks_ju@yahoo.co.in (S.K. Saha).

0263-2241/$ - see front matter © 2013 Elsevier Ltd. All rights reserved.
http://dx.doi.org/10.1016/j.measurement.2013.04.057

software black or white portion of those phases are added to other phases present in that micrograph. Discrimination problem may also occur with phases with almost similar gray level, such as the case of different ferrites viz. granular and acicular ferrite. In such cases textural pattern, edge orientation and morphological pattern have to be considered in addition to the gray level intensity for proper identification of phases. In addition to this presence of revealed grain boundary with features similar to those of another grain offers challenge.

Gauthier et al. [9] has presented an automated scheme for segmenting WC grains in the Cobalt matrix. They have adopted a two stage algorithm. Based on gray level threshold and morphological gradient filter, first level segmentation has been done and in the next stage, they have gone through a series of involved processing to get rid of grain boundaries. Classification based approach was tried in [10]. In [11], a scheme has been presented where an image classifier has been integrated with context vision [12]. Neural network also have been tried to classify the phases of an alloy [13].

In the area of materials engineering, quantitative metallography deals with the features of the microstructure in a two dimensional plane, which can be correlated with the other properties of the material, as discussed earlier. The analysis of metallurgical samples includes grain size analysis, inclusion rating, volume fraction, porosity, particle size, morphology etc. Thus the results obtained from such analysis have immense importance not only for material characterization, but also for industrial production for effective quality control [14–16]. The stereological analysis method is successfully applied for quantification of chunky graphite [17] and volume fraction phases in titanium alloys [18]. It has already been emphasized that the most important aspect of automatic image analysis is to properly classify different phases in dual phase or multiphase metallography samples. The accuracy of subsequent measures relies on the performance of the underlying segmentation scheme. Considering all these issues, it is evident that a robust and elegant segmentation scheme is still in demand. It has motivated us to focus on segmentation.

In the present work effort is made to quantify SEM micrographs of dual phase steel. Here due to higher resolution of the microscope, the pixel values of several regions within the second phase (martensite) matches with that of the primary phase (ferrite). This type of confusion areas exist in cases of SEM images of ferrite–pearlite or ferrite–bainite steels also, but generally absent in case of images grabbed through optical microscope due to lesser resolution. The paper is organized as follows. The brief introduction presented in this section is followed by the detailed description proposed methodology in Section 2. Experimental results are presented in Section 3 and it is finally concluded in Section 4.

2. Methodology

In this work, we have dealt with SEM images of dual phase steels consisting of two distinct phases, soft polygonal ferrite matrix along with the distribution of hard martensite second phase in the form of island. Images of the samples, polished and etched with 2% Nital, were carried out by in Scanning Electron Microscope (Model: Hitachi S3400N), in secondary electron mode, at various magnifications. The ferrite grains with black appearance cover the major part whereas the sparsely distributed second phase appears as white blobs (see Fig. 1). Thus, the task can be mapped onto the classical problem of segmenting the background and foreground. But, numbers of challenges come up which are as follows.

- The grain boundary also possesses the similar intensity (white in our case) as one of the phases (martensite).
- Martensite components may not possess uniform intensity. Even it may have ferrite like intensity values trapped inside.
- A single martensite component may appear as a collection of splitted sub-components.

The challenges make the task quite difficult. It is no longer a simple task of intensity based extraction of regions of two types. The boundaries are to be identified and excluded. A closed contour of the white phases encompassing the nearby sub-components has to be formed. Otherwise the white grain boundaries and the black segment within the martensite laths will disturb the phase identification and phase quantification process. The broad steps to accomplish the tasks are as follows.

- Initial segmentation.
- Phase formation.
- Phase refinement.

The steps are detailed in the following sub-sections.

2.1. Initial segmentation

It has been observed that intensity values of the pixels in two phases can be broadly categorized as black and white. Thus, the primary target is to binarize the given image. As the boundary pixels are also white, the removal of the same is taken up with the binarized image. The steps for initial segmentation are as follows.

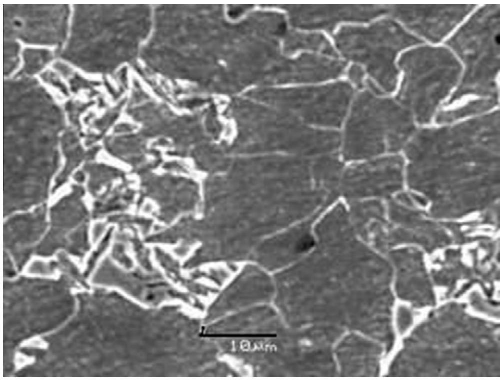

Fig. 1. A SEM image of dual-phase steel.

- Smoothing.
- Thresholding.
- Boundary removal.

The micrograph may not reflect strong contrast between the two phases. The ferrite grains are not uniformly black. It contains variation. Same is also true for the martensite phase. Due to the limitation imposed by image acquisition environment and surface undulation, such variations and/or noise may creep in. To minimise such effects we perform pre-processing prior to thresholding. 5 × 5 mean filter is applied to smoothen the image.

Thresholding is applied on the smoothened version of the original image. Based on the intensity histogram, a threshold, *th* is chosen. Pixels with intensity higher than *th* are considered as white and black otherwise. Selection of *th* is important, as the phases show considerable variation and contrast is also not very high always. We have relied on thresholding scheme proposed by Otsu [19]. As the histogram for the micrographs are bimodal in nature, Otsu algorithm is well suited. The optimal threshold is chosen in a way to minimize the intra-class variance. The thresholded image corresponding to the image in Fig. 1 has been shown in Fig. 2.

It may be noted that in the thresholded image the pixels forming the inter ferrite grain boundaries also take part in the process of binarization and appear as white. But, the grain boundaries are thinner with respect to the actual martensite phase regions. Based on these observations, we have applied morphological opening operation [20] to get rid of thin boundary segments. Opening operation consists of morphological erosion followed by dilation. Let size of the structuring element (SE) for morphological operation be S × S. In order to erode the binary image, the centre of SE is placed on a pixel and in the eroded image; the corresponding pixel is converted to a black one if any of the pixels covered by SE in the binary image is black, otherwise white. Thus the grain boundaries being thinner get removed. White regions retained after erosion also get shrinked and in order to retain their original size, dilation is carried out with the eroded image. Centre of the SE is placed on a pixel of eroded image. The corresponding pixel in the dilated image is white if any of the pixels covered by SE in the eroded image is white, otherwise black. In our experiment, 5 × 5 structuring element has been considered for opening operation. Thus, the output after boundary removal operation on image in Fig. 2 has been shown in Fig. 3.

2.2. Phase formation

After initial segmentation, we take up the task of formation of the white phases. Martensite phase may not have uniform high intensity all over the region that it covers. As a result black regions may be trapped in inter-lath positions and also may be splitted into multiple white components as evident in Fig. 3. Thus, the white components with in the neighbourhood are to be linked and closed contour encompassing the linked components has to be formed to develop a continuous martensite region.

Disjoint white components are first identified and labeled through component labeling [20]. A component C_i is linked with another component C_j if either of the following conditions is satisfied.

- C_i and C_j lie within a neighbourhood.
- Bounding box of C_i includes major part of C_j.

In order to link the components, the procedure evolves as follows.

- Consider an array P and initialize each element $P(r,c)$ as black.
- For each component C_i.
  - Dilate [20] the component by a structuring element of size K × K to obtain C_{id}.
  - Mark $P(r,c)$ as white for $(r,c) \in C_{id}$ if C_{id} touches/enters C_j and $(i \neq j)$, otherwise for $(r,c) \in C_i$.
- Perform component labeling on P.
- Consider an array F and initialize each element $F(r,c)$ as black.
- For each component C_i in P.
  - Consider an array *temp* and initialize each element *temp(r,c)* as black.
  - Find the bounding box bb_i of C_i.
  - S be the set of components C_j whose p% area or more lies within bb_i.
  - Compute the bounding box BB_i encompassing all components $C_j \in S$.
  - $temp\,(r,c) = P\,(r,c)$ if $(r,c) \in BB_i$.

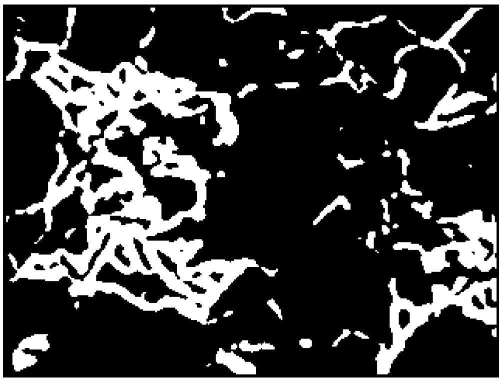

Fig. 2. Image after thresholding.

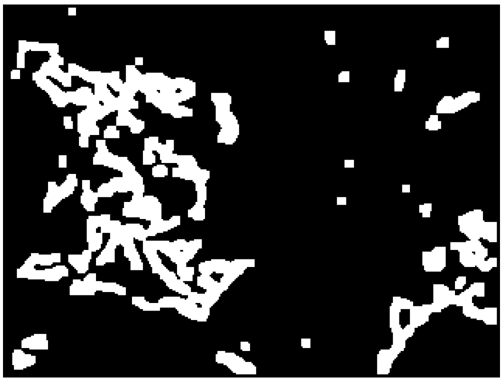

Fig. 3. Image after boundary removal.

- Execute procedure *closed_contour (temp)* and store output in the array *CC*.

Mark *F (r, c)* as white for all *(r, c)* such that *CC (r, c)* is white

- *F* is taken as the output.

As it has been indicated in the algorithm, it deals with two major steps. At first level, a component is dilated to identify and link the neighboring components. In our experiment, size of structuring element has been empirically chosen as 5×5. It should neither be too low nor be too high. Along with linking, dilation also helps to smoothen the contour of the component itself that may arise out of non-uniform intensity variation around the contour leading towards omission in thresholding process. Effect of dilation is ignored if it fails to link a component with others. As a result unnecessary growth of the components is also avoided. After such linking, components are relabeled. The second stage of algorithm proceeds with the newly labeled components. At this stage, the neighborhood is defined differently in terms of the bounding box. Presence of low intensity within the white phase may split it in a manner which fails to satisfy the first criteria. Bounding box based definition of neighbourhood addresses these cases. For each component, the minimal bounding box is determined and other components whose major area (in our, experiment it has been taken as at least 50%) falls within the same bounding box are considered as the components to be linked. *closed_contour()* procedure is carried out on the bounding box encompassing all the components to be linked. The technique has been elaborated in [21,22]. It approximates the contour as the pseudo convex hull of the object. The procedure finally generates a closed contour by combining the components and it also removes the shaded region trapped inside.

Let B be the image where $B\,(r, c) = BB_i\,(r, c)$ if $(r, c) \in BB_i$ else $B\,(r, c) = 0$. The steps for the procedure *closed_contour*(B) are as follows.

1. Take four other arrays $H\,(i,j)$, $V\,(i,j)$, $D1\,(i,j)$ and $D2\,(i,j)$ of same size as that of $B\,(i,j)$, and initialize them with one.
2. For each row of $H\,(i,j)$.
   (a) Start from first column, change its pixel value to zero and move right until $B(i,j) = 1$ or the last column is reached.
   (b) If the last column is not reached then start from last column, change pixel values to zero and move left ward until $B(i,j) = 1$.
3. Now repeat sub-steps of 2 for $V\,(i,j)$, $D1\,(i,j)$ and $D2\,(i,j)$ with appropriate directions i.e., upward and downward for V and along the two principal diagonals for $D1$ and $D2$.
4. Finally, produce a binary image $F\,(i,j)$ that contains the pseudo convex hull of the given image B as follows:

$$F(i,j) = \begin{cases} 1 & H(i,j) + V(i,j) + D1(i,j) + D2(i,j) \geq th \\ 0 & \text{otherwise} \end{cases} \tag{1}$$

The binary image of which closed region is required is scanned in four directions. Scanning starts from image boundary and goes on marking the pixels as background till it encounters the foreground pixel i.e. object boundary. In case there is a discontinuity in the object contour, scan lines may intrude inside the object. Such intrusion varies for different scan directions. Depending on the degree of discontinuity and value of *th*, such open regions are approximated to form a closed region. Physically, *th* denotes at least from how many directions a boundary pixels of the foreground object can be reached. In our experiment, *th* is taken as 2. Thus, a continuous white phase with smooth contour is approximated. The pixels *F (i,j)* with value 1 constitute the phase. Output corresponding to the image in Fig. 3 has been shown in Fig. 4. Now we get the image free from grain boundaries between the ferrite grains and also with distinct martensite regions.

2.3. Phase refinement

Once the white phases are formed, we carry out post-processing activities.

It consists of two steps as follows.

- Phase linking.
- Small component removal.

During phase formation stage, components within proximity have been merged together. At this stage, possible merging of phase regions is taken up. In order to define the neighbourhood for finding the regions likely to be merged, we rely only on the first condition described in Section 2.2. Bounding box based criteria can lead to undesirable phase linking. As phase has been already formed by extending the components, a strict approach is followed at this stage. A white phase region is dilated by a $K \times K$ structuring element.

In our experiment K is taken as 5. If because of dilation at a point, the region gets connected with another then effect is retained otherwise previous state is maintained by canceling the growth. In case regions are merged, there is a possibility that black phase may be trapped inside. To remove those, region filling algorithm is applied.

Because of noise, thresholding and other practical limitations small white regions may be formed. Such regions are removed based on the size analysis of the detected regions. Regions with size smaller than a threshold, t_s are removed. *ts* is taken as *max*($\mu s - \sigma s$, 0.1 µs). μs and σs are

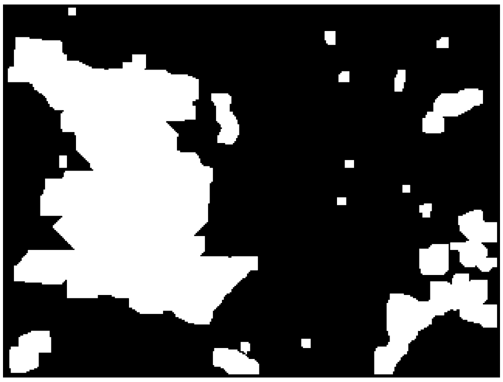

Fig. 4. Image after phase formation.

Fig. 5. Image after phase refinement.

the average and standard deviation of the region sizes. After post-processing, the final output corresponding to the image in Fig. 4 has been shown in Fig. 5.

3. Results and discussion

In order to carry out the experiment, we have considered 12 dual phase steel micrographs. They vary in terms grain size and concentration, magnification and illumination level. Such collection has enabled us to judge the robustness of proposed scheme. Representative outputs are shown in Fig. 6.

To measure the segmentation performance, we have compared the result with ground-truth information. As white martensitic regions are interfered by the boundaries, analysis is also focused on it. It has been observed that the proposed scheme successfully discards the grain boundaries. Table 1 shows the fraction of white (martensite) and black (ferrite) phases as obtained at the various stages of processing for the samples shown in Fig. 6b–e. As expected the phase fraction of the white phase decreases significantly after the grain boundary removal (Fig. 6c). But still the volume fraction of the black phase includes inter lath dark regions of the martensite, may be due to the formation of low angle grain boundaries. Due to the joining of white region and formation of phase contour of the martensite phase, the volume fraction of the phase increases in subsequent steps (Figs. 6d and 6e). The changes in the volume fraction of each phase in every step, shown in Table 1, indicate the importance of all operations on the image. Fig. 6f shows the results after analyses using standard software used for analyses and quantification of micrographs (Olysia). The images seem to be almost similar to the images formed after the thresholding step using the present scheme. This actually justifies the steps used after the thresholding to actually recognize and compute two separate phases distinctly. The volume fractions of martensite

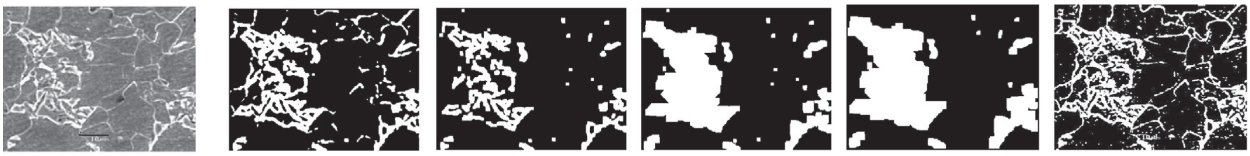

(i) Image 1

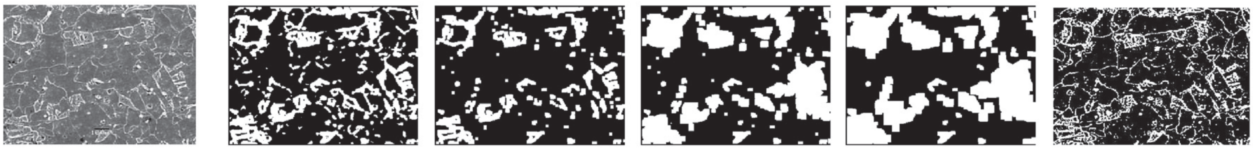

(ii) Image 2

(iii) Image 3

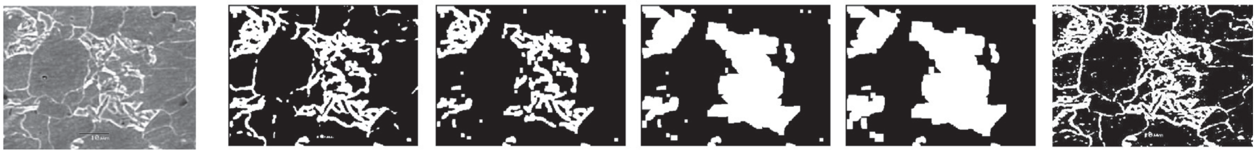

(iv) Image 4

Fig. 6. Few sample results : (a) original grayscale image, (b) image after thresholding, (c) image after boundary removal (d) image after phase formation (e) image after phase refinement, (f) image after analysis using Olysia software.

Table 1
Volume fraction of the two phases at different stages of processing.

Image	After Thresholding		After Boundary Removal		After Phase Formation		After Phase Refinement		From Olysia software	
	White	Black	White	Black	White	Black	White	Black	White	Black
Image 1	.22	.78	.17	.83	.28	.72	.32	.68	.26	.74
Image 2	.29	.71	.21	.79	.34	.66	.40	.60	.22	.78
Image 3	.19	.81	.17	.83	.33	.67	.37	.63	.21	.79
Image 4	.23	.77	.19	.81	.31	.69	.34	.66	.29	.71

as calculated by the Olysia software are also depicted in the Table. This also clearly shows the amount of error present in the result using only thresholding operation. It is evident in Fig. 6 that the proposed methodology can well approximate the phase regions even in presence of intensity variation within a phase which a simple threshold based scheme cannot. The implication of the methodology towards the volume fraction of the phases is also well reflected in Table 1. The results also show that present method is superior to the methods applied by the conventional software, and can serve as a practical approach for analysis and quantification of SEM images. The method, as evident from the above results, is not specific for dual phase steel only. It may be applied to many other steel or even other materials, where the microstructure contains such areas of confusion, as in this case where pixels values of several regions within the second phase matches with that of the primary phase (ferrite) due to higher resolution of the microscope though which the images are grabbed. But the idea has to be practically verified in future.

4. Conclusion

- A novel scheme for automatic extraction of the phases present in the microscopic image of dual phase steel is presented. The proposed scheme has overcome the problems of simple threshold based scheme.
- In spite of strong similarity between the grain boundary and a phase, the scheme successfully discriminates them. Even in presence of intensity variation within the martensite phase, the proposed scheme can well approximate closed phase region.
- Moreover, the strength of the scheme lies in the fact that it does not rely on any assumption about the issues like magnification factor, contrast level which affects the image characteristics.
- Experimental result indicates that performance of the scheme is satisfactory for a wide variety of cases.

References

[1] K.J. Kurzydlowski, B. Ralph, The Quantitative Description of the Microstructure of Materials, CRC Press, London, 1995.
[2] Q. Wu, F.S. Merchant, K.R. Catleman, Microscope Image Processing, Academic Press, UK, 2008.
[3] D.L. Spector, R.D. Goldman, in: Basic Methods in Microscopy, Cold Spring Harbor Laboratory Press, 2005.
[4] G. Sluder, D.E. Wolf, Digital Microscopy, Academic Press, UK, 2003.
[5] S. Inoue, K.R. Spring, in: Video Microscopy, Springer, 1997.
[6] D.B. Murphy, in: Fundamentals of Light Microscopy and Electronic Imaging, Wiley-Liss, 2001.
[7] K.R. Castleman, in: Digital Image Processing, Prentice-Hall, 1996.
[8] A. Diaspro, in: Confocal and Two-photon Microscopy, Wiley-Liss, 2001.
[9] G. Gauthier, M. Coster, L. Chermant, J. Chermant, Morphological segmentation of cutting tools, Microsc. Microanal. Microstruct. 7 (1996) 339–344.
[10] H.V. Saebo, K. Braten, N.L. Hjort, B. Llewellyn, E. Mohn, Contextual classification of remotely sensed data: statistical methods and development of a system, Technical Report, Norwegian Computing Center.
[11] J. Komenda, Automatic recognition of complex microstructures using the image classifier, Mater. Charact. 46 (2001) 87–92.
[12] Contextvision, Users's Guide, MicroGOP2000/S Software v. 3.1, 1999.
[13] V.H.C. deAlbuquerque, A.R. Alexandria, P.C. Cortez, J.M.R.S. Tavares, Evaluation of multilayer perceptron and self-organizing map neural network topologies applied on microstructure segmentation from metallographic images, NDT and E International 42 (2009) 644–651.
[14] G. Das, Image analysis in quantitative metallography, in: Proc. Workshop on Materials Charaterization Techniques – Principles and Appli-cation, NML, Jamshedpur, India, 1999, pp. 135–150.
[15] M. Goken, H. Vehoff, Quantitative metallography of structural mater with the atomic force microscope, Scripta Mater. 35 (1996) 983–989.
[16] Materials Handbook, Metallography and Microscopy, vol. 9, AST Publication, Ohio, 1988.
[17] K. Breitkreutz, H. Frenz, P.D. Portella, On the quantitative determination of chunky graphite in cast iron, Pract. Metallogr. 28 (1991) 532–541.
[18] K. Wang, W. Zeng, Y. Shao, Z. Zhao, Y. Zhou, Quantification of microstructural features in titanium alloys based on stereology, Rare Metal Mater. Eng. 38 (2009) 398–403.
[19] N. Otsu, A threshold selection method from gray level histogram, IEEE trans. Sys. Man, Cyber. vol. 9(1), 1979, pp. 62–66.
[20] B. Chanda, D.D. Majumder, in: Digital Image Processing and Analysis, Prentice-Hall, 2001.
[21] S.K. Saha, A.K. Das, B. Chanda, Graytone image retrieval using shape feature based on petal projection, in: Proc. ICAPR, 2003, pp. 252–256.
[22] S.K. Saha, A.K. Das, B. Chanda, An automatic image segmentation technique based on pseudo-convex hull, in: Proc. ICVGIP, 2006, pp. 70–81.